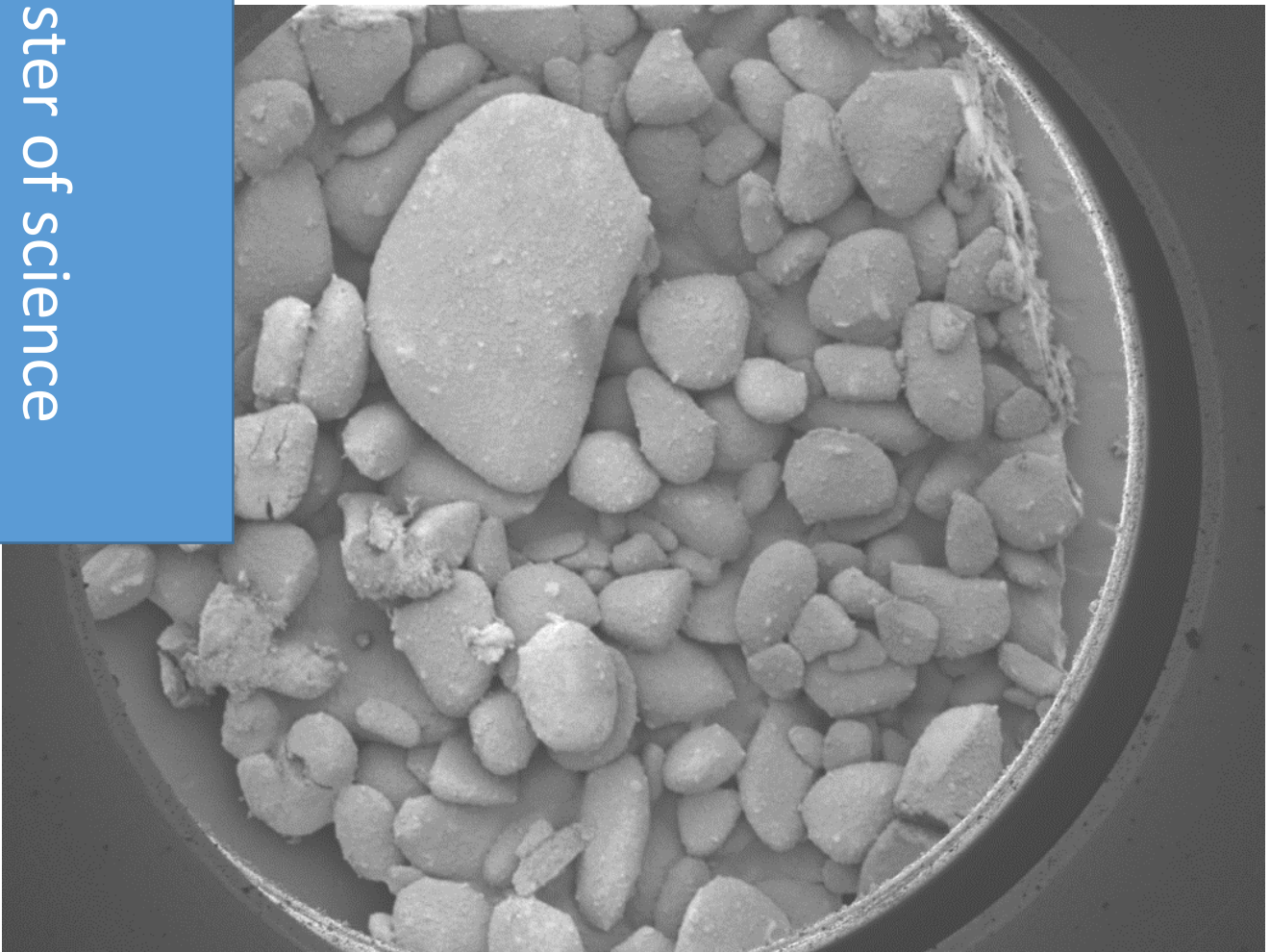


# Optimization of scale-up of KNLN piezocomposites

for flexible haptic feedback applications

*A. Sivagnana Sundaram*

Master of science



*(This page was intentionally left blank)*

# Optimization of scale-up of KNLN piezocomposites for flexible haptic feedback applications

By

A. Sivagnana Sundaram  
(4696158)

in partial fulfilment of the requirements for the degree of:

**Master of Science**  
**in Aerospace Structures and Materials**

at the Delft University of Technology,  
to be defended publicly on Thursday February 27, 2020 at 09:00 AM

Supervisor:	Dr. T. Mahon,	TU Delft
Thesis committee:	Prof. dr. W. A. Groen,	TU Delft
	Prof. dr. ir. S. van der Zwaag,	TU Delft
	Dr. S. Turteltaub,	TU Delft
	Dr. T. Hoeks,	SABIC IP

*This thesis is confidential and cannot be made public until February 27<sup>th</sup> 2020.*

An electronic version of this thesis is available at <http://repository.tudelft.nl/>.

*(This page was intentionally left blank)*

# Preface

This report is the result of a study into the optimization of scale-up of KNLN ceramic and the subsequent mechanical testing of KNLN piezocomposites used for flexible haptic feedback application. This report has been written based on the culmination of work done on the aforementioned topic from the 15<sup>th</sup> July, 2019 to 27<sup>th</sup> February, 2020 as part of my master of science thesis in the programme of Aerospace Structures and Materials with NoVAM profile. The work has been performed entirely at the Delft university of technology, Delft, Netherlands in collaboration with SABIC research and technology Pvt. Ltd, Bangalore, India.

*A. Sivagnana Sundaram*

*Delft, February 2020*

# Acknowledgements

The completion of this master's thesis would not have been possible without the continuous help and guidance from the people who have supported me in this road. For that, I would like to wish my utmost gratitude to them.

First and foremost, I owe my deepest gratitude to my supervisor Dr. Tadhg Mahon, for providing me an opportunity in doing a thesis on flexible piezoelectric composites. His continuous support, suggestions and encouragement was pivotal to the thesis and made me not only into a better scientific thinker but also a better person. His technical expertise and critical thinking has been a great help towards achieving my goals. It has definitely been a great pleasure working with him for the past 8 months.

I would like to thank Prof. Pim Groen, for his key role in the thesis and for providing me an opportunity to work under the SMART materials group of NoVAM. His critique and guidance during several meetings and during general working of the thesis aided me to structure the thesis well and helped me to improve my abilities in performing research.

I would like to thank Ir. Durga Mainali, Dr. Marlies Nijmeisland and Dr. Johan Bijleveld for their continuous help with introducing me to the theory and usage of new apparatus. I am very grateful to them for providing me subtle tips on how to better perform an experiment with their expertise in the subject which really helped me save time during the thesis. I am also thankful to them for educating me on the various precautions one must take before performing an experiment especially since I handled moderately hazardous substances.

I would like to thank Shanta Visser for helping me with setting up the meetings/presentations on time with my supervisors and also for her punctual reminders to the meetings.

I would like to thank all the members of NoVAM for their continuous help, input in the project and also for making this journey one of the most fruitful, enjoyable and unforgettable experiences of my life.

Finally, I would like to thank my parents and friends for always being a helping hand during stressful days and supporting my decisions throughout the thesis.

*A. Sivagnana Sundaram*

*Delft, February 2020*

# Abstract

In this thesis, we focus on flexible haptic feedback applications which rely on the sensation of touch to display a feedback to the user that establishes a system to user interaction. Piezoelectric materials can be used in these applications due to their ability to deform under an electric field. In these applications flexibility is mandatory and hence, rather than ceramics, flexible piezoelectric polymers are used. However, due to several disadvantages associated with piezoelectric polymers recent trend has shifted towards using piezocomposites made of piezoceramic and polymer phases. The most versatile and commonly used piezoceramic: lead zirconium titanate or PZTs, cannot be used in this case due to its high toxicity and high dielectric mismatch in a composite. Hence, a lead-free alternative: 3 % lithium doped potassium sodium niobate or KNLN-3 has been chosen as the ceramic phase. A non-piezoelectric polymer PVDF-TrFE-CFE with a high dielectric constant was chosen as the polymer phase to decrease the dielectric mismatch to the maximum extent.

The first objective of this thesis is to optimize the scale-up in production of KNLN-3 ceramic for this particular application when employed as a random 0-3 composite. Thus, the production process of the KNLN-3 ceramic was analyzed with respect to the microstructure, purity, surface topology, poling, lithium content, precursors used and correlated with its performance in a composite. Based on this set of data, an optimized powder was obtained which can be scaled-up in production.

The second objective of thesis is to perform mechanical tests on this optimized powder as a composite to test its viability when employed in a flexible haptic feedback application in-terms of the feedback that will be perceived based on the stiffness of the composite, flexibility in the composite and its piezoelectric performance. From these tests, the optimized powder was seen to be the most ideal for haptic feedback applications when it was employed as an R50 (random composite with 50 % filler and 50 % polymer) composite with no glass fibres used during production.

*(This page was intentionally left blank)*



# Contents

Preface .....	5
Acknowledgements .....	6
Abstract .....	7
Contents .....	9
List of figures .....	13
List of tables .....	17
List of abbreviations and symbols .....	18
1 Introduction.....	20
1.1 Summary .....	20
1.2 Research objective .....	20
1.3 Problem statement .....	21
1.4 Background on flexible haptic feedback devices .....	21
2 Theoretical background .....	22
2.1 Introduction to piezoelectricity .....	22
2.2 History .....	22
2.3 Characterization of piezoelectricity .....	24
2.4 Types of piezoelectric materials .....	25
2.4.1 Single Crystals.....	26
2.4.2 Polycrystalline electroceramics and ferroelectricity .....	26
2.4.3 Piezopolymers .....	30
2.4.4 Piezocomposites.....	33
2.5 PZTs .....	35
2.5.1 MPB .....	35
2.5.2 Processing.....	36
2.5.3 Compositional modifications .....	36
2.5.4 Toxicity .....	36

2.6 Lead-free piezoelectric materials .....	37
2.6.1 Considerations for alternatives .....	37
2.6.2 Issues with KNN-based piezoceramics and possible solutions .....	39
2.6.3 Li doping in KNN .....	41
2.7 Motivation and description of experiments .....	42
2.7.1 Agglomerate size variation and determination of poling settings.....	42
2.7.2 Calcination temperature variation .....	43
2.7.3 Dwelling time variation .....	43
2.7.4 Ball-milling analysis .....	44
2.7.5 Casting method analysis.....	44
2.7.6 Precursor optimization.....	44
2.7.7 Poling method analysis.....	44
2.7.8 Mechanical testing .....	45
3 Experimental methods .....	46
3.2 Production method of ceramic and composites.....	46
3.2.1 Ceramic production.....	46
3.2.2 Composite production.....	48
3.2.3 Poling the composite.....	50
3.2.4 Storage .....	52
3.2.5 Analytical methods.....	52
4 Results and discussion.....	58
4.1 Study of poling conditions, agglomerate size and Li content .....	58
4.1.1 Poling settings variation .....	58
4.1.2 Comparison of performance .....	59
4.1.3 KNLN-6 vs KNLN-3 .....	59
4.1.4 Surface roughness and waviness .....	59
4.2 Calcination study.....	61
4.2.1 First calcination temperature variation .....	61

4.2.2 First calcination dwelling time variation .....	62
4.2.3 Phase purity.....	63
4.2.4 Surface waviness .....	66
4.3 Particle size analysis.....	67
4.3.1 First calcination temperature variation .....	67
4.3.2 First calcination dwelling time variation .....	70
4.4 Particle size distribution analysis .....	73
4.4.1 First calcination temperature variation .....	73
4.4.2 First calcination dwelling time variation .....	75
4.5 Ball-milling analysis.....	78
4.6 Agglomeration variation analysis.....	84
4.7 Composite synthesis method analysis .....	88
4.8 Precursor optimization .....	90
4.9 Poling method analysis .....	92
4.10 Mechanical testing.....	94
4.10.1 Tensile testing .....	94
4.10.2 Torsional testing.....	96
5 Conclusions and future work .....	98
5.1 Conclusions .....	98
5.1.1 Study of poling conditions, agglomerate size and Li content .....	98
5.1.2 Calcination study .....	98
5.1.3 Microstructure analysis.....	98
5.1.4 Ball-milling analysis .....	98
5.1.5 Agglomeration variation analysis.....	99
5.1.6 Composite synthesis method analysis .....	99
5.1.7 Precursor optimization.....	99
5.1.8 Poling method analysis.....	99
5.1.9 Mechanical testing .....	99

5.2 Future work.....	99
Appendix-A: Bibliography.....	101
Appendix-B: Sample descriptions.....	108
B1: Poling study samples .....	108
B2: First calcination temperature variation samples.....	108
B3 Dwelling time variation samples.....	109
B4 Ball-milling samples .....	109
B5 Agglomerate comparison samples .....	109
B6 Mechanical testing samples.....	110
B7 Particle size distribution samples .....	111
B8 Poling method variation samples .....	111

# List of figures

Figure 1: Crystal structure of Quartz containing Silicon (Orange) and Oxygen (Blue) atoms in a non-centrosymmetric structure [4] .....	22
Figure 2: Direct (left) and inverse (right) piezoelectric effects visualized on the crystal structure of quartz [4] .....	22
Figure 3: Naturally produced tourmaline crystal .....	23
Figure 4: Perovskite structure of barium titanate. Blue atoms represent barium; red atoms represent oxygen and black atoms represent titanium [9].....	23
Figure 5: The change in research interests of piezoelectric materials over the years and the corresponding $d_{33}$ associated with the materials [13].....	24
Figure 6: Direct (left) and inverse (right) piezoelectric effects in a bulk ceramic [15].....	24
Figure 7: Axes nomenclature in piezoelectricity [4].....	25
Figure 8: General structure of crystalline (left), polycrystalline (centre) and amorphous (right) solids [4] .....	26
Figure 9: Weiss domains and their respective polarizations present in them [21] .....	26
Figure 10: Mechanism of piezoelectricity exhibited in materials with a perovskite structure at $T > T_c$ (left) and $T < T_c$ (right) [4] .....	27
Figure 11: Change in crystal structure with temperature as seen for BT [4] .....	27
Figure 12: Unpoled (left), poled (centre) and depoled (right) Weiss's domains [21] .....	28
Figure 13: Hysteresis loop generated in a piezoelectric material during poling [28] .....	28
Figure 14: Crystalline and amorphous regions of PVDF [32] .....	29
Figure 15: Increase of mean grain size with sintering temperature for an undoped PZT (52/48) [33] .....	29
Figure 16: Schematic of ceramic powder preparation [4] .....	30
Figure 17: Sintering process as depicted by the change in microstructure [35].....	30
Figure 18: $\alpha$ -form (left) and $\beta$ -form (right) of PVDF [32] .....	31
Figure 19: Hysteresis loops of PVDF-TrFE and PVDF-TrFE-CFE [55] .....	32
Figure 20: Connectivity patterns exhibited in a dual-phase composite [57] .....	33
Figure 21: Comparison of actuation potential for piezoelectric ceramics, polymers and composites .....	34
Figure 22: Perovskite structure of PZTs in non-piezoelectric (left) and piezoelectric (right) states [68] .....	35
Figure 23: Phase diagram of $Pb(Zr,Ti)O_3$ [69] .....	35
Figure 24: Types of domain orientations in (a) Cubic, (b) Orthorhombic, (c) Tetragonal states in perovskite structures [70] .....	36
Figure 25: Classification of elements in the periodic table based on the cost and toxicity [81] .....	37
Figure 26: Difference between (a) MPB and (b) PPT in-terms of the dependence on the temperature and composition [81] .....	38
Figure 27: Phase diagram of KNN ceramics [87] .....	39
Figure 28: Effect of substitution by different elements on KNN ceramics on the $T_c$ and $T_{O-T}$ [90] .....	40
Figure 29: Comparison of $d_{33}$ based on $T_c$ for lead-free and lead-based piezoceramics [83] .....	41
Figure 30: Comparison of $d_{33}$ of random and DEP structured particular piezocomposites with increasing Li content [59] .....	41
Figure 31: Average grain variation vs dwelling/sintering time in KNN ceramics [106].....	43
Figure 32: Ball-milling apparatus.....	46
Figure 33: Sintering oven (a) and sintered sample after first calcination in oven (b).....	46
Figure 34: Sample after hand-milling and sieving.....	47
Figure 35: Sample after second calcination .....	47
Figure 36: Composite solution after solution casting .....	48

Figure 37: Composite sample after drying and annealing .....	49
Figure 38: Micro-compounding twin screw extruder .....	49
Figure 39: Magnetron sputterers for poling (a) and SEM (b) .....	50
Figure 40: Sample before (left) and after (right) gold sputtering .....	50
Figure 41: Poling set-up (a) with amplifier (red arrow), poling stage (green arrow) and poling bath (blue arrow) and poling stage (b).....	51
Figure 42: Corona poling unit.....	52
Figure 43: XRD apparatus.....	52
Figure 44: SEM.....	53
Figure 45: LCR meter (a) and Berlincourt meter (b).....	54
Figure 46: Particle size analyzer .....	54
Figure 47: Confocal microscope.....	55
Figure 48: DSC apparatus .....	55
Figure 49: DMA apparatus .....	56
Figure 50: Rheometer .....	56
Figure 51: $d_{33}$ of the samples with different agglomerate sizes and Li doping.....	58
Figure 52: SEM image (100x magnification) of KNLN-6 piezocomposite cross-sections with 63-125 $\mu\text{m}$ agglomerate size (a) and <63 $\mu\text{m}$ agglomerate size (b).....	59
Figure 53: $d_{33}$ vs (a) average $W_a$ and (b) $R_a$ for the samples in the poling study; (c) primary (green), roughness (blue), waviness (red) profiles of higher sized agglomerate KNLN-6 sample and (d) composite discs made with 63-125 $\mu\text{m}$ (left) and <63 $\mu\text{m}$ agglomerate sizes.....	60
Figure 54: $d_{33}$ vs $C_1$ temperatures of samples with $C_1$ dwelling time of 1 hour .....	61
Figure 55: $d_{33}$ vs $C_1$ temperature of the samples for $C_1$ dwelling times of 1 hour and 3 hours .....	62
Figure 56: XRD results shown for samples with $C_1 = 750^\circ\text{C-1 h}$ , $950^\circ\text{C-1 h}$ , $1050^\circ\text{C-1 h}$ , and $1150^\circ\text{C-1 h}$ after $C_1$ and $C_2$ ( $925^\circ\text{C-10 h}$ ) .....	63
Figure 57: DSC results of samples with $C_1 = 750^\circ\text{C-1 h}$ ; $950^\circ\text{C-1 h}$ ; $1150^\circ\text{C-1 h}$ after $C_1$ (a) and after $C_2$ ( $925^\circ\text{C-10 h}$ ) (b) .....	64
Figure 58: XRD results of the samples with $C_1 = 950^\circ\text{C-1 h}$ ; $950^\circ\text{C-3 h}$ ; $1050^\circ\text{C-1 h}$ and $1050^\circ\text{C-3 h}$ after $C_1$ and $C_2$ ( $925^\circ\text{C-10 h}$ ).....	65
Figure 59: DSC results of the $C_1$ dwelling time variation samples after $C_2$ ( $925^\circ\text{C-10 h}$ ) .....	66
Figure 60: $d_{33}$ vs the average $W_a$ for the $C_1$ temperature variation samples (a) and $C_1$ dwelling time variation samples (b) .....	67
Figure 61: Grains of KNLN-3 visualized with SEM (5000x magnification) for three $C_1$ temperatures after $C_1$ and $C_2$ ( $925^\circ\text{C-10 h}$ ): $C_1 = 750^\circ\text{C-1 h}$ after $C_1$ (a), $C_1 = 750^\circ\text{C-1 h}$ after $C_2$ (b); $C_1 = 950^\circ\text{C-1 h}$ after $C_1$ (c), $C_1 = 950^\circ\text{C-1 h}$ after $C_2$ (d); $C_1 = 1150^\circ\text{C-1 h}$ after $C_1$ (e), $C_1 = 1150^\circ\text{C-1 h}$ after $C_2$ (f) .....	68
Figure 62: Sintered agglomerates visualized with SEM (50x magnification) for three $C_1$ temperatures after $C_1$ and $C_2$ ( $925^\circ\text{C-10 h}$ ): $C_1 = 750^\circ\text{C-1 h}$ after $C_1$ (a), $C_1 = 750^\circ\text{C-1 h}$ after $C_2$ (b); $C_1 = 950^\circ\text{C-1 h}$ after $C_1$ (c), $C_1 = 950^\circ\text{C-1 h}$ after $C_2$ (d); $C_1 = 1150^\circ\text{C-1 h}$ after $C_1$ (e), $C_1 = 1150^\circ\text{C-1 h}$ after $C_2$ (f) .....	69
Figure 63: Grains of KNLN-3 visualized with SEM (5000x magnification) for two $C_1$ temperatures under two $C_1$ dwelling times after $C_1$ and $C_2$ : $C_1 = 950^\circ\text{C-1 h}$ after $C_1$ (a), $C_1 = 950^\circ\text{C-1 h}$ after $C_2$ (b); $C_1 = 950^\circ\text{C-3 h}$ after $C_1$ (c), $C_1 = 950^\circ\text{C-3 h}$ after $C_2$ (d); $C_1 = 1050^\circ\text{C-1 h}$ after $C_1$ (e), $C_1 = 1050^\circ\text{C-1 h}$ after $C_2$ (f) and $C_1 = 1050^\circ\text{C-3 h}$ after $C_1$ (g), $C_1 = 1050^\circ\text{C-3 h}$ after $C_2$ (h).....	71
Figure 64: Sintered agglomerates of KNLN-3 powder visualized with SEM (50x magnification) for two $C_1$ temperatures under two $C_1$ dwelling times after $C_1$ and $C_2$ : $C_1 = 950^\circ\text{C-1 h}$ after $C_1$ (a), $C_1 = 950^\circ\text{C-1 h}$ after $C_2$ (b); $C_1 = 950^\circ\text{C-3 h}$	

after $C_1$ (c), $C_1 = 950\text{ }^{\circ}\text{C}$ -3 h after $C_2$ (d); $C_1 = 1050\text{ }^{\circ}\text{C}$ -1 h after $C_1$ (e), $C_1 = 1050\text{ }^{\circ}\text{C}$ -1 h after $C_2$ (f) and $C_1 = 1050\text{ }^{\circ}\text{C}$ -3 h after $C_1$ (g), $C_1 = 1050\text{ }^{\circ}\text{C}$ -3 h after $C_2$ (h) .....	72
Figure 65: PSD curves of volume density (%) vs the size classes ( $\mu\text{m}$ ) for the $C_1$ temperature variation samples after $C_1$ (a) and after $C_2$ (b) .....	74
Figure 66: $D_{10}$ (a); $D_{50}$ (b) and $D_{90}$ (c) vs $C_1$ temperature of the calcination study samples .....	75
Figure 67: PSD curves of volume density (%) vs the size classes ( $\mu\text{m}$ ) for the $C_1$ dwelling time variation samples after $C_1$ (a) and after $C_2$ (b) .....	76
Figure 68: Variation of $D_{10}$ (a); $D_{50}$ (b) and $D_{90}$ (c) for the $C_1$ dwelling time variation samples .....	77
Figure 69: SEM images of the microstructure with 5000x magnification at different instances in the processing route of the ceramic: (a) After $C_1$ of precursors, before any ball milling; (b) After $C_2$ with no ball-milling done on sample in (a); (c) After ball-milling performed on sample in (a); (d) Sample from (c) after $C_2$ ; and (e) After ball-milling performed on sample in (d) .....	79
Figure 70: SEM images of the sintered agglomerates with 50x magnification at different instances in the processing route of the ceramic: (a) After $C_1$ of precursors, before any ball milling; (b) After $C_2$ with no ball-milling done on sample in (a); (c) After ball-milling performed on sample in (a); (d) Sample from (c) after $C_2$ and (e) After ball-milling performed on sample in (d) .....	80
Figure 71: Volume density (%) vs size classes ( $\mu\text{m}$ ) of particles present in the sample after each calcination and ball-milling process .....	81
Figure 72: (a) $D_{10}$ , (b) $D_{50}$ , and (c) $D_{90}$ vs the sample after 'x' process (BM: ball-milling) .....	82
Figure 73: $d_{33}$ vs average $W_a$ for the samples prepared with different amounts of ball-milling .....	83
Figure 74: Variation of $d_{33}$ with respect to the agglomerate size present in the powder .....	84
Figure 75: Cross-sectional images from SEM (200x magnification) of the $>125\text{ }\mu\text{m}$ (a); $63\text{-}90\text{ }\mu\text{m}$ (b) and $25\text{-}63\text{ }\mu\text{m}$ (c) agglomerate size samples .....	85
Figure 76: Composite samples made with (a) $63\text{-}90\text{ }\mu\text{m}$ and (b) $>125\text{ }\mu\text{m}$ agglomerate size ceramic powders .....	85
Figure 77: Top surfaces of (a) $63\text{-}90\text{ }\mu\text{m}$ and (b) $>125\text{ }\mu\text{m}$ agglomerate size sample when viewed in SEM at 50x magnification .....	86
Figure 78: $d_{33}$ vs average $W_a$ for the agglomerate sizes present in the sample .....	86
Figure 79: $d_{33}$ normalized with the thickness of the composites vs the agglomerate sizes present in the ceramic .....	87
Figure 80: Solution cast (left) and hot-pressed (right) R40 composites of KNLN-3 and CFE .....	88
Figure 81: Cross-section images of the solution-cast (a) and hot-pressed (b) composite made with KNLN-3 ceramic as seen through SEM (2000x magnification) .....	88
Figure 82: $d_{33}$ vs average $W_a$ for the hot-pressed and solution cast R40 KNLN-3/CFE composites compared with the solution cast R50 KNLN-3/CFE composite .....	89
Figure 83: Top surface of (a) solution-cast and (b) hot-pressed R40 composite samples viewed through SEM at 100x magnification .....	89
Figure 84: $d_{33}$ vs relative density of the R40 hot-pressed and R40, R50 solution-cast composite samples .....	90
Figure 85: XRD curves of the KNLN-3 powders made with less pure and more pure $\text{Nb}_2\text{O}_5$ after $C_1$ and $C_2$ .....	91
Figure 86: Microstructure of 99.99 % pure $\text{Nb}_2\text{O}_5$ (a) and 99.9 % pure $\text{Nb}_2\text{O}_5$ (b) visualized with SEM at 5000x magnification .....	92
Figure 87: $d_{33}$ vs the KNLN-3 samples made with less pure and more pure $\text{Nb}_2\text{O}_5$ .....	92
Figure 88: $d_{33}$ vs calcination temperature of samples poled with contact and corona poling .....	93
Figure 89: $d_{33}$ of the contact and corona poled samples vs their respective $C_1$ temperatures after normalizing with composite thickness .....	94
Figure 90: Stress vs strain curves (a) and Young's modulus vs ceramic filler amount (b) for all the samples tested in DMA .....	95

Figure 91: R0 sample at beginning of tensile test (a); R0 sample at end of tensile test (b); R60 sample at beginning of tensile test (c); R60 sample at end of tensile test (d) .....	95
Figure 92: Normal force vs ceramic filler loadings for all the mechanical testing samples taken with and without glass fibres.....	96
Figure 93: 0% ceramic filler loading sample without (a) and with (b) glass fibres .....	97



# List of tables

Table 1: List of piezoelectric ceramics with a distinct phase at room temperature [81].....	38
Table 2: Polymer phases previously used displayed alongside their Young’s moduli and dielectric constants.....	42
Table 3: Agglomerate comparison samples .....	108
Table 4: C <sub>1</sub> temperature variation samples .....	108
Table 5: Dwelling time variation samples .....	109
Table 6: Nano-fragment analysis composite samples.....	109
Table 7: Agglomerate comparison study composite samples .....	109
Table 8: Mechanical testing composite samples .....	110
Table 9: Particle size distribution powders .....	111
Table 10: Corona poling samples .....	111

# List of abbreviations and symbols

PZT	Lead zirconium titanate
KNN	Potassium sodium niobate
PVDF	Polyvinylidene difluoride
KNLN	Lithium doped potassium sodium niobate
MLA	Multi-layer actuator
BNT	Bismuth sodium titanate
BT	Barium titanate
BLSF, BLS	Bismuth layered structured ferroelectrics
$d_{33}$	Piezoelectric charge constant quantifies volume change under an applied electric field when both field and volume change are measured in the same direction
D, P	Polarization
E	Electric field
Y, E	Young's modulus
T	Stress
$s^E$	Compliance
S	Strain
g	Piezoelectric voltage constant quantifies volume change under an applied voltage
$\epsilon$	Dielectric constant
$\tan(\delta)$	Dielectric loss
$T_c$	Curie temperature
t	Goldschmidt tolerance factor
$P_r$	Retained polarization
$E_c$	Coercive field
$T_g$	Glass transition temperature
ITO	Indium Tin oxide
PVDF-TrFE	Poly(vinylidene difluoride-trifluoroethylene)
PVDF-TrFE-CFE, CFE	Poly(vinylidene difluoride-trifluoroethylene-chlorofluoroethylene)
R	Size ratio
DEP	Dielectrophoresis
MPB	Morphotropic boundary
TTB	Tetragonal tungsten bronze
PPT	Polymorphic phase transition
$T_{O-T}$	Orthorhombic to tetragonal phase transition
SPS	Spark plasma sintering
KNLN-3	3 % lithium doped potassium sodium niobate

KNLN-6	6% lithium doped potassium sodium niobate
RPM	Revolutions per minute
DMF	Dimethylformamide
R50	Random 50% volume ceramic filler composites
D.C.	Direct current
SEM	Scanning electron microscopy/e
XRD	X-ray powder diffraction
LCR	Inductance, capacitance, resistance
$\lambda_c$	Cut-off wavelength
DSC	Differential scanning calorimetry
DMA	Dynamic mechanical analysis
$R_a$	Average line roughness
$W_a$	Average line waviness
$C_1$	First calcination
$C_2$	Second calcination
PSD	Particle size distribution
$D_x$	Maximum of the sizes of particles present in the sample occupied by the x% of the particles present
BM	Ball-milling
THF	Tetrahydrofuran
DEP	Diethyl phthalate
$F_N$	Normal force
BET	Brunauer, Emmett and Teller
TEM	Tunelling electron microscopy
FTIR	Fourier-transform infrared spectroscopy

# 1 Introduction

## 1.1 Summary

Piezoelectric ceramics have had wide-spread use in many daily applications like communication, aerospace, medical, and many more sectors. These ceramics typically involve the use of lead-based ferroelectric compounds such as lead zirconium titanate (PZT) which are sintered at high temperatures to produce the ceramic. However, the production of these ceramics requires lead-oxide, which is highly toxic and harmful to the environment. Hence, there has been a push towards producing more environmentally-friendly and less toxic lead-free alternatives whilst having the same performance in applications. One family of ceramics which was found to be a promising alternative to PZTs is the doped potassium sodium niobate (KNN) systems. In particular the lithium doped members of this family (so called KNLN ceramics) have shown great promise and will be the focus of the research.

Ceramics, due to their high rigidity and brittle nature, are not suitable for applications that require high flexibility or will lead to high stresses such as in flexible haptic devices. Piezopolymers on the other hand are flexible but have a number of drawbacks such as the requirement for high fields and mechanical stretching to activate the material and it still shows considerably lower piezoelectric performance than the piezoceramics. In order to improve the feasibility of piezoelectric materials for future flexible haptic feedback devices, composites of piezoceramic powders in a flexible polymer matrix are currently being developed to combine the high piezoelectric activity of the ceramics with the flexibility of a polymer system. In our work we focus on the design and fabrication of lead-free piezocomposites based on the KNLN system of materials with a PVDF terpolymer (PVDF-TrFE-CFE) matrix that has a high dielectric constant.

The structure of the thesis is as follows: [Chapter-1](#) gives more information on the state of the art of haptic feedback systems, which is the end-goal application for these composites. [Chapter-2](#) will be a discussion on the basics of piezoelectricity, various piezoelectric materials, current state of the art of lead-free piezo-ceramics, feasibility of using KNLN composites in haptic feedback devices and the motivation behind the experiments conducted. [Chapter-3](#) will deal with the manufacturing process of the KNLN ceramic starting from the raw materials until the composite and the experimental methodologies that are associated with during the production, testing and analysis of the composite. This will lead to the results, discussion presented in [Chapter-4](#) and conclusions, future work based on the results in [Chapter-5](#).

## 1.2 Research objective

Currently, piezoelectric devices are dominated by lead-based piezoceramics and their derivatives. The main objective of this work is to optimize a KNLN ceramic for scale-up and test its properties as the active phase of a piezocomposite with a suitable polymer. The secondary objective is to test the mechanical properties relevant for flexible haptic feedback devices using the optimized composite. The identification of key elements in the structure-property relationship within the composites and any potential trade-offs between properties such as roughness, piezoelectric activity, microstructure, porosity, thickness of composite and stiffness will be identified for use in a wider project to develop these materials for flexible haptic feedback devices

These materials, while promising, show a number of problems. One of the main barriers for large scale production of devices made from this composition lies in the limited production of KNLN ceramics. While lab scale synthesis is relatively simple, larger scale synthesis requires significant development to ensure reproducibility and optimum properties. In order to ensure the effective scale up, during this project we shall work in close collaboration with

industry to determine the optimum synthesis at the limits of lab scale to feed into a larger project developing the scale up of this ceramic material and work to characterise the mechanical properties of these composites to allow for device integration.

## 1.3 Problem statement

In order to reach the two previously mentioned general objectives, certain sub-goals need to be met based on the timescale available. For the first objective of scale-up of the KNLN piezoceramics, the first sub-goal is to test the effect of agglomeration and Li doping on the behaviour of random piezocomposites. Also, a study of poling conditions (method, time and voltage) will be done to find a suitable poling set-up. Based on these results, a suitable amount of agglomeration can be introduced into the composites and a full fledged study on the calcination temperatures and dwelling time during calcination can be performed. This is to get information on the relation between the piezoelectric activity and the microstructure of the composites. Additionally, the milling performed after each calcination to obtain a usable powder will also affect the microstructure. Thus, this will also be investigated and from this study an optimum KNLN composition will be selected for scale-up. Furthermore, other experiments which will help in scale-up such as the method of casting the composites, precursors used in forming the KNLN ceramic and the poling method used will be investigated.

In order to reach the second objective, a best version of the KNLN ceramic powder can be selected from the previous studies and used for mechanical testing. Mechanical testing involves tensile testing, and torsional testing. Besides these, surface roughness can also be analyzed for all the samples to make a link between piezoelectric properties and itself.

## 1.4 Background on flexible haptic feedback devices

Haptic technology, simply put, is the technology behind the interaction between humans and technology. It involves the feedback given by the device to the user after an input, to signal a successful input. Thus, the feedback must be sensed and understood by the user in-order to have any tangible interaction. Haptic feedback devices are mainly divided into two types: Contact and non-contact haptic applications. Contact haptic feedback applications will be the focus of this thesis and it involves human-technical interaction through touch. Typical examples of where these devices are used are in: cellphones, touchpads, virtual buttons, interactive holograms etc.

Haptic feedback devices can be made by several means. In this thesis, we will be focusing on actuator based haptic feedback, which involves the bending/vibration of an actuator to give the feedback to the user as a haptic pulse. Nowadays, instead of a single actuator, multi-layered actuators (MLAs) fitted inside a piezoactuator are used to dramatically reduce the driving voltage [1]. An attempt to correlate the magnitude of a stimulus that provided the feedback to user sensation was studied by Tikka *et al.* [2]. It was seen that the acceleration of the haptic stimulus pulse characterized the perceived intensity of the feedback to the user more than any other studied metric. This can be easily changed in a potential haptic device to provide an optimum sensation.

Future market in haptic feedback technology involves more usage of flexible haptic feedback technology. This is due to devices getting more sophisticated in their shape and function which requires flexibility and conformability in the material which will also provide feedback that can be sensed. The state of the art flexible haptic feedback technology involves usage of piezoelectric polymers [3]. The focus of this thesis is to provide valuable information regarding the replacement of piezopolymers with lead-free piezocomposites due to the disadvantages associated with them. These will be explained in more detail in later sections.

## 2 Theoretical background

### 2.1 Introduction to piezoelectricity

The term piezoelectricity originates from the greek word *piezein* (meaning “pressure”) and *ēlektron* (meaning “amber”) and, simply put, involves the conversion of energy from the mechanical domain to the electrical domain (and *vice-versa*). These unique properties arise from the non-centrosymmetric crystalline structure of these materials [4] or lack of an inversion center like in the case of quartz as shown in Figure 1. This causes an uneven distribution of charges within the unit cell leading to the formation of dipoles. Applied strain thus, causes an accumulation of charge across the crystal and effectively couples their mechanical and electrical states [5]. This behaviour can be useful in countless applications such as transducers, sensors, actuators, haptic feedback, and energy harvesting applications. Some of these applications, such as sensors, rely on electric charge storage upon applied stress (known as the direct piezoelectric effect). Others, like actuators, rely on the shape change under an applied voltage (known as the inverse piezoelectric effect). Moreover, many devices, for example ultrasound transducers, rely on both the direct and inverse piezoelectric effects at the same time. These two effects are shown for the same quartz crystal described in Figure 1, in Figure 2.

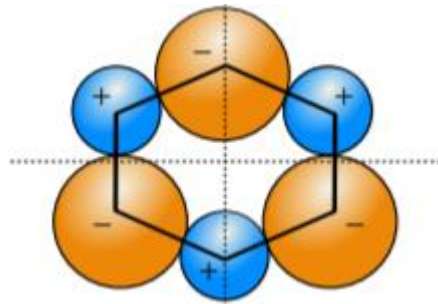


Figure 1: Crystal structure of Quartz containing Silicon (Orange) and Oxygen (Blue) atoms in a non-centrosymmetric structure [4]

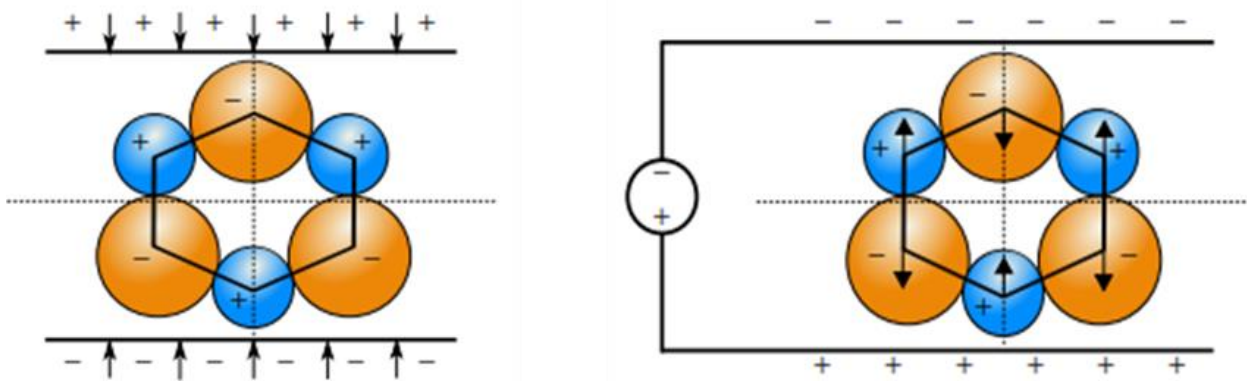


Figure 2: Direct (left) and inverse (right) piezoelectric effects visualized on the crystal structure of quartz [4]

The overwhelming majority of piezoelectric materials are mostly ceramics or single crystals. However, several polymeric materials like Polyvinylidene fluoride (PVDF) and its derivatives have also been shown to exhibit piezoelectricity [4].

### 2.2 History

Research involving piezoelectric materials started in the 17<sup>th</sup> century. During this time, it was seen by merchants in Ceylon, Sri-Lanka that Tourmaline crystals repelled or attracted ash particles when placed in hot-ash. Thus, it garnered the name: “Ceylonese magnet” [6]. Naturally produced tourmaline crystal is shown in Figure 3. These crystals were further studied by scientists and were noticed to generate opposing polarities on either side of the crystals upon a temperature change. This phenomena was termed as pyroelectricity.



**Figure 3: Naturally produced tourmaline crystal<sup>1</sup>**

The first successful description of the piezoelectric effect was demonstrated by Pierre and Jacques Curie on quartz [7]. The inverse piezoelectric effect was later found by Gabriel Lippmann [8] for quartz as well.

Later, the same group of scientists also discovered the piezoelectric effect in Tourmaline and other crystals like Rochelle salt [7]. It was noticed that some piezoelectric materials, like barium titanate exhibited a spontaneous polarization under an externally applied electric field which was reversible. This phenomenon was termed ferroelectricity. Barium titanate crystallises in the perovskite structure (named after the mineral perovskite,  $\text{CaTiO}_3$ , which also has this structure). This structure is shown in Figure 4. It consists of a simple cube of  $\text{Ba}^{2+}$  ions in the corners,  $\text{O}^{2-}$  ions in all the face centres and a  $\text{Ti}^{4+}$  ion in the centre of the  $\text{O}^{2-}_6$  octahedron.

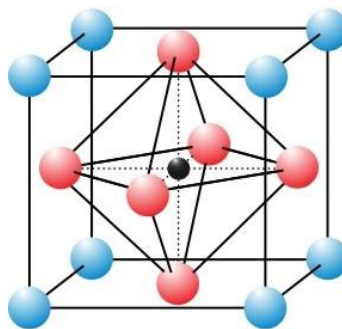


**Figure 4: Perovskite structure of barium titanate. Blue atoms represent barium; red atoms represent oxygen and black atoms represent titanium [9]**

Eventually, it was found that replacing the Ba ions with larger ones such as Pb and mixing large amounts of Zr onto the Ti site could drastically improve the piezoelectric properties, thus the  $\text{PbZr}_{1-x}\text{Ti}_x\text{O}_3$  or lead zirconium titanate (PZT) was produced [10]. These materials are currently the most widely used piezoelectric materials in the industry due to their ease of manufacture, high degree of tuneability (through doping) and high piezoelectric performance.

Recently, the EU council decided to ban the use of lead containing substances in electronics due to the high toxicity and potential for chronic and long term neurological and health impacts, especially in children. The current prescribed safe limit for lead in these devices is 0.8% in weight content [11]. However, PZTs are held as an exception

<sup>1</sup> <https://www.irocks.com/>

to the ban (despite having a lead weight percentage of more than 60%) due to their versatility and the lack of available alternatives. Of principle concern for both the environment and human health is the use of  $\text{Pb}_2\text{O}_5$  in the manufacture of PZTs and also the toxicity generated to the environment upon the disposal of such PZTs. Hence, lead free research has seen a significant resurgence [12]. Several lead-free materials have been studied that could potentially be either a direct replacement to PZTs in their applications or in applications where even PZTs are not useful. These prominently include: KNN (potassium sodium niobate) based materials, BNT (bismuth sodium titanate) based materials, BT (barium titanate) and BLSF (bismuth layered structured ferroelectrics) [12]. The current research focuses on KNN based perovskite ceramics. The historical research direction towards developing better perovskite structured materials is generally considered in terms of the piezoelectric charge coefficient ' $d_{33}$ ' or the charge generated in the same direction as a force is applied. This trend is presented in Figure 5, showing a steady increase since the beginning with  $\text{BaTiO}_3$ . This steady increase in the output of PZTs has been one of the leading difficulties in finding a suitable replacement.

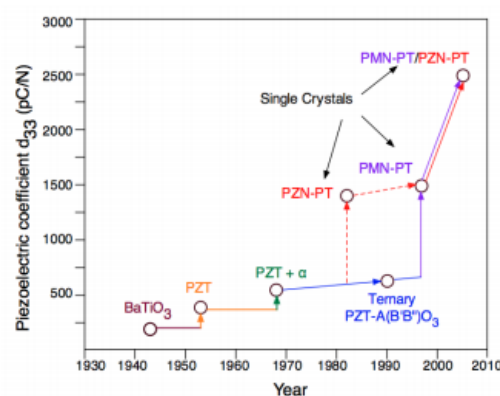


Figure 5: The change in research interests of piezoelectric materials over the years and the corresponding  $d_{33}$  associated with the materials [13]

## 2.3 Characterization of piezoelectricity

In order to better discuss piezoelectricity in-terms of materials, it is necessary to consider the piezoelectric effect in a bulk material rather than a single crystalline unit cell as described before. Both the piezoelectric effects on a bulk piezoelectric material are shown in Figure 6. The direct piezoelectric effect manifests as a polarization on the surface of the material when a mechanical stress is applied on it [14]. Similarly, the inverse piezoelectric effect manifests as a shape change in the entire material when there is an electrical input on the surface of the material.

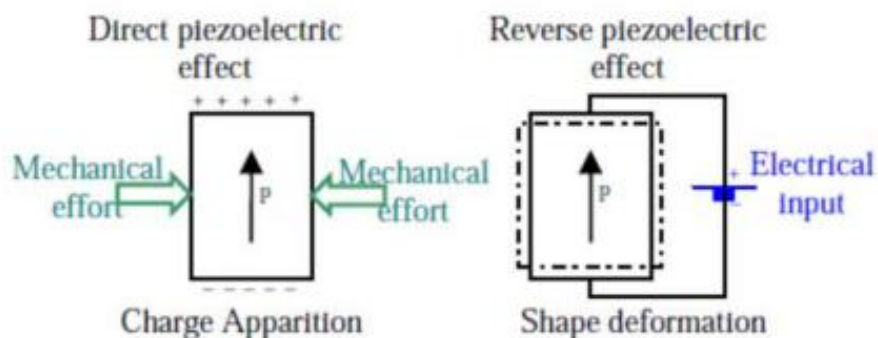


Figure 6: Direct (left) and inverse (right) piezoelectric effects in a bulk ceramic [15]



Apart from dielectric parameters, since piezoelectric materials exhibit electro-mechanical behaviour, the electromechanical term of each effect can be summed up based on the individual electrical and mechanical behaviours of the piezoelectric material. Thus, two sets of equations arise (one for each effect) [4], [16] as shown in equations (1) and (2) below:

$$D = dE + \varepsilon^T Y \quad (1)$$

$$S = s^E T + dE \quad (2)$$

Where D is polarization, E is electric field, Y is young's modulus, T is stress,  $s^E$  is the compliance and S is the strain. The 'd' is known as the piezoelectric charge constant and is the main performance related parameter considered for piezoelectricity. It indicates the charge stored in the material per unit force applied or the strain generated per unit voltage applied. The latter 'd' will be the main quantifying parameter for piezoelectric performance here as we will be dealing with mostly actuator based applications like haptic feedback. Additionally, since the charge stored is not an easily measurable quantity another constant, the piezoelectric voltage constant 'g' is used for sensor based applications. 'g' is proportional to 'd' and inversely proportional to the dielectric constant as shown equation (3) below:

$$g = \frac{d}{\varepsilon} \quad (3)$$

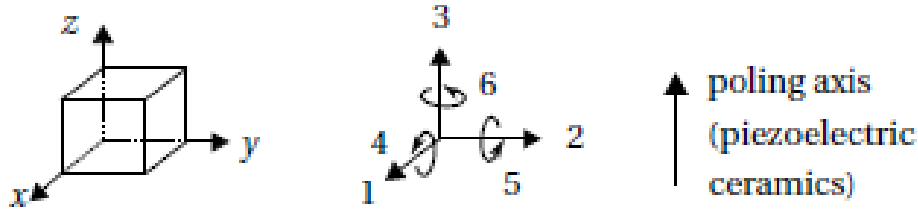


Figure 7: Axes nomenclature in piezoelectricity [4]

The direction and magnitude of deformation in a piezoelectric material depends on the direction and magnitude of the electrical input. As shown in Figure 7, there are six possible response directions in the mechanical domain corresponding to three possible electrical inputs. This corresponds to 18 possible 'd' combinations denoted as  $d_{ij}$ , where 'i' corresponds to the electrical input (1 to 3) and 'j' corresponds to the mechanical response (1 to 3 for axial deformation and 4 to 6 for deformation in shear). For the focus of this thesis, we will be quantifying 'd' as  $d_{33}$  which is the deformation along 3<sup>rd</sup> axis due to an electrical input along the 3<sup>rd</sup> axis. Also, in piezoelectric polycrystalline ceramics, the material needs to be supplied with an external electric field in order to have a bulk piezoelectric effect. This is termed as poling and will be elaborated in [Section-2.4.2.2](#). The 3<sup>rd</sup> axis is also the axis along which the material is poled.

Additionally, losses are also prevalent in piezoelectric materials. In a non-resonant cycle of operation like in actuators, the main type of loss which occurs is the dielectric loss denoted by ' $\tan(\delta)$ ' which denotes the inherent dissipation of electromagnetic energy present within the piezoelectric material [17] due to the influence of various phenomena.

## 2.4 Types of piezoelectric materials

Piezoelectric materials are broadly classified into four types based on their physical and chemical structures: 1. Single crystals, 2. Piezoceramics, 3. Piezopolymers and 4. Piezocomposites.

### 2.4.1 Single Crystals

In single-crystals, a long range order of atoms can be observed without grain boundaries, unlike amorphous solids as shown in Figure 8. In order to exhibit piezoelectricity, crystals must have a non-centrosymmetric structure. Piezoelectric single crystals can be made naturally or artificially like in the case of quartz. While natural quartz is rare, artificial quartz and other single crystals can be grown using hydrothermal synthesis [18] from their polycrystalline counterparts. The processing conditions in the synthesis which typically involves high temperatures and pressures, can be tuned to enable the single crystal to grow in a defect free-way thus, creating the long-range atomic order stated before. Piezoelectric single crystals possess a piezoelectric effect that is natural to their crystal structure and do not need external reorientation of their domains through poling. Quartz single crystals are used in frequency stabilizers in electronics since their operation involves a frequency band very close to the resonant frequency of the device [19]. Other useful examples of piezoelectric single crystals consist of: lithium niobate, PMN-PT and PIN-PMN-PT [20]. These crystals are used in instruments which require low electromechanical energy losses (high coupling coefficient) such as ultrasounds, sonar imaging etc.

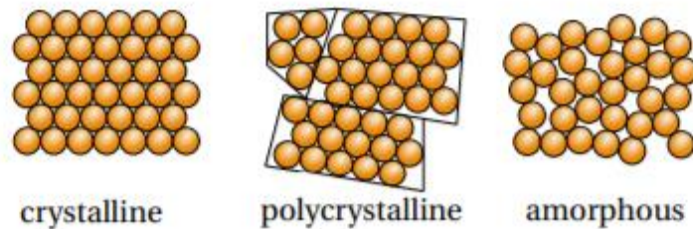


Figure 8: General structure of crystalline (left), polycrystalline (centre) and amorphous (right) solids [4]

### 2.4.2 Polycrystalline electroceramics and ferroelectricity

Polycrystalline ceramic materials, which are shown in Figure 8, can also be piezoelectric if they have a non-centrosymmetric structure in their unit cells. These materials are made of many smaller sized single crystals. Each of these crystals possess domains, known as Weiss domains, which are all randomly oriented in-terms of polarization and thus, provide a net polarization of zero to the bulk material. Weiss domains are shown in Figure 9.

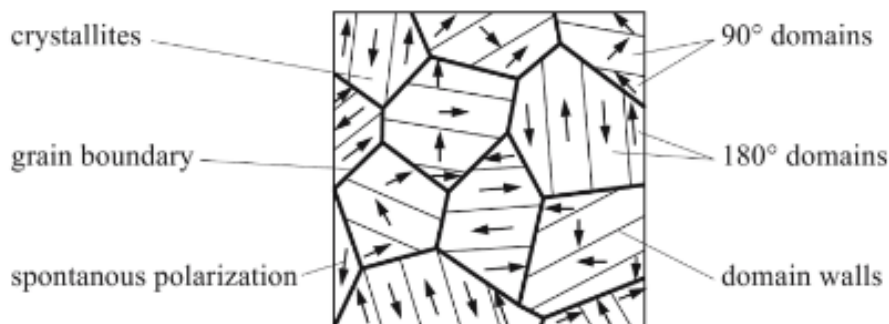


Figure 9: Weiss domains and their respective polarizations present in them [21]

In-order to have a feasible piezoelectric effect, each domain in the crystals must be reoriented towards a desired direction by applying an electric field. Thus, they need to undergo a spontaneous repolarization under an applied

electric field which is termed as ferroelectricity and the materials displaying this behaviour fall into the category of: ferroelectric materials [22]. Perovskite structured materials such as: barium titanate (BT), lead zirconium titanate (PZT) and KNLN (lithium doped sodium potassium niobate) are examples of these types of materials.

Nowadays, most piezoelectric applications use polycrystalline ceramics. These include applications in fields of communications, aerospace, marine, and transport sectors. Some of the specific applications include: motion sensors, watches, ultrasonic power transducers, lithotripters, ultrasonic cleaning, ultrasonic welding, active vibration dampeners, high-frequency loudspeakers, actuators for atomic force microscopes, and many more [23].

#### 2.4.2.1 Perovskites

The general formula for perovskite structures is  $ABX_3$ , where 'A' refers to A-site cations which occupy the vertices of the unit cell; 'X' refers to X-site anions in the face centres of the unit cell (usually oxygen ions) and 'B' refers to B-site cations in the body centre of the unit cell. The piezoelectricity arises from the formation of a non-centrosymmetric structure due to the displacement of the B-site cation along the c-axis as shown in Figure 10 for BT. This displacement arises from a change in the unit cell structure from a cubic structure (non-piezoelectric) to a piezoelectric tetragonal structure. The temperature above which the structure is cubic is the Curie temperature ' $T_C$ '. The change in crystal structure at that temperature is always accompanied by a spike in dielectric constant [24].

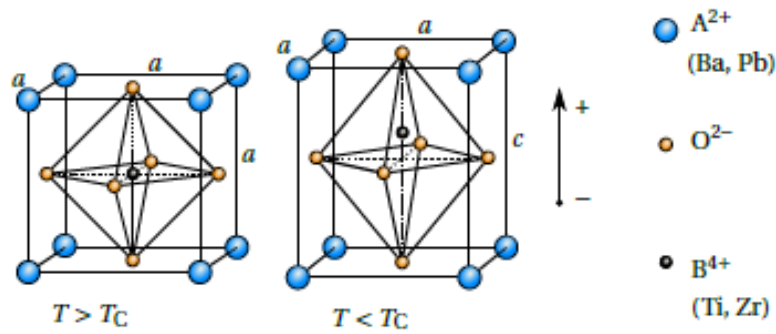


Figure 10: Mechanism of piezoelectricity exhibited in materials with a perovskite structure at  $T > T_C$  (left) and  $T < T_C$  (right) [4]

Furthermore, other structural transitions occur at temperatures below  $T_C$  which also result in the displacement of the B-site ions in different directions that leads to different types of polarizations. These changes in crystal structure with temperature are shown in Figure 11 for BT. The formation of a non-centrosymmetric tetragonal structure (which is critical for ferroelectricity) from the cubic structure is dependent on the radii of the A, B and X ions. Each radii must be the optimum size, such that a shift of the lattice occurs that creates a dipole instead of a rotation of the octahedra [25]. This is defined using the Goldschmidt tolerance factor,  $t$  where  $t = (r_A + r_O) / \sqrt{2}(r_B + r_O)$  [26] (for BT,  $t = 1.06$ ).

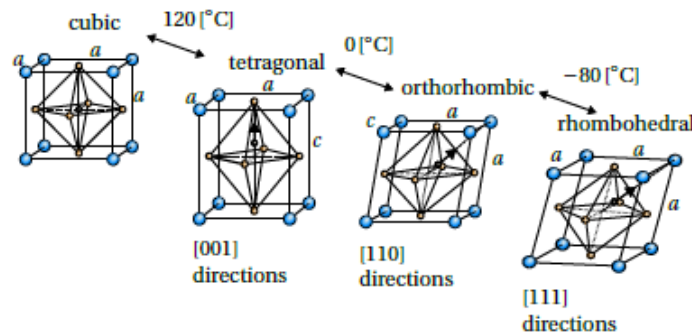


Figure 11: Change in crystal structure with temperature as seen for BT [4]

In general perovskite ferroelectric materials have a much higher piezoelectric effect compared to other piezoelectric materials. This is due to the induced dipole formation and large crystalline distortion by the covalent bonding between the B and X atoms [27].

#### 2.4.2.2 Poling and influencing factors

Ferroelectricity is observed in these materials after reorientation of the Weiss's domains with an external electric field. This process is known as 'poling' as stated before. Poled and unpoled Weiss domains are shown in Figure 12.

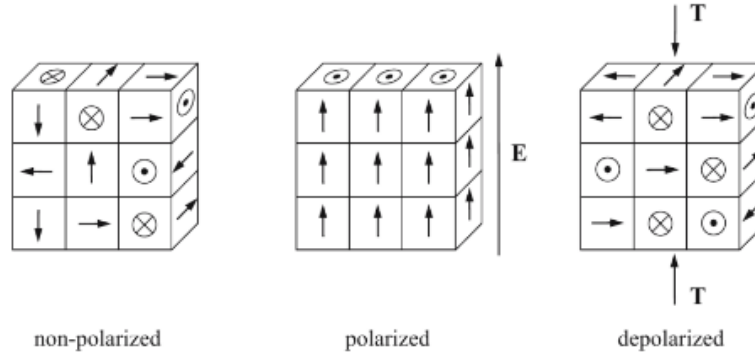


Figure 12: Unpoled (left), poled (centre) and depoled (right) Weiss's domains [21]

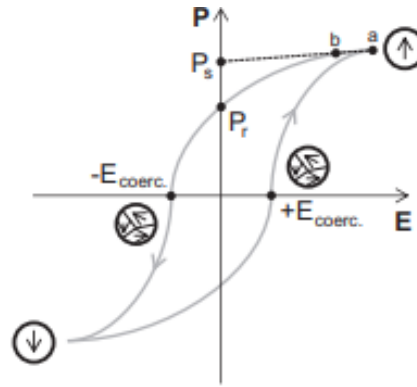


Figure 13: Hysteresis loop generated in a piezoelectric material during poling [28]

The poling process in a ferroelectric material is dependent on both an intrinsic (inherent magnitude of polarization present in the Weiss domains) and an extrinsic effect (reorientation of the Weiss domains due to the external electric field) [29]. The combination of effects produces a non-linear dependence of the polarisation on the electric field that can be described as a hysteresis loop shown in Figure 13. Generally, poling is dependant on the dielectric constant ( $\epsilon$ ) of the material as it dictates the amount of electric field that can permeate through the material.

There is a saturation polarization at which all domains are aligned ( $P_s$ ). Once the electric field is taken away, some polarization is retained. This retained polarization ( $P_r$ ) occurs due to a strain build-up in the domains from their rotation, known as poling strain. The electric field where there is no polarization is known as the Coercive field ( $E_c$ ).

During poling, the poling voltage must be higher than the coercive field of the particular material. The coercive field decreases at higher temperatures due to a higher  $\epsilon$  close to  $T_c$ . This is why poling is mostly done at higher temperature, to reduce the poling voltage that is to be needed. However, the Curie temperature must also be kept in mind, since the material typically starts to depole beyond  $0.5T_c$  and becomes non-piezoelectric at  $T_c$  [4].

A factor to take into account during poling is surface topology of the ceramic or composite. If the sample has a high amount of surface undulations, contact poling will yield varying results within batches of the same sample due to local electric field differences in the surface of the sample [30].

Another factor to take into account during poling are the electrodes that serve as a link to transfer the electric field to the material. The electrode material must be compatible with the piezoelectric material and different electrode materials yield different results during poling. For example, PZTs must be poled with copper electrodes due to compatibility issues with other electrodes but KNLN can be poled with copper and nickel electrodes [31].

Another parameter which affects poling is the crystallinity of the piezoelectric material. Although, polycrystalline ceramics are 100 % crystalline, piezopolymers like PVDF (polyvinylidene difluoride) and derivatives are semi-crystalline in nature. Thus, only the crystalline part of the polymer gets poled. This results in an intrinsic decrease in the piezoelectric response and poling efficiency as only a portion of the material is piezoelectric. The crystalline and amorphous regions of PVDF are shown in Figure 14. Piezopolymers are discussed in Section-2.4.3.

Additionally, doping can also improve the poling efficiencies of certain ceramics. For example, addition of 10-15 % of zirconium in place of titanium in BT converged the three crystal structure transitions present in BT but dramatically increased the dielectric constant thus, providing a single temperature for poling at which there is very low coercive field [4].

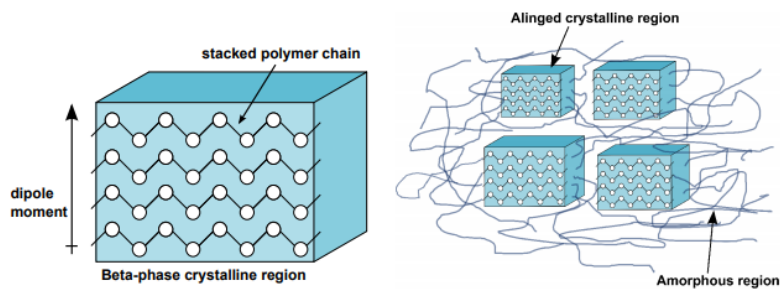


Figure 14: Crystalline and amorphous regions of PVDF [32]

### 2.4.2.3 Influence of microstructure

Ferroelectric materials are also strongly influenced by their microstructure. The size and shape of grains have many effects on the final piezoelectric properties of the material. It was seen from the work done by Randall *et al.* [33], that piezoelectric properties varied significantly with grain size for PZT ceramics. The grain sizes can be changed by varying the sintering temperature, time, and/or the composition. A higher sintering temperature and a longer sintering time aids grain growth. The grain sizes obtained vs the sintering temperature is shown in Figure 15 for a PZT.

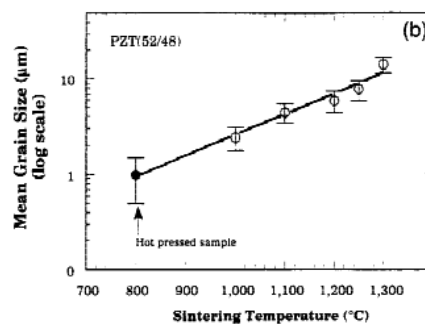


Figure 15: Increase of mean grain size with sintering temperature for an undoped PZT (52/48) [33]

In a study by Huan *et al.* [34], it was found that a peak performance was observed for a perovskite structured ferroelectric BT at a specific grain size of 1-3  $\mu\text{m}$  whereas for smaller and bigger grains, the  $d_{33}$  dropped. It was concluded through the study that higher grain sizes produced more  $90^\circ$  domain walls in the grain which made it difficult to pole whereas smaller grains had similar sizes to the domains themselves causing domain wall clamping which also produced the same effect.

#### 2.4.2.4 Processing route

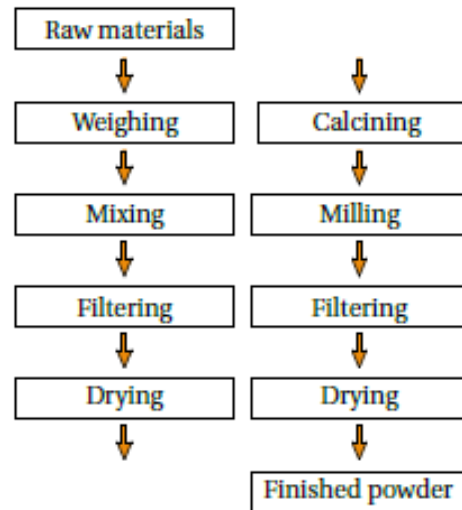


Figure 16: Schematic of ceramic powder preparation [4]

Ferroelectric ceramics are normally prepared via the calcination route depicted in Figure 16. The process starts by weighing the raw material components according to stoichiometric ratios. The raw materials are thoroughly mixed to produce macroscopic homogeneity. The mixture is then calcined in a crucible at a high temperature for a certain time for the solid-state reaction to occur. The ceramic powder forms a dense mass which has high grain size and a high number of agglomerates. These agglomerates are broken down by milling. The now reacted and milled powder is pressed into a compact pellet which has a much lower density compared to the theoretical density. Thus, the cold pressed pellet is put in at high temperatures close to its melting point until full densification occurs. This process is known as sintering. The sintered and unsintered ceramic is depicted in Figure 17.

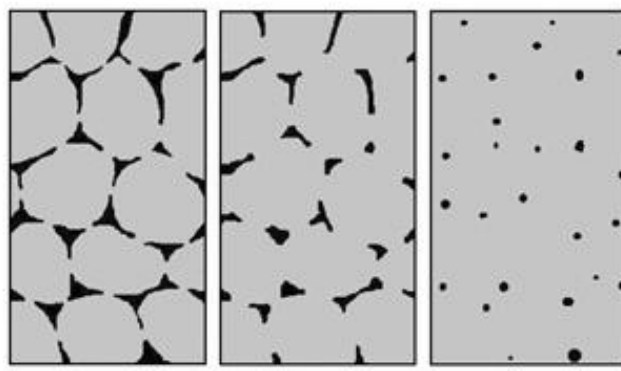


Figure 17: Sintering process as depicted by the change in microstructure [35]

### 2.4.3 Piezopolymers

In piezoceramics and single-crystals, the deformation which can be achieved is very low (below 1 %). This is because of their rigid and brittle structures that are produced from very strong ionic bonds. In piezoelectric applications which require flexibility, piezoelectric polymers are instead used. Piezopolymers are mainly divided into two categories: 1. Piezopolymers with an intrinsic piezoelectricity; and 2. Electrets [36] which are only used in piezoelectric generators. In this work, we will only discuss the former category. This category is further divided into three types: 1. PVDF and its derivatives; 2. Nylon-11; and 3. Polyureas [37]. For our application, PVDF and its derivatives are more relevant due to the highest amount of piezoelectricity present in them compared to the other polymers [38]. Piezopolymers in general have much lower piezoelectric properties compared to piezoceramics. This is attributed in part to their lower crystallinity as most polymers are only 30 %-40 % crystalline. Their semi-crystallinity also imparts a low dielectric constant which in-turn makes them difficult to pole and they have very high coercive fields as a consequence.

#### 2.4.3.1 PVDF

PVDF is a semi-crystalline polymer consisting of alternating hydrogen and fluorine atoms along the carbon backbone. It is produced by the polymerization of its monomer: vinylidene difluoride (VDF). The piezoelectricity typically arises in its  $\beta$ -structure where the fluorine atoms are all on the same side of the backbone thus, producing a polarization across the polymer backbone. The flexibility of the polymer arises from the amorphous phase having a glass transition temperature ( $T_g$ ) below room temperature. Additionally, PVDF also possesses a high dielectric constant compared to other piezoelectric polymers [38].

The piezoelectricity in PVDF was discovered in 1969 by Tanaka *et al.* [39]. It may adopt 4 different forms based on conformation:  $\alpha$ -form,  $\beta$ -form,  $\gamma$ -form and  $\delta$ -form. The most stable form is the  $\alpha$ -form, which is not piezoelectric. Out of the four forms, only two forms are polar and therefore, piezoelectric:  $\beta$ -form and  $\delta$ -form. The  $\delta$ -form is formed by mechanical rotation of the  $\alpha$ -form polymer with the help of a strong electric field [38], [40].

The  $\beta$ -form, which is the most piezoelectric conformation, is obtained by mechanical stretching of the  $\alpha$ -form polymer to 300 %-400 % of its initial length at high temperatures (150 °C) which converts most of the  $\alpha$ -form to the piezoelectric  $\beta$ -form. Later on, the stretched polymer is poled with an electric field of about 30 kV/mm at 90 °C to enhance the piezoelectric properties and also to convert the rest of the  $\alpha$ -form into the  $\beta$ -form [39]. The poled  $\beta$ -form after mechanical stretching is shown in Figure 18 alongside the nonpolar  $\alpha$ -form. The ferroelectricity of PVDF was confirmed by Tamura *et al.* [41]. The ferroelectricity was attributed to the crystalline  $\beta$ -domains being embedded in the amorphous  $\beta$ -domains which acted as a medium for elongation similar to grain boundaries in ceramics [42]. The retainment of polarization occurred due to conformational restriction.

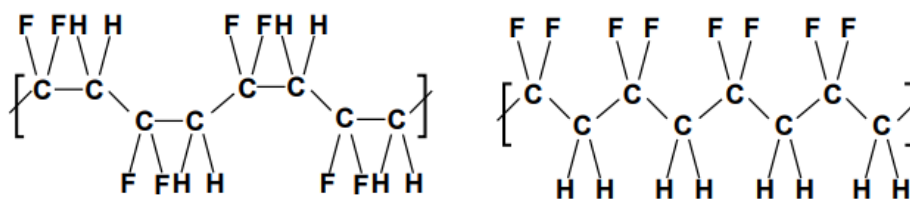


Figure 18:  $\alpha$ -form (left) and  $\beta$ -form (right) of PVDF [32]

Nowadays PVDF is poled in more sophisticated ways which produce a higher piezoelectric response compared to the first piezoelectric PVDF made by Tanaka *et al.* For example, using ITO (indium tin oxide) as electrodes during poling [43] transferred a much higher electric field compared to the conventional metal electrodes without its degradation as poling PVDF requires exceptionally high voltage as stated before.



Additionally, the crystallinity in PVDF can be increased by drawing and rolling processes [44] to provide higher piezoelectric properties. PVDF has been used in several applications like headphones, speakers, microphones, ultrasonic transducers, ultrasounds, visual displays, electric fans and hydrophones [42].

#### 2.4.3.2 PVDF-TrFE

Research was done on producing PVDF-copolymers with the same piezoelectric effect that gave an exact value for the Curie temperature since pure PVDF did not. The initial research points towards copolymerizing VDF with trifluoroethylene (TrFE) to produce the copolymer: PVDF-TrFE. Yagi *et al.* [45], synthesized the copolymer in all compositions and characterized the structures produced. A composition of 50 %-50 % of the monomers was seen to produce a measurable Curie temperature at 70 °C. PVDF-TrFE was confirmed to be ferroelectric by Yamada *et al.* [46] and Davis *et al.* [47]. Furthermore, the piezoelectric charge constant 'd' was measured to be 29 pC/N which was comparable to the initial pure PVDF. Drawing and rolling processes on the PVDF copolymer were investigated by Lovinger *et al.* [48] who noted the increase in crystallinity just like in PVDF.

Apart from the main advantages of having comparable piezoelectric properties and a definite Curie temperature, the copolymers of PVDF are preferred over the pure version due to the fact that their crystallinity and hence, the ferroelectric properties can be obtained directly from the melt, making rolling and drawing more effective [49]. Additionally, PVDF-TrFE also had a higher use temperature compared to PVDF [38]. Properly stretched and poled PVDF-TrFE copolymers have been reported to have a high piezoelectric constant of 38 pC/N [50].

Nowadays, the PVDF-TrFE processing has been optimized for its intended applications like MEMS [51], energy harvesters [52], acousitc applications [32] and many more.

#### 2.4.3.3 PVDF-TrFE-CFE

In an attempt to make materials with high charge storage it was concluded that ferroelectric and non-ferroelectric materials were not suitable [53]. In the research by Zhang *et al.* [54], PVDF-TrFE was radiated with a specific wavelength of light such that it introduced defects in the polymer. This created a relaxor-ferroelectric polymer (ferroelectric materials which produce a high electrostrictive strain). Thus, the material had a lower remnant polarization, slimming the polarization loop as well as increasing the energy density and dielectric constant. This is shown in Figure 19.

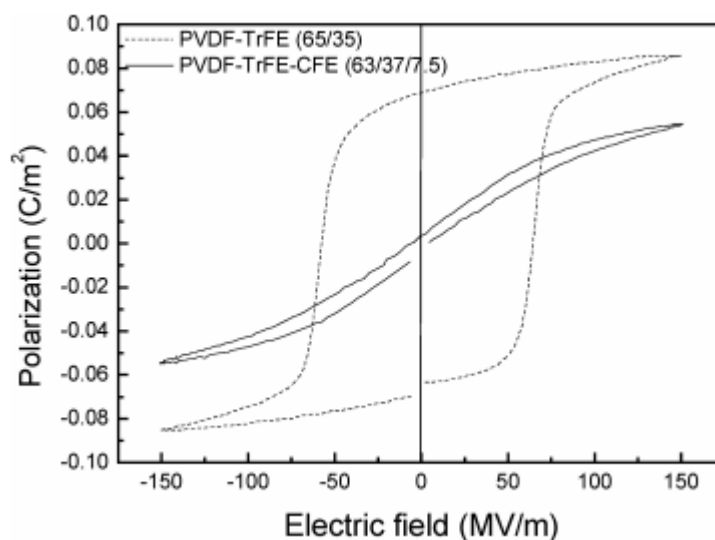


Figure 19: Hysteresis loops of PVDF-TrFE and PVDF-TrFE-CFE [55]



A new method of introducing defects into the PVDF-TrFE matrix was developed by Chu *et al.* [56], where bulky CFE (chloroflouroethylene) groups were introduced as a terpolymer into PVDF-TrFE to produce the same relaxor ferroelectric characteristics. This was known as PVDF-TrFE-CFE terpolymer or simply CFE polymer. These had a dielectric constant of 55 (dimensionless) at room temperature which was much higher than PVDF-TrFE which had around 12 (dimensionless). This is the highest dielectric constant of any commercially available polymer known to date.

## 2.4.4 Piezocomposites

Composites are generally defined as multi-phase mixtures of several components that are macroscopically homogenous in properties. For this study, we deal with two-phase composites consisting of a continuous phase and a filler phase. The filler phase is the active piezoelectric phase and the continuous phase is usually meant for giving the composite: structure and flexibility.

### 2.4.4.1 Connectivity

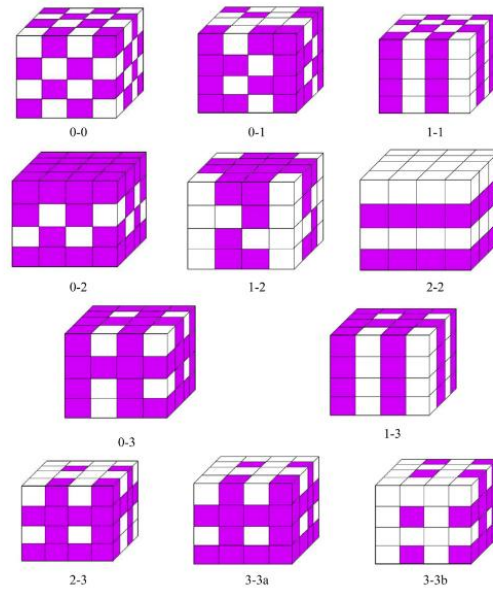


**Figure 20: Connectivity patterns exhibited in a dual-phase composite [57]**

Additionally, apart from the relative amount of the filler phase, the shape, size, orientation and connectivity between other filler particles of the filler come into play in determination of the composite properties [58], [59]. In piezocomposites, connectivity of the ceramic fillers is the property determining step. Generally, there are ten essential connectivity patterns in piezocomposites concerned with ceramic fillers as displayed in Figure 20. In the ten different connectivity patterns, the first number denotes connectivity of the filler and the second, that of the matrix phase. In piezoelectric applications, mostly 0-3 and 1-3 composites are used.

### 2.4.4.2 Why piezocomposites?

Ceramic materials are typically rigid/brittle and have low  $g_{33}$  values. Hence, they cannot be used for flexible haptic feedback applications. Piezoelectric polymers on the other hand, are flexible but have low Curie temperatures and piezoelectric properties. Thus, the ceramics are combined with polymers to give it the flexibility whilst offering an improvement of the piezoelectric properties over those of the polymer systems. This is shown explicitly as  $d_{33}$  vs  $\epsilon$  in Figure 21, for a broad collection of piezoelectric ceramics, polymers and composites.

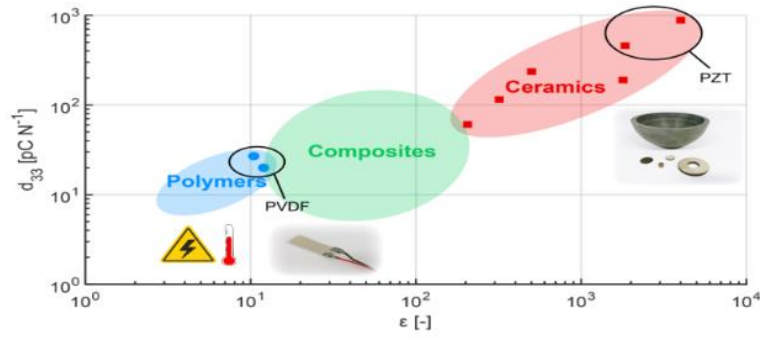


**Figure 21: Comparison of actuation potential for piezoelectric ceramics, polymers and composites<sup>2</sup>**

#### 2.4.4.3 0-3 piezocomposites

0-3 composites (random composites) are essentially the ceramic filler phase randomly distributed in a flexible matrix. They can be easily cast into complex shapes if needed. However, their piezoelectric properties are quite low due to the lack of connectivity between the ceramic particles and potential inhomogeneity in the distribution of filler phase [59]. One of the major problems in piezoelectric composites is an imbalance in the applied electric field which affects the effective field experienced by the ceramic particles [60], [61]. This stems from the mismatch in the dielectric constants of the ceramic and polymeric phases. Therefore, in order to have effective poling scenarios, the difference between the dielectric constants between the two phases must be as low as possible [62]. This is described by Bowen's model shown in equation (4) below:

$$E_{\text{composite}} = \left\{ \frac{(1 + R)\epsilon_1}{\epsilon_2 + R\epsilon_1} \right\} E_{\text{applied}} \quad (4)$$

where,  $R$  is the size ratio of the filler particles which is the ratio between average particle size and inter-particle distance,  $\epsilon_1$  and  $\epsilon_2$  are the dielectric constants of the polymer and the ceramic filler respectively,  $E_{\text{applied}}$  is the applied electric field and  $E_{\text{composite}}$  is the effective electric field that is applied on the whole composite and hence, the ceramic phase. We can see that as  $\epsilon_1$  becomes lesser compared to  $\epsilon_2$ ,  $E_{\text{composite}} = (\epsilon_1/\epsilon_2)E_{\text{applied}}$ , which denotes the electric field imbalance.

In some instances, a dielectric mismatch is preferred to reduce signal-to-noise ratios and increase the sensing capabilities (by lowering  $\epsilon$  such that  $g_{33}$  is increased). This is seen in piezoelectric devices like robotic skins [63] which employ piezoelectric foams [64]. The dielectric mismatch is increased in these foams by having air pockets or porosities.

#### 2.4.4.4 1-3 piezocomposites

1-3 composites (known as structured composites) on the other hand, have complete ceramic filler interconnectivity in one dimension. They are essentially made from rods or fibres of the ceramic filler embedded through the polymer matrix. These composites are made by processes such as: dicing and filling, injection moulding etc [4]. These composites are usually preferred in applications where high reliability is needed such as medical, sonar applications.

#### 2.4.4.5 Structured 0-3 composites

DEP (dielectrophoresis) structured 0-3 composites are another type of composites where-in 0-3 composites are made to mimick the 1-3 composites in-terms of connectivity. This is done by aligning the filler particles before the

<sup>2</sup> Dr. Tadhg Mahon *et al.*, International Symposium on Applied Ferroelectrics (ISAF) 2019, Oral communication

curing of the matrix such that they ideally form percolation paths that replicate the connectivity present in 1-3 composites. These produce much better piezoelectric properties in 0-3 composites [65]. In the study by Stuber *et al.* [66], the previous increase in piezoelectric properties by structuring was further exploited by using ceramic fibres instead of particles which produced even better piezoelectric properties.

## 2.5 PZTs

Most of today's piezoceramics are lead-based ceramics that consist of the primary ceramic structure: lead zirconium titanate ( $\text{Pb}(\text{Zr,Ti})\text{O}_3$ ) or simply PZT. This is a perovskite structure of  $\text{PbZrO}_3$  doped with Ti shown in Figure 22. The ferroelectric states that different compositions of Ti:Zr produce can be illustrated with the help of a phase diagram shown in Figure 23. PZTs had much higher piezoelectric properties than other perovskites due to the presence of 6s orbitals in Pb which are hybridized easily [27] (large atoms like Pb are generally highly polarisable) and contributed to the covalent bonding effect present in perovskites to a greater extent. Apart from their versatility in properties, PZTs also are easy to shape for use in devices through many compatible processes like press moulding, tape moulding, extrusion etc. [67].

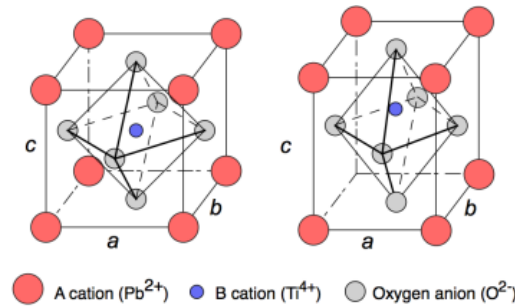


Figure 22: Perovskite structure of PZTs in non-piezoelectric (left) and piezoelectric (right) states [68]

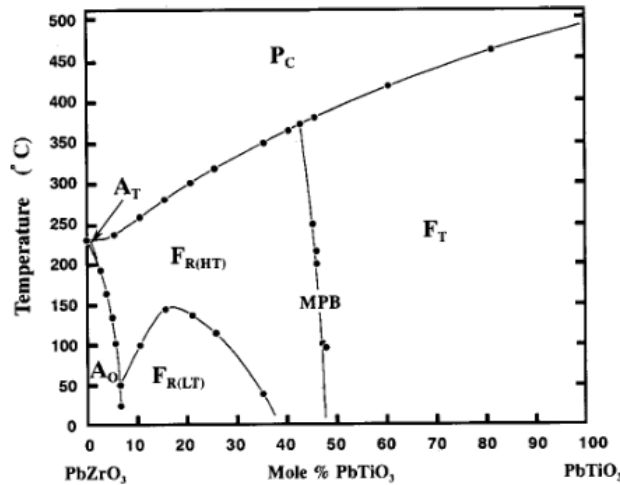
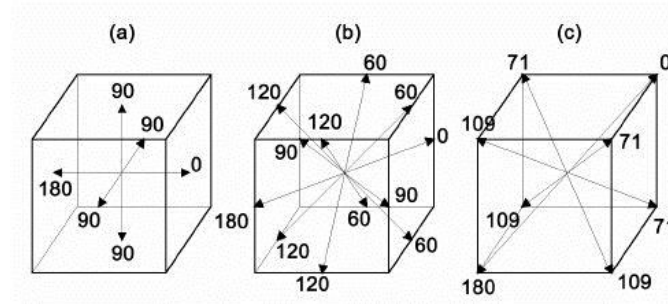


Figure 23: Phase diagram of  $\text{Pb}(\text{Zr,Ti})\text{O}_3$  [69]

### 2.5.1 MPB

The best piezoelectric properties are found with a Zr:Ti ratio of 48:52 which lies in the phase transition region known as the morphotropic phase boundary (MPB) seen in the phase diagram of PZT. This transition separates two phases: rhombohedral and tetragonal phases [4]. An MPB is essentially a phase transition boundary that is almost independent of temperature and only depends on the composition of Zr:Ti.



**Figure 24: Types of domain orientations in (a) Cubic, (b) Orthorhombic, (c) Tetragonal states in perovskite structures [70]**

At the MPB, there are at least 14 different possible orientations as shown in Figure 24 (8 for orthorhombic and 6 for tetragonal). This makes the poling more effective as the grains are able to orient better due to more available orientations thus, increasing the piezoelectric properties. The MPB is observed as a spike in dielectric constants and coupling factors at this specific ratio of Zr:Ti similar to other phase transitions. Noheda *et al.* suggested that the increased number of orientations at the MPB was due to the formation of an intermediate monoclinic phase [71].

## 2.5.2 Processing

PZTs are normally prepared using the conventional milling and calcining process [72]. More efficient processes have been developed that both reduce the time of preparation and the environmental effect that the conventional process has. These include processes such as low temperature sintering [73], hydrothermal precipitation [74], polymeric precursor methods [75].

## 2.5.3 Compositional modifications

PZTs, although having high piezoelectric properties, also have great suitability for a wide variety of piezoelectric applications that each have different requirements. This is due to the highly modifiable composition of PZTs. Compositional modifications are generally of three types: 1. Changing the Zr:Ti ratio, 2. Doping with other elements, 3. Producing ternary perovskites. These are described below:

1. Changing the Zr:Ti ratio is beneficial in applications where the value of the piezoelectric charge constant need not be as high as it can be in the MPB. These are usually done for temperature stability applications where the single phase rhombohedral and tetragonal PZTs perform better than in the MPB composition [67].
2. The second type of compositional modification involves doping. Generally, doping in PZTs are of four types depending on the valency of the dopant ion: Acceptor doping, donor doping, isovalent doping, and compensating doping with each type producing different effects [4], [76], [77].
3. The third type of compositional modification involves combining the PZT perovskite with another type of perovskite for producing a specific set of properties. Since this involves more than two contributing ions (apart from Pb and Ti or Zr), it is termed as a ternary PZT system. Some examples include:  $\text{Pb}(\text{Sb}_{1/2}\text{Nb}_{1/2})\text{O}_3$ – $\text{Pb}(\text{Zr}_{1-x}\text{Ti}_x)\text{O}_3$  [78] which yields good temperature stability,  $\text{Pb}(\text{Mn}_{1/3}\text{Sb}_{2/3})\text{O}_3$ – $\text{Pb}(\text{Zr}_{1-x}\text{Ti}_x)\text{O}_3$  [79] which yields low mechanical loss,  $\text{Pb}(\text{Ni}_{1/2}\text{Nb}_{1/2})\text{O}_3$ – $\text{Pb}(\text{Zr}_{1-x}\text{Ti}_x)\text{O}_3$  [80] which yields a very high 'd'.

## 2.5.4 Toxicity


Lead based ceramics are currently the state of the art in most piezoelectric applications being only rivalled by single crystals in some applications. However, the toxicity of lead is a major concern in today's industrial practices [81]. In the production of PZT, there are two types of toxic effects that pose a health concern: 1. Toxicity of the lead oxide precursor, 2. Toxicity of the disposed PZT which contains lead. Lead is known to leach from both these compounds in

Hence, an official ban on such lead-based materials in electronic applications has already been issued by the EU council [82]. Due to the versatility of PZTs in piezoelectric applications and no viable alternatives, PZTs have been given an exemption from the ban. However, this exception may change with the demands of politics and environmental responsibility. Therefore, there has been marked increase in the research towards other piezoelectric materials (lead-free piezoelectrics) which are safer than lead-based piezoelectric ceramics. The main research direction focuses on improving their properties to make them a viable alternative to the PZTs.

Research into lead-free piezoelectric materials started with five main considerations that will be needed to replace PZTs as the most widely known piezoelectric materials: 1. Cost and toxicity, 2. Crystal structure, 3. Electronic structure of atoms present, 4. Phase diagram and 5. Comparable piezoelectric properties with PZTs

#### 2.6.1.1 Cost and toxicity

	1	2	3	4	5	6	7	8	9	10	11	12	13	14	15	16	17	18
Ia																		VIIa
1 (H)	H	He																He
2 (Li)	Li	Be											B	C	N	O	F	Ne
3 (Na)	Na	Mg	IIIb	IVb	Vb	VIb	VIIb	VIII			lb	IIb	Al	Si	P	S	Cl	Ar
4 (K)	K	Ca	Sc	Ti	V	Cr	Mn	Fe	Co	Ni	Cu	Zn	Ga	Ge	As	Se	Br	Kr
5 (Rb)	Rb	Sr	Y	Zr	Nb	Mo	Tc	Ru	Rh	Pd	Ag	Cd	In	Sn	Sb	Te	I	Xe
6 (Cs)	Cs	Ba	La	Hf	Ta	W	Re	Os	Ir	Pt	Au	Hg	Tl	Pb	Bi	Po	At	Rn
7 (Fr)	Fr	Ra	Ac	Rf	Db	Sg	Bh	Hs	Mt	Ds	Rg	Uub	Uut	Uuq	Uup	Uuh	Uus	Uuo
Lanthanoid																		
Actinoid																		



Cost	< 500\$/kg	> 500; <1000\$/kg	>1000\$/kg
Toxicity	not toxic	slightly toxic	toxic

#### 2.6.1.2 Crystal structure

37

It is also noted that, the temperature of the material (perovskites above  $T_c$  do not exhibit piezoelectricity), coordination number of atoms etc., also play a role in determining whether the system will exhibit piezoelectricity [81]. Variations of the perovskite structure which are also ferroelectric exist. These types are seen in bismuth layered structures (BLS) and lithium niobate. BLS contain a layered perovskite structure and lithium niobate contains a tilted octahedral variant of a conventional perovskite which is uniaxially ferroelectric. Structures other than the perovskites can also exhibit piezoelectricity such as the tetragonal tungsten bronze (TTB) structures with the formula ' $A_xB_2O_6$ '.

### 2.6.1.3 Electronic structure of atoms

From the different perovskite structures produced from the suitable atoms chosen in the previous sections, one can narrow down the order of performance based on the electronic structure of the atoms and determining how much each atom contributes to the piezoelectric effect in the crystal structure. It was found that the PZTs achieved such good properties due to the size and orbital configuration associated with the Pb ion. Thus, any element which has comparable size and polarizability to that of Pb would serve as an effective alternative to PZT.

### 2.6.1.4 Phase diagram

Finally, it was found from the research into PZTs that the presence of an MPB drastically increases piezoelectric properties. Although the presence of an MPB is attractive, it is not present in many lead-free alternatives. Through Gibb's free energy curves, it was realized that a polymorphic phase transition (PPT) exhibits a similar Gibb's free energy curve to that of an MPB and thus, also yields improved piezoelectric properties. The PPT is similar to an MPB, except that the phase transition occurred as a variable with temperature and composition as shown in Figure 26. Based on this, a list of piezoelectric ceramics each having a distinct phase at room temperature were given such that in solid solutions of one or more of them, one can hopefully obtain an MPB or PPT. These are listed in Table 1. Through this list, good piezoelectric properties were discovered for two types of material solid solutions namely: KNN (solid-solution of sodium and potassium niobate) [83] and bismuth-based materials like bismuth sodium titanate and bismuth potassium titanate [84], [85]. For the scope of this thesis, the ferroelectric perovskite of KNN will be the focus.

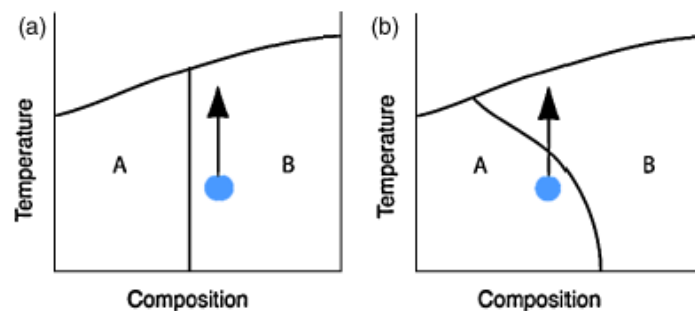


Figure 26: Difference between (a) MPB and (b) PPT in-terms of the dependence on the temperature and composition [81]

Table 1: List of piezoelectric ceramics with a distinct phase at room temperature [81]

Orthorhombic	Tetragonal	Rhombohedral
$\text{KNbO}_3$	$\text{BaTiO}_3$	$\text{Bi}_{1/2}\text{Na}_{1/2}\text{TiO}_3$
$\text{NaNbO}_3$	$\text{Bi}_{1/2}\text{K}_{1/2}\text{TiO}_3$	$\text{BiFeO}_3$



AgNbO <sub>3</sub>	BaCu <sub>1/2</sub> W <sub>1/2</sub> O <sub>3</sub>	BiMg <sub>1/2</sub> Ti <sub>1/2</sub> O <sub>3</sub>
--------------------	---	--

### 2.6.1.5 Comparison of properties with PZTs

KNN ceramics are seen to offer a PPT at approximately 200 °C according to its phase diagram shown in Figure 27. But most KNN based materials do not perform as well as PZTs for the same Curie temperature due to the atoms being not as polarisable. However, the work of Saito *et al.* [86], provided the existence of KNN based materials being a suitable alternative to PZTs in-terms of  $d_{33}$  and hence, research shifted towards KNN based materials. The  $d_{33}$  measured by Saito *et al.* of, 416 pC/N, is higher than actuator grade PZTs for that particular  $T_c$ . However, the method they used to produce the ceramic involves significant doping and templated grain growth methods. These are difficult to replicate commercially in application and so alternative routes to such high  $d_{33}$  values will need to be found. Nevertheless, the study provided a good starting point towards development of KNN based ceramics.

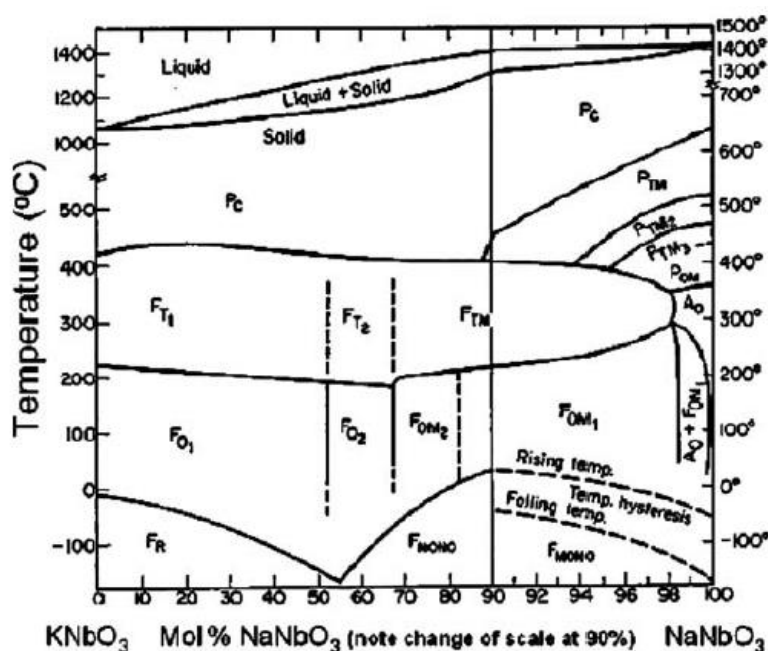


Figure 27: Phase diagram of KNN ceramics [87]

Although with the above mentioned arguments we notice that KNN ceramics seems to be a viable replacement for PZTs, practical implementation of these ceramics have had issues which are related to the inherent properties of KNN [1]. These are summarized in the subsequent subsection.

### 2.6.2 Issues with KNN-based piezoceramics and possible solutions

Apart from the fact that, conventionally sintered KNN have piezoelectric properties much lower than even undoped PZTs [88], [89], the processing of KNN and the exploitation of its PPT also has issues.

The first issue associated with KNN is the volatility of the alkali oxides during sintering. Due to the high sintering temperatures (>1100 °C) needed, alkali precursors evaporate and affect the stoichiometry of the KNN ceramic. Additionally, the loss of alkalis also promotes the formation of a TTB phase which causes abnormal grain growth [89]. Excess alkali precursors added before sintering and slower heating rates seemed to solve the respective issues.

The second issue with KNN-ceramics is their poor densification. This is seen in the work of Li *et al.* [90], where the reduced densification of KNN is attributed to the inherent cuboidal morphology of the ceramic grains. This makes it

intrinsically difficult to sinter these ceramics and achieve full densification. Although densification can be improved by using hot-pressing methods [91] and spark plasma sintering (SPS) [92], for mass production, pressure-less oven sintering is preferred. It was also seen through the works Liu *et al.* [93], Wang *et al.* [94], and Saito *et al.* [95] that faster heating rates, longer dwelling times and Li addition aided densification. Notably, the factors that improve densification are exactly the same ones that lead to alkali evaporation, further complicating the optimisation of these systems.

The third issue of KNN ceramics is associated with the temperature dependence of the PPT where KNN achieves its maximum piezoelectric properties. The temperature at which this phase transition happens, known as  $T_{O-T}$  (as it is the transition from orthorhombic at low temperature to tetragonal at higher temperatures), must be shifted to room temperatures for KNN to have access to its benefits. In the research done by Li *et al.* [90], it was seen that addition of Li in the form of a niobate or antimonate decreased the  $T_{O-T}$  to room temperature with an added benefit of also increasing  $T_C$ , which broadened the usage temperature range. This is shown in Figure 28.

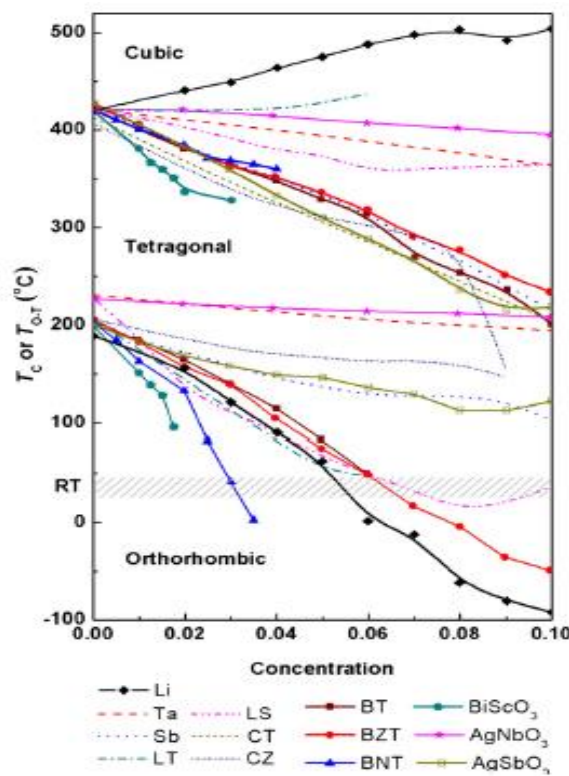


Figure 28: Effect of substitution by different elements on KNN ceramics on the  $T_C$  and  $T_{O-T}$  [90]

The fourth issue with KNN ceramics is their tendency to absorb moisture from the air [95]. The problem was also observed in the precursors of KNN ceramics before the calcination step. The moisture absorption causes high dielectric losses in the ceramic which makes the ceramic difficult to pole and presents a problem for application as its stability is compromised. Storage in vacuum is seen to eliminate this issue but may be impractical for applications.

The above discussion clearly indicates the good properties of doping KNN especially with Li which is associated with: good sinterability, more grain growth, lower  $T_{O-T}$  to produce better piezoelectric properties and higher  $T_C$ . The maximum  $d_{33}$  which was obtained in KNN through pure Li doping was around 200 pC/N [88], [96]. Future studies are still being performed to rival the  $d_{33}$  found by Saito *et al.* at 416 pC/N [97]. However, it is to be noted that these  $d_{33}$  are not even close to the  $d_{33}$  exhibited by soft PZTs which have values above 600 pC/N as shown in Figure 29. However, when it comes to piezoelectric composite materials, lead free piezoceramics such as KNLN perform better



than PZTs due to the lower dielectric mismatch. For this reason lead free materials can be regarded as a viable replacement for PZTs in the development of materials for flexible haptic feedback applications.

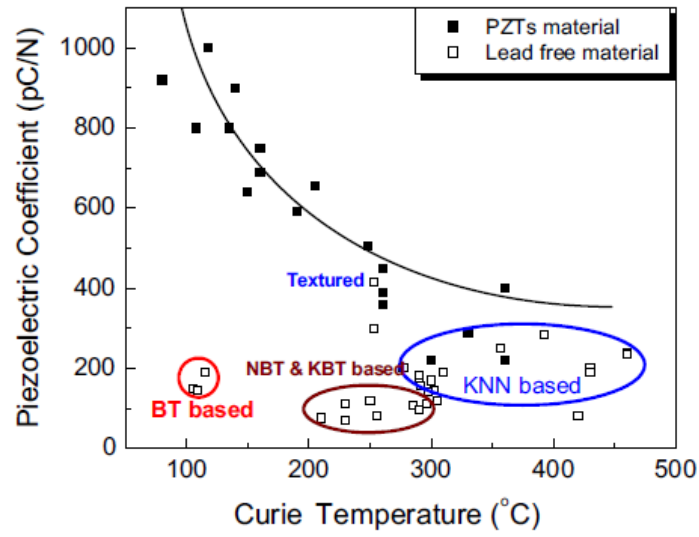


Figure 29: Comparison of  $d_{33}$  based on  $T_c$  for lead-free and lead-based piezoceramics [83]

### 2.6.3 Li doping in KNN

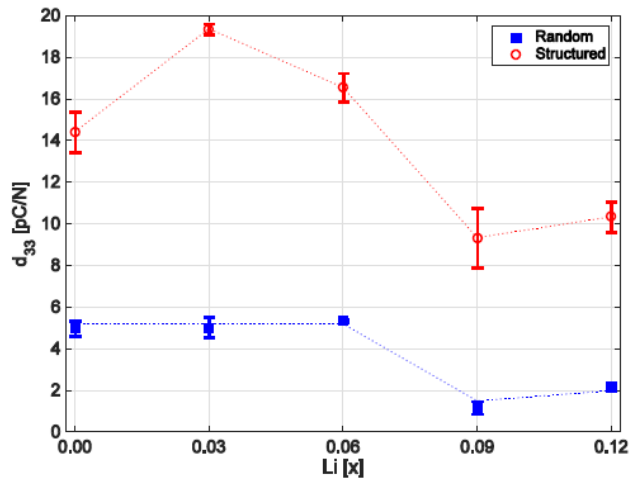


Figure 30: Comparison of  $d_{33}$  of random and DEP structured particular piezocomposites with increasing Li content [59]

Although Li doping was seen to yield better piezoelectric properties, it was unclear at which Li doping amount there was a peak in the properties of the composite. For a ceramic, it was seen that KNLN-6 (6 % mol. of Li addition) gave the best properties due to the reduction of the  $T_{O-T}$  to room temperature thus, utilizing the PPT effect. In a study by Deutz *et al.* [65], it was seen that for random distribution of the fillers, there is no difference in the  $d_{33}$  between composites with low loadings of pure KNN, KNLN-3 and KNLN-6 powders in epoxy. Beyond KNLN-6 however, there is a dip in  $d_{33}$ , as shown in Figure 30. It is likely that, for the random composites, any gains in the  $d_{33}$  from additional Li doping are offset by an increase in the dielectric constant (and thus, the dielectric mismatch in the composite).

Additionally, it was concluded from the study by Khaliq *et al.* [62] that a smaller dielectric mismatch ensured better piezoelectric properties as seen through Bowen's equation (equation (4)). Thus, KNLN-3 was preferred for our study over KNLN-6 since KNLN-6 has a higher dielectric constant and thus a larger mismatch [98]. Furthermore, shifting

towards temperatures near the PPT yields temperature instability issues which is more likely to happen in KNLN-6 which has the PPT at room temperature [90] and KNLN-6 was also seen to contain TTB phases which further decreased its performance [65].

For selecting the matrix phase, the primary constraints were the high flexibility which is needed in flexible haptic feedback applications and a high dielectric constant to reduce the dielectric mismatch with the ceramic/filler phase to the maximum extent. Based on work done on piezocomposites previously, six polymers were selected: Epoxy, polydimethylsiloxane, PVDF, PVDF-TrFE, PVDF-TrFE-CFE and polyurethane. These polymers are given alongside their respective dielectric constants and stiffnesses in Table 2.

**Table 2: Polymer phases previously used displayed alongside their Young's moduli and dielectric constants**

Polymer used	$\epsilon$ (-)	Youngs modulus (GPa)
Epoxy [99]	3.4	3.1
Polydimethylsiloxane [66]	2.7	0.006
PVDF [65]	10	2.4
PVDF-TrFE [65]	14	1.2
PVDF-TrFE-CFE [65]	55	0.4
Polyurethane [99]	3.3	0.24

From Table 2, PVDF-TrFE-CFE (CFE) terpolymer was chosen as the matrix phase due to its high dielectric constant and good flexibility (low young's modulus). Hence, for this thesis, we focus on the study of composites made with KNLN-3 in PVDF-TrFE-CFE.

## 2.7 Motivation and description of experiments

The thesis focuses on the optimization of scale-up in the KNLN-3 ceramic powders and subsequent mechanical testing. Scale-up here means the increase in the amount of KNLN-3 material prepared per batch such that it does not have any variation in physical, chemical or piezoelectric properties within the batch. In-order to scale-up the ceramic powders, one needs to optimize the powders for the specific application first so that bigger batches can be created with that specific powder. This type of powder optimization has already been done on KNLN-6 [100], but not yet done for KNLN-3, which will be the scope of this thesis. Additionally, the ultimate usage of the ceramic powders will be in the form of composites and hence, the effect of the optimization of the powders specifically with respect to microstructure, poling, composite casting method, precursors used etc., should be correlated with the properties of the composite created. Furthermore, out of the optimized powder mechanical testing must be done in-order to evaluate the performance of the composite when used in haptic feedback applications.

Based on this objective, a certain number of experiments for the optimization for scale-up and mechanical testing of the optimized powder were planned based on the time-scale available. These will be elaborated in the subsequent sections.

### 2.7.1 Agglomerate size variation and determination of poling settings

We see from the work of Deutz *et Al.* [65], that for random composites, the piezoelectric performance is dominated by the formation of agglomerates. Thus, the size of agglomerates for producing the maximum piezoelectric performance is yet to be found in our composite. Additionally, it remains to be seen whether this optimum size of agglomerates will affect the general working of the composite in-terms of the other properties considered.

Also, during scale-up of a piezoelectric material, optimum poling settings (poling time, poling temperature and poling voltages) must be established to get the maximum piezoelectric activity out of the material. It is seen from the work of Deutz *et Al.* [101], that increasing the poling temperature improved  $d_{33}$  until the melting point of the polymer was reached. Thus, a poling temperature of 110 °C (closest to melting point of CFE = 120 °C) was selected for poling of our composite. The optimum poling voltage and time remains to be investigated.

### 2.7.2 Calcination temperature variation

For scale-up, it is essential to understand how varying the calcination temperature changes the microstructure/ phase purity of the ceramic and also how these changes affect the piezoelectric properties of the composite. Based on the variation, peak performance could be dictated by a particular calcination temperature which will help in scale-up.

It is seen from previous work that a cubic morphology with particle sizes ranging from 1-3  $\mu\text{m}$  yielded the best piezoelectric properties in-terms of  $d_{33}$  for KNLN-6 ( $\text{K}_{0.47}\text{Na}_{0.47}\text{Li}_{0.06}\text{NbO}_3$ ) [100] and BT [34]. The cubic nature of the particles is naturally occurring in KNN ceramic powders and indicate the complete formation of the KNN ceramic powder but hinder the ceramic from achieving high densities due to the difficult packing. Hence, Li doping is used as described before. However, the exact calcination temperature at which this type of grain size and shape is obtained in KNLN-3 and how it influences the composite properties has not been investigated. Also, a second calcination will be done at a lower temperature for a higher dwelling time to grow sub-micrometer particles (which are essentially paraelectric [100]) produced after the first calcination into the desired cubic particles [102]. This method of introducing two calcinations in the production is known as the double calcination method. Additional to the optimization of the size and shape of grains in the double calcination method, the method also broadens the temperature range for the sintering process [103]. Also, the calcination temperatures affect the sintering of the ceramics thus, producing different sizes and numbers of agglomerates in the powders which further affect the performance of the ceramic and the composite made from it.

### 2.7.3 Dwelling time variation

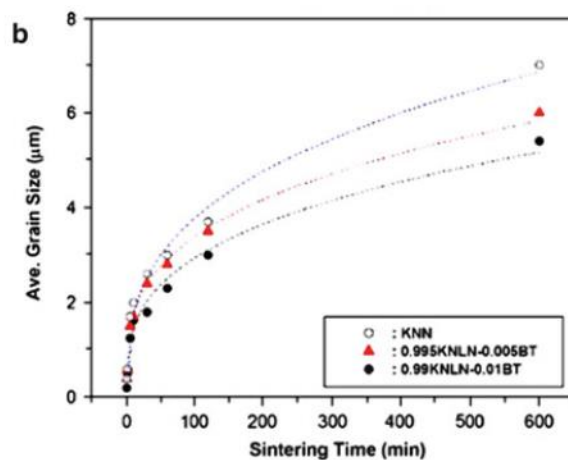


Figure 31: Average grain variation vs dwelling/sintering time in KNN ceramics [106]

Just like calcination temperature, the dwelling time also affects the grain sizes; grain shapes, agglomerate sizes and so on. As dwelling time is increased, the grain sizes continually grow as shown in [Figure 31](#). Furthermore, longer dwelling times produce more sintering leading to a better densification [104] and consequently bigger agglomerates [105]. Hence, differing dwelling times will generally affect the piezoelectric activity of the composite due to differing amounts agglomerates formed. Thus, finding the optimum grain size and agglomerate size will be the focus of this experiment.

#### 2.7.4 Ball-milling analysis

Ball-milling is a high energy process that is performed during the production of a ceramic that drastically influences its microstructure. During ball-milling, large agglomerates formed after calcination are broken as a means to control their sizes so that a usable ceramic is obtained which also in-turn affects its performance in the end. Additionally, big grains are also broken in the process due to the high energy environment producing nano-fragments. It was seen through previous work that these nano-fragments may be non-piezoelectric and could decrease the effective  $d_{33}$  [100]. Thus, during scale-up it is necessary to find the optimum amount of times ball-milling must be performed such that there is a trade-off between the  $d_{33}$  and the microstructures created. This is because too much milling may lead to many nano-fragments which may yield a low  $d_{33}$  and no milling will lead to large sized agglomerates that may not be suitable for the second calcination, as it requires smaller agglomerates for uniform grain growth [65].

#### 2.7.5 Casting method analysis

Based on previous work [107], KNLN-3 composites can be prepared via solution casting which involves dissolving the polymer in a solvent followed by mixing with the ceramic and drying. However, solvent-less casting methods would reduce time of preparation, costs, toxicity associated with the solvent if there is any and also porosities present in the sample due to solvent evaporation which ensures good poling in the composite. Hot-press method [108], [109] can be used as a solvent-less casting method to cast the composite. This involves using high pressures and temperatures to melt the polymer in the ceramic powder and form the composite solution. The solution is then cast onto a mould producing the composite sheet from which the piezoelectric properties can be tested. One disadvantage however, with the hot-press method is the mixing of the polymer and ceramic powders which is not as efficient as the mixing in the solution casting method where the solvent dispersion provides a much better mixing. Thus, the comparison of the surface topology, microstructure and  $d_{33}$  between the these two methods must be done to evaluate the ideal casting method.

#### 2.7.6 Precursor optimization

Amongst the precursors in making KNLN-3, it was seen that the niobium oxide ( $\text{Nb}_2\text{O}_5$  with 99.99 % purity) was the most expensive precursor which costed more than 2000 €/kg which is about 70 % of the entire precursor costs. Hence, an alternative niobium oxide with a lower purity (99.9 %) and consequently a much lower cost (1000 €/kg) can be used to make an alternative KNLN-3 powder. This powder can be compared with the powder made with the more pure form of  $\text{Nb}_2\text{O}_5$  in-terms of purity and the secondary phases that may be formed. Additionally, its  $d_{33}$  can also be compared with the other powder after they are made into composites to potentially replace the more pure niobium oxide with the less pure one. This would dramatically reduce costs of the precursors and aid in scale-up.

#### 2.7.7 Poling method analysis

Based on previous work [65], the KNLN-3 composites showed reproducible properties when poled via contact poling. This involves the supply of a (direct current) D.C by external means on the composite via contact through pins that also hold the composite in-place. However, with the inherent reduction of electric field flowing through the ceramic particles in a random composite due to dielectric mismatch (described in [Section-2.4.4.3](#)), a sufficiently high electric field must be supplied to the composite in-order to properly pole the ceramic inside. As high electric fields are

supplied through a small area at the tip of the pins, local breakdown of the electrode and composite may occur causing a short-circuiting in the composites that stops the poling process. This is especially the case with samples which have a lot of surface undulations as explained in [Section-2.4.2.2](#). Additionally, contact poling is influenced by many other properties like thickness, microstructure and density inside the composite. Hence, alternative non-contact poling methods such as corona poling [110] can be used to pole the composites and their properties can be compared with contact-poled composites to potentially replace contact poling with corona poling. An added benefit with using corona poling is that, it is also more scalable compared to contact poling due to the lesser human input needed.

### **2.7.8 Mechanical testing**

Based on the results from the previous experiments, an optimized powder should be obtained in-terms of its performance in a composite. Preliminary mechanical tests should be conducted on this optimized powder made into a composite to see the expected performance when it is employed in a haptic feedback device. Since haptic feedback devices rely on the sensation of touch by the user, the stiffness of the composites play a major role in the feedback since in-general a greater sensation can be felt from stiffer materials. Stiffer materials are produced by increasing the ceramic filler amount of composite but the drawback of increasing the ceramic filler is that it also leads to a brittle composite (reduction of flexibility). Thus, the exact filler volume percentage must be established that produces good piezoelectric properties (high enough filler content) whilst at the same time having a sufficient stiffness (to produce detectable feedback) and flexibility as mentioned before. Additionally, the stiffness could also be increased by adding additional amounts of stiffening materials in the composite such as glass fibres. Thus, this will give a range of values of stiffnesses based on the filler and glass fibre amounts for different samples that can provide a trade-off between a good stiffness values and other parameters relevant to the composite. For determining the stiffness, tensile and torsional testing can be done to determine the relative stiffnesses in each case.

## 3 Experimental methods

### 3.2 Production method of ceramic and composites

#### 3.2.1 Ceramic production

##### 3.2.1.1 Mixing

The first step during the ceramic production is the mixing of raw materials:  $K_2CO_3$ ,  $Na_2CO_3$ ,  $Li_2CO_3$  (stored in hot-air ovens at  $220\text{ }^{\circ}\text{C}$  to reduce moisture absorption) and  $Nb_2O_5$ . The raw materials were taken based on the stoichiometric ratios of the raw material elements in  $[K_{0.5}Na_{0.5}]_{(1-x)}Li_xNbO_3$  ( $x=0.03$  for KNLN-3 and  $0.06$  for KNLN-6 respectively). The mixture is poured into a 6.5 kg ball-mill with about 100x 5 mm diameter balls made of  $Y_2O_3/Zr_2O_3$ . The ball-mill is filled with hexane ( $C_6H_{14}$ ) until about 1 cm below the brim to prevent moisture absorption of the powder and for lubrication during milling. The mill is then fitted into a planetary ball-mill (Retsh PM 100) shown in Figure 32. The mixing is done for 12 hours at 150 RPM with 10 minute breaks every 5 minutes to prevent overheating. The long mixing time at low RPM is done to ensure complete mixing of the components instead of milling. After mixing, the contents of the ball-mill were dried on a hot-plate at  $60\text{ }^{\circ}\text{C}$  to evaporate the hexane.



Figure 32: Ball-milling apparatus

##### 3.2.1.2 First calcination

(a) Sintering oven



(b) Sintered sample after  $C_1$



Figure 33: Sintering oven (a) and sintered sample after first calcination in oven (b)

After the mixing procedure, the mixture was put in a sintering oven (L5/13 with Controller B410 manufactured by Nabertherm) shown in Figure 33 (a). A variety of calcination temperatures (800 to 1300 °C) and dwelling times (1 to 3 hours) were chosen to be performed for a study of the calcination conditions [100]. All other variables were kept constant like heating rate (5 °C/min) and cooling rate (free cooling by atmosphere inside oven). The sintered KNLN-3 after the first calcination is shown in Figure 33 (b). The specific temperatures and dwelling times taken for different samples are given in [Appendix-B2](#) and [Appendix-B3](#) respectively.

### 3.2.1.3 Milling and sieving

After the first calcination, the mixture ends up as a compacted mass in the alumina crucible. It is taken out and hand-milled using an agate mortar and pestle. The hand-milling is done to reduce the sintered ceramic into smaller particles/powder. This powder is sieved through a 125 µm mesh size sieve and any remaining material is reground until the entire powder has passed through the sieve. This is done with the help of an auto-shaker (Haver EML digital plus – Test sieve shaker manufactured by Haver and Boecker). In-order to prevent clumping from static attraction, 10-12x 1 cm diameter balls of  $Y_2O_3/Zr_2O_3$  are added when needed to break up static agglomerates. The powder after hand-milling and sieving is shown in Figure 34.



**Figure 34: Sample after hand-milling and sieving**

After the sieving procedure, the ceramic powder is placed inside the same ball-mill used for mixing as described in [Section-3.2.1.1](#). This time, balls of 3 mm diameter are added such that they cover the powder completely. The ball-mill is filled with hexane liquid up to 1 cm below the brim and fixed inside the planetary ball-mill. Then, the ball-milling is done for 1 hour at 250 RPM with no breaks. The ball-milling is done at a higher RPM with small balls for a short amount of time to ensure the agglomerates are further broken down into much smaller agglomerates without excess milling. After ball-milling the mixture is dried on a hot-plate to obtain the ceramic powder.

### 3.2.1.4 Second calcination



**Figure 35: Sample after second calcination**



After drying, the ceramic powder is put in an alumina crucible and calcined a second time. The second calcination is done at 925 °C, dwelling time of 10 hours, temperature ramp of 1 °C/min, and free cooled in the oven for all samples. The sample comes out as a partially sintered powder as shown in Figure 35, as the second calcination is mostly done for grain growth and formation of agglomerates.

### 3.2.1.5 Second milling and sieving

Just like the first calcination, after the second calcination hand-milling is done to reduce the bulk mass that is got from the second calcination to workable powders. Then, again the mixture is sieved with the help of an auto-shaker over a 125 µm followed by a 63 µm sieve. These settings were optimized based on the thickness of the composite that is formed afterwards (100 µm to 200 µm) as described from previous work [65]. For comparing different agglomerate sizes, the powder left in-between each of the sieves was taken for composite preparation. The sieves taken were of mesh sizes: 125 µm; 90 µm; 63 µm and 25 µm respectively. The specific sieves in-terms of the mesh size used for each sample of each analysis is given in [Appendix-B](#).

## 3.2.2 Composite production

Composites were made by combining the ceramic powder produced and casting with the CFE polymer. Two methods of composite casting were tested. The description of the procedure for both, will be given in subsequent sections.

### 3.2.2.1 Solution-casting

#### 3.2.2.1.1 CFE/DMF polymer solution preparation

A 13 wt% solution of CFE in dimethylformamide (DMF) was prepared by adding the required mass of CFE to DMF and stirring until dissolved. Before usage, the solution was degassed under vacuum for 1 hour to remove the air bubbles.

#### 3.2.2.1.2 Mixing of polymer and ceramic

In all samples, except for mechanical testing, ceramic powder was mixed with CFE solution such that a final 50:50 volume composition of ceramic:CFE (so called R50 composites; random, 50 V% filler) would be obtained after drying, calculated based on a 13 wt% solution of CFE in DMF. The relative amounts of CFE solution and ceramic powder were mixed in a speed mixer (Speedmixer DAC150.1 FVZ) at 750 RPM for 5 minutes. The liquid was then degassed in a vacuum pot until no more bubbles were observed. For larger agglomerate sizes, the mixing was done at 2500 RPM for 15 minutes to ensure proper mixing. For mechanical testing, as a means for changing the stiffness of the samples, the ceramic amount was changed and also 2% wt. of CFE was added as glass fibres. These are described in [Appendix-B](#). For the samples with glass fibres, the mixing was done at 2500 RPM for 15 minutes to ensure the glass fibres dissolved.

#### 3.2.2.1.3 Casting

The composites were prepared by solution casting onto a glass plate, that has been coated with release agent, using the doctor blade technique with a cast height of 1 mm. A schematic representation of this process is shown in Figure 36.

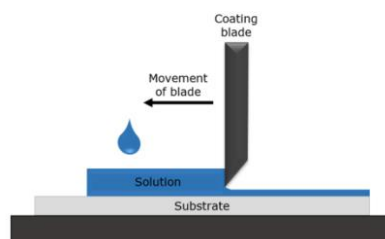


Figure 36: Composite solution after solution casting



The cast speed was kept at 5 mm/s. For some of the mechanical testing samples the cast height was varied based on the CFE amount in the composite. These are given in [Appendix-B6](#). Additionally, the cast speed was kept at 2.5 mm/s to reduce the bubbles formed under low ceramic filler loadings.

#### **3.2.2.1.4 Drying and annealing**

The solution cast composites were dried in a vacuum oven (Thermoscientific VACUTHERM-4109 vacuum oven) at 70 °C under active vacuum. After the DMF is evaporated, the samples were kept in a conventional oven at 110 °C for 1 hour for annealing. The sample after drying and annealing is shown Figure 37. The annealing ensured stresses that form in the composite after DMF evaporation are released. The composites generally had a rough side (that faced away from the glass plate from which the DMF evaporates) and a smooth side (that was placed on the glass plate).



**Figure 37: Composite sample after drying and annealing**

#### **3.2.2.2 Extrusion and hot-pressing**

Composites were also prepared via hot-pressing as a means to make the composite casting method solvent-less. The hot-pressing was carried out at the Sabic plant located in Bergen-Op-Zoom, the Netherlands with the help of a hot pressing attachment to a standard pneumatic press at 250 °C and 2 bars of pressure for 1 minute. R40 composites (40 vol. % KNLN-3 and 60 vol. % CFE) were initially prepared using a micro-compounding twin screw extruder from Xplore shown in Figure 38 to hot mix and extrude strands of the R40 composite (mixing at 5 RPM for 2 minutes at 250 °C).



**Figure 38: Micro-compounding twin screw extruder**

R40 composites was prepared instead of the usual R50 composites because the R50 composites were too viscous for the extrusion apparatus. A composite sheet was obtained after hot-pressing pellets (cut from the extruded strands) in the described setup from which the conventional composite discs can be cut.

### 3.2.3 Poling the composite

Poling is the process by which a ceramic or composite which initially has randomly oriented domains are oriented in a specific direction by supplying an electric field along the poling axis. This is described in detail in [Section-2.4.2.2](#). Two poling methods were done to investigate the effects that these methods have on the general working of the composite. These are described in subsequent sections.

#### 3.2.3.1 Contact poling

##### 3.2.3.1.1 Electrode formation

After the composite is annealed, 12 mm diameter discs are cut from the composite. The discs are then sputtered with gold electrodes with the help of a magnetron sputterer (Balzers Union SCD-040 Magnetron Sputterer) as shown in Figure 39 (a).

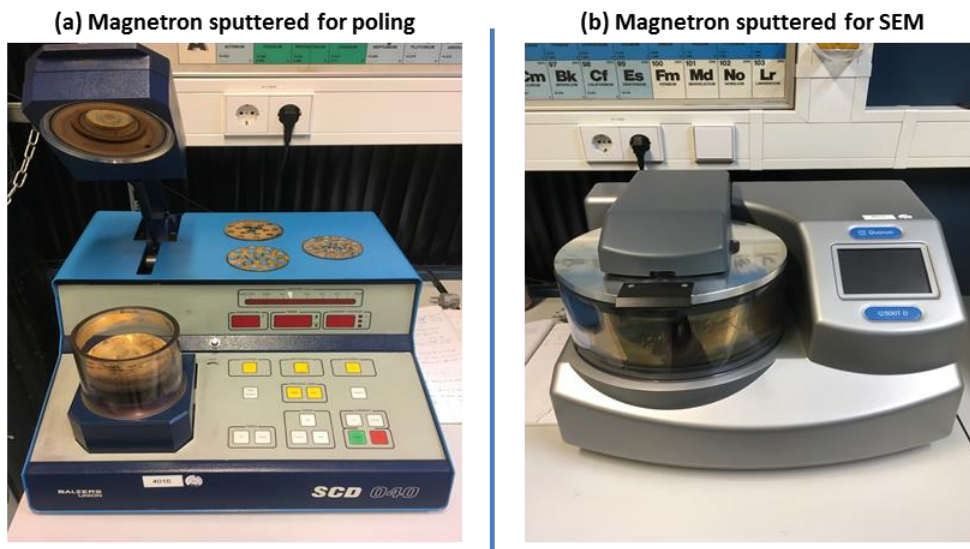


Figure 39: Magnetron sputterers for poling (a) and SEM (b)

In this, argon plasma is created by supplying a sufficient voltage, which strike the gold target present on the top of the set-up. The impact creates gold ions, which are sputtered down onto the sample placed below which forms the electrodes. The samples before and after gold sputtering is shown in [Figure 40 \(left\)](#) and [Figure 40 \(right\)](#) respectively.

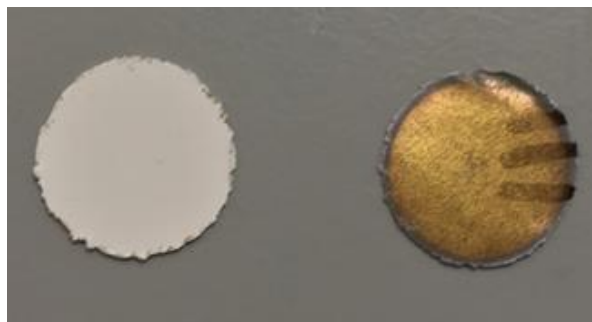
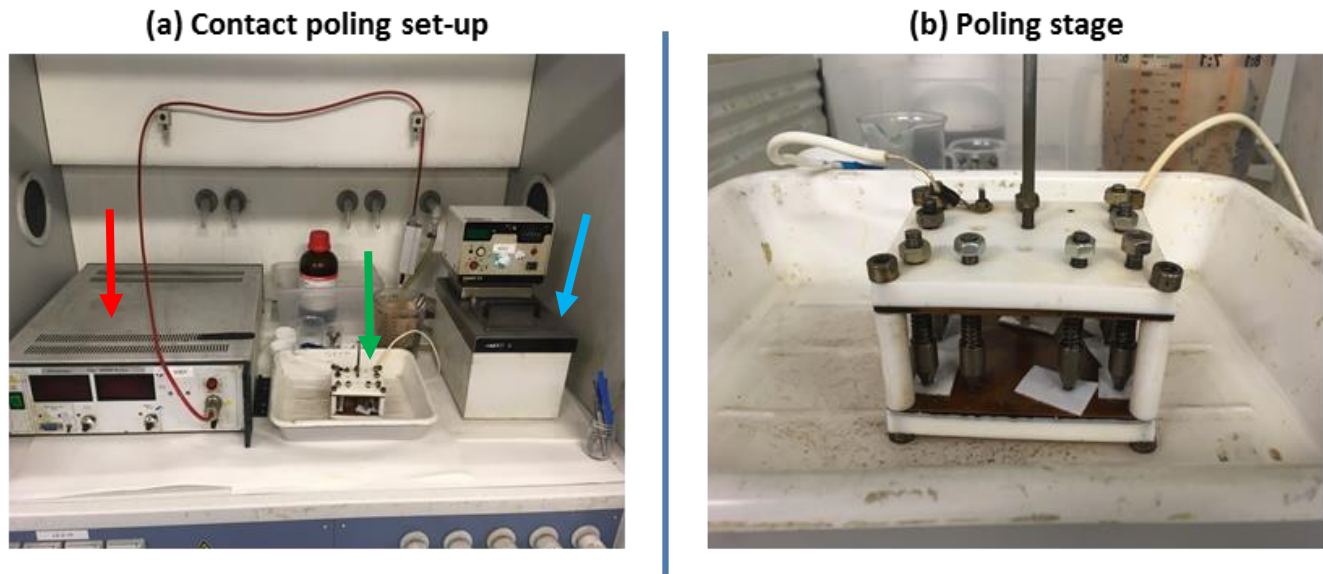


Figure 40: Sample before (left) and after (right) gold sputtering

The process is done under active vacuum. The sputtering is done at 18 mA for 8 minutes on both sides. The sputtering is done on 10 mm diameter areas on the composite discs with the help of a stencil. This is to prevent touching of the electrodes from either side of the composite disc.

Additionally, before SEM (scanning electron microscopy) is performed on the samples which will be described in [Section-3.2.5.2](#), the samples must be sputtered with gold electrodes just like in poling scenarios. This is to ensure electrons pass through the sample for visualization. Another magnetron sputterer was used for this (Quorum Q300T D – Magnetron sputterer) which is shown in [Figure 39 \(b\)](#). Before poling, the discs with the electrodes are kept in vacuum for 1 day to make sure the adsorbed moisture is removed.

### 3.2.3.1.2 Poling



**Figure 41: Poling set-up (a) with amplifier (red arrow), poling stage (green arrow) and poling bath (blue arrow) and poling stage (b)**

In contact poling the composite is given a high DC voltage via contact with pins. Before poling, the composite discs were measured for their thickness and weight. The thickness was measured to calculate the amount of voltage needed to supply each disc with a particular specific voltage. The weight was measured to calculate the density of the samples. Contact poling was done at the DASML lab with the help of a poling set-up shown in [Figure 41 \(a\)](#). The poling was done at 110 °C in a silicone oil bath (indicated by blue arrow). Voltage supply was provided using an amplifier (indicated by red arrow). The discs were fitted on a stage shown in [Figure 41 \(a\)](#) (indicated by green arrow) and [Figure 41 \(b\)](#) with the help of pins which supplied the voltage to the discs from the amplifier. The poling time and voltage were varied between samples and are described for each experiment in [Appendix-B](#). The smooth side of the composite was in contact with the pin as this gave better poling (better  $d_{33}$  and lesser short-circuiting). After poling, the composites were dried with tissue paper that removed the silicone oil. They were then ready for analysis.

### 3.2.3.2 Corona poling

A corona poling unit was used to pole the composites using a corona discharge rather than a direct DC voltage applied on a sputtered sample like in contact poling described in [Section-3.2.3.1](#). The composite samples were cut into rectangular pieces of 20 mm X 20 mm dimensions and placed inside the corona poling unit. The electrical field on the sample was stabilized using a comparison circuit to a voltage of 10 kV/mm to compare with the results of the contact poling. The corona poling was done for 30 minutes.  $d_{33}$  obtained from corona poling done at different points on the composite were averaged to find the  $d_{33}$  of the entire composite. The corona poling was done at SABIC

technology centre in Bangaluru, India. The exact description of the samples for which corona poling was done is described in [Appendix-B8](#). The corona poling unit is shown in [Figure 42](#).



**Figure 42: Corona poling unit**

### 3.2.4 Storage

All samples (composite and ceramic powder) were stored under vacuum in a dessicator. This was done to prevent any moisture absorption. Additionally, before analysis all poled composite discs were stored in vacuum for 2 days to stabilize the  $d_{33}$ .

### 3.2.5 Analytical methods

#### 3.2.5.1 XRD

XRD (X-ray powder diffraction) was used to characterize the phase distribution and unit cell parameters of the ceramics. In XRD, X-rays of a specific wavelength are fired at the sample placed in different angles. Collectors are used to analyze the X-rays diffracted out of the sample to analyze the structure of its crystal lattice. This was performed after each calcination. XRD was done to potentially see any differences in phase purity, alkali evaporation, sample stoichiometry imbalances and crystallinity between samples. Generally, crystallinity is indicated by the width and sharpness of peaks and the others are indicated by a change in the position of the peaks. XRD analysis was performed from 10-60 ° using  $\theta$ -2 $\theta$ , Bragg-Brentano geometry and Cu- $K_{\alpha}$  radiation ( $K_{\alpha-1}=1.54059 \text{ \AA}$ ,  $K_{\alpha-2}=1.54431 \text{ \AA}$ ) with a Rigaku XRD-Miniflex 600, shown in [Figure 43](#).



**Figure 43: XRD apparatus**

### 3.2.5.2 SEM

SEM was used to visualize the microstructures of the ceramic powder and composite samples. The scanning electron microscope used was JEOL JSM-7500F – Field emission scanning electron microscope which is shown in Figure 44. In SEM, highly focused beams of electrons are shone on a sample. The electron interaction with the sample produces various secondary emissions. The secondary electrons emitted from the conduction bands of the specimen can be analysed to get information on the topography of the sample. The essential principle behind its operation is the same as an optical microscope albeit with a higher magnification owing to the lower wavelength of electrons (1.23 nm) compared to visible light (500 nm for blue light).



Figure 44: SEM

Hand-milling and sieving processes are done before SEM so that a clean powder is obtained which is easy for sample preparation whilst at the same time keeping the agglomerates intact. The SEM was done from 50x to a maximum of 10000x magnification based on visibility of the topography in the samples. Composite cross-sections were also visualized in SEM by breaking the composite with liquid nitrogen to ensure brittle fracture. Additionally, both composite surfaces (rough and smooth) were also analysed.

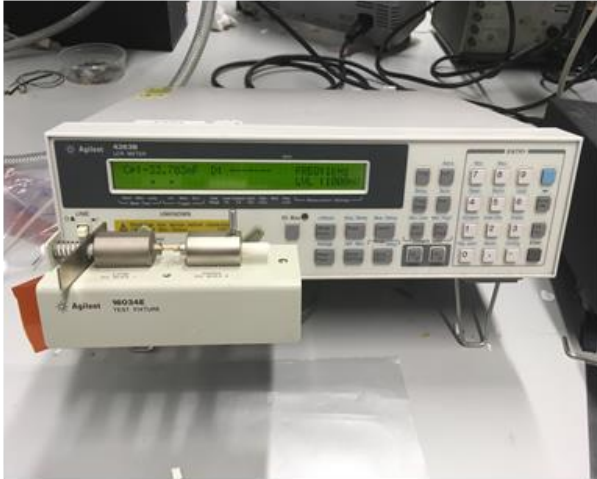
### 3.2.5.3 LCR meter and Berlin-court meter

An Agilent 4263B LCR (inductance, capacitance, resistance) meter was used to measure the capacitance and  $\tan(\delta)$  of the composites before and after poling with a frequency 1 kHz and voltage of 1 V. The instrument is shown in Figure 45 (a). The capacitance is used to calculate the dielectric constant of the material and the  $\tan(\delta)$  is used to quantify the dielectric losses in the composite, which could affect poling. The  $\tan(\delta)$  is highly sensitive to the absorption of moisture by KNLN ceramics and hence, serves as an indicator of the moisture absorbed.

A Berlincourt-type piezometer, from Piezometer Systems, as shown in Figure 45 (b) was used to measure the  $d_{33}$  of the composites after poling. It consists of a vibrating pin with a specific amplitude and frequency that supplies electrical signals from the poled composite to the machine. The  $d_{33}$  is calculated with respect to a reference. A static force of 1 N, dynamic force of 0.25 N and a frequency of 110 Hz was used during the measurement of  $d_{33}$ .



(a) LCR meter



(b) Berlincourt meter

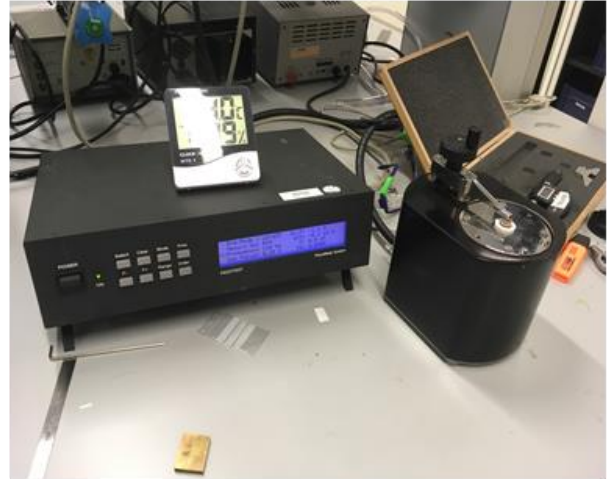


Figure 45: LCR meter (a) and Berlincourt meter (b)

#### 3.2.5.4 Particle size distribution

A particle size analyzer (Mastersizer Hydro 3000) shown in Figure 46, manufactured by Malvern, was used to analyse the particle size distributions of a variety of samples.



Figure 46: Particle size analyzer

This was used to get a more reliable estimate of the grain and agglomerate sizes present in the ceramic powders. In the particle size analyzer, a small amount of sample is taken and dropped through a laser. Based on the intensity of the diffracted laser beams, picked up by a collector, the particle sizes are determined based on the number of particles present per size. The particle size analysis was done with water as the solvent at 2480 RPM after mixing with an ultrasonic probe for 5 minutes at 6.5 kHz with 20 second intervals every 10 seconds of ultrasonication. The obscuration intensity was kept at  $\approx 6\text{--}7\%$  for all samples. The exact description of the samples for which particle size distribution was determined is described in [Appendix-B7](#).

#### 3.2.5.5 Confocal microscope

A confocal microscope (Olympus LEXT – TS150 confocal microscope) as shown in [Figure 47](#), was used to measure the surface roughness and waviness of the composite samples. The surface roughness and waviness parameters were estimated as the line roughness and waviness averaged out along six lines (three vertical and three horizontal lines with equal spacing between them) drawn on the focused image of the sample.

These were done to verify whether these parameters interfere with the extent of poling and subsequently the performance. In a confocal microscope, a laser is used to scan a specified area prescribed by the magnification over multiple focal lengths. The inbuilt machine analyses these images and generates the local surface topologies. All samples were measured for surface roughness and waviness only on the rough side (side that faces away from the glass during evaporation of DMF) as these were influential during the poling. A cut-off wavelength ( $\lambda_c$ ) of 0.1 was used to distinguish between roughness and waviness. The entire procedure was performed at 20x magnification. Additionally, the profiles of each sample were treated with a filter that removed noise.

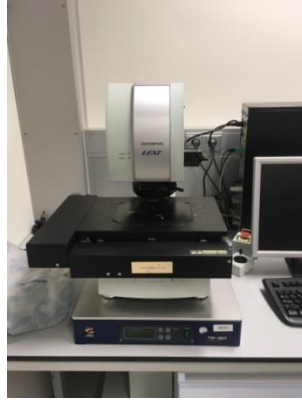


**Figure 47: Confocal microscope**

### 3.2.5.6 DSC

DSC (differential scanning calorimetry) was used to examine the position of the PPT and  $T_c$  for each of the samples in the calcination temperature and dwelling time variation studies as seen in previous work for BT [111]. This is to check the samples for alkali evaporation that cannot be detected by XRD due to their small sizes like in the case of lithium. As the PPT and  $T_c$  are highly sensitive to the amount of lithium present in KNLN ceramic as shown by the work of Li *et al.* [90] in Figure 28, we can analyze the potential amount of lithium lost by evaporation by detecting the temperature at which the PPT and  $T_c$  peaks are observed in DSC. The PPT and  $T_c$  peaks were assessed based on the heating curve for all samples.

In DSC, the heat flow present in the sample is measured over a wide range of temperatures with respect to a reference sample. Thus, all temperature transitions which are present in the sample within the chosen temperatures is seen as a change in heat flow (peak or trough). DSC was performed from 25 °C to 450 °C for all samples with a heating and cooling rate of 10 °C/min and a dwelling time of 5 minutes at the extreme temperatures. The DSC used was a Discovery TA DSC-250, shown in Figure 48.

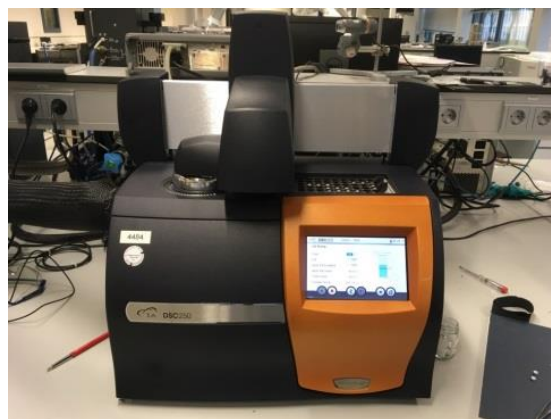


**Figure 48: DSC apparatus**

### 3.2.5.7 DMA

DMA (dynamic mechanical analysis) was used to perform tensile testing on the samples. The DMA apparatus used was Discovery TA G2-RSA as shown in Figure 49. The samples were manually cut into rectangular pieces with dimensions: 30 mm X 10 mm and fit into the DMA clamps. The entire test was performed at room temperature with no change in frequency of loading. The loading was done in a strain controlled fashion with strain rate of 0.03 mm/sec. The load cell had a maximum loading capacity of 35 N. The samples used for tensile testing in the DMA apparatus are described in [Appendix-B6](#).

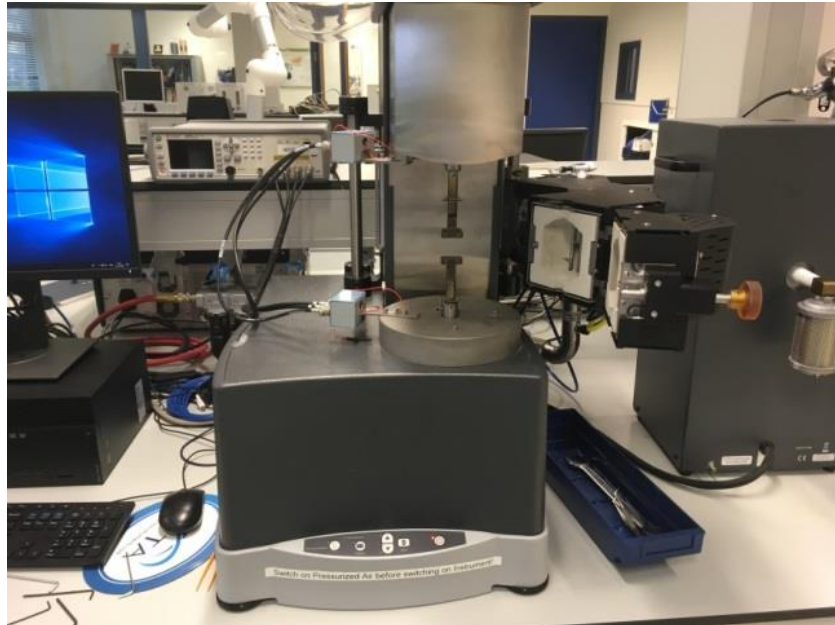


Figure 49: DMA apparatus

### 3.2.5.8 Rheometer

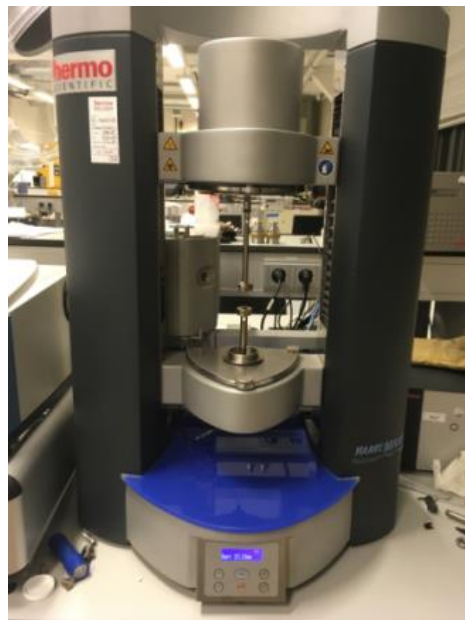


Figure 50: Rheometer

A rheometer was used to test the samples for the the normal force produced during torsion. The samples were manually cut into rectangular pieces with dimensions of about: 30 mm X 10 mm and clamped inside the torsion



tester. The entire test was performed at room temperature. A dynamic load was applied on all samples. The test was performed in a rotation controlled fashion with a constant rotation of  $5 \times 10^{-4}$  rotations per second. The frequency was kept at 0.5 Hz. The test was performed for 300 seconds for all samples. The rheometer apparatus was called: Haake Mars Modular Advanced Rheometer system. The apparatus is shown in [Figure 50](#). The samples used used for torsion testing in the rheometer are described in [Appendix-B6](#).

## 4 Results and discussion

### 4.1 Study of poling conditions, agglomerate size and Li content

In this study, two types of composites: KNLN-6/CFE and KNLN-3/CFE composites were taken under different agglomeration sizes ( $<63\ \mu\text{m}$  and  $63\text{--}125\ \mu\text{m}$ ) and poled under different conditions. The samples were prepared based on previous work [65] and are described in [Appendix-B1](#). The poling time was varied between 10 and 20 minutes and the poling voltage from 5 kV/mm to 10 kV/mm. Beyond 10 kV/mm, all the samples short-circuited and below 5 kV/mm none of the samples were poled. All samples short-circuited when the poling was done at 10 kV/mm for 20 minutes and none of them were poled when poled at 5 kV/mm for 10 minutes. Additionally, the higher sized agglomerated samples could not be poled past 5 kV/mm as all of them short-circuited. This was most likely due to inhomogeneous field distribution from the erratic surface topology. The results of the  $d_{33}$  vs the samples for the poling voltage study is shown in [Figure 51](#). The legend indicates the mesh sizes in the sieves. Only the samples which had poled successfully (had a definite  $d_{33}$ ) without many short-circuits are shown.

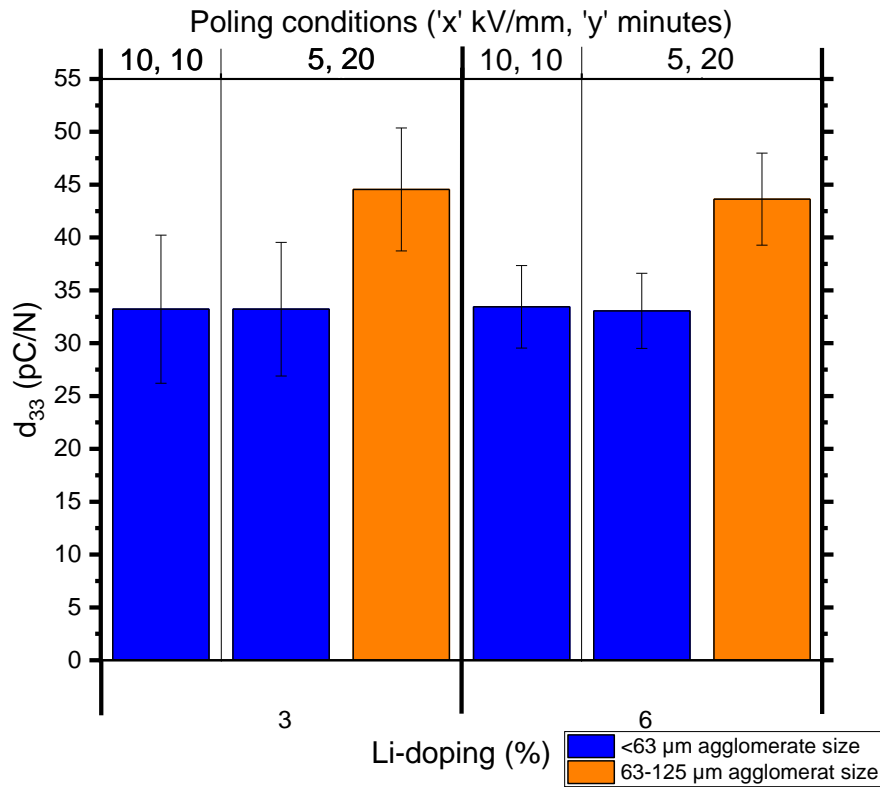


Figure 51:  $d_{33}$  of the samples with different agglomerate sizes and Li doping

#### 4.1.1 Poling settings variation

From Figure 51, it is seen that for the lower sized agglomerate samples, poling at higher voltages for shorter times produced identical performance compared to the same samples poled at lower voltages for longer times. This suggests that longer poling times does affect the extent of poling and consequently the performance. As stated before, it was also seen from the experiment that higher poling times and voltages ( $>20$  minutes and  $>10$  kV/mm) caused short-circuits and lower poling times and voltages ( $<10$  minutes and  $<5$  kV/mm), did not pole the samples.

This suggests that with KNLN/CFE composites there is an upper limit to the poling time and voltage after which sample electrodes degrade and there is a lower limit to poling time and voltage which is designated to the coercive field associated with KNLN. For subsequent experiments, 10 kV/mm for 10 minutes is taken as the poling setting.

#### 4.1.2 Comparison of performance

From the results, it can be seen that higher sized agglomerate samples perform better than lower sized agglomerate samples. This is attributed to the pseudo 1-3 composite effect exhibited by these composites in which the greater connectivity present in 1-3 composites is mimicked. Hence, larger agglomerates can be said to provide lesser interparticle distance that is similar to the chain-like structures formed by the ceramic particles in DEP structured composites [65] which lead to a better poling and consequently a higher  $d_{33}$ . Thus, we see that the behaviour of random composites is dominated by the size of the agglomerates present. The mimicking of the 1-3 composite is also clearly seen in the higher sized agglomerated samples as opposed to the lower sized agglomerate samples viewed through SEM as shown in Figure 52 (a) and Figure 52 (b) respectively. Additionally, the variation of  $d_{33}$  between each set of samples is the same which suggests that the variation in the size of agglomerates (from 63-125  $\mu\text{m}$  to <63  $\mu\text{m}$ ) between samples does not influence the variation in the performance.

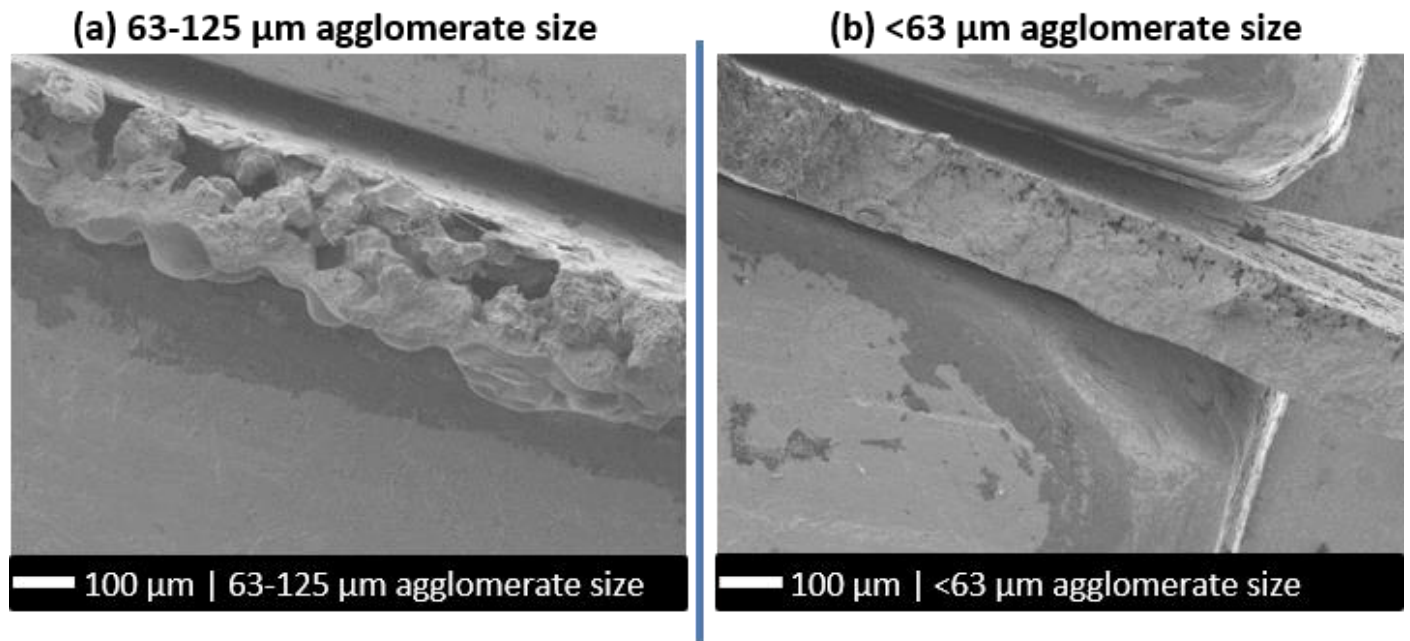


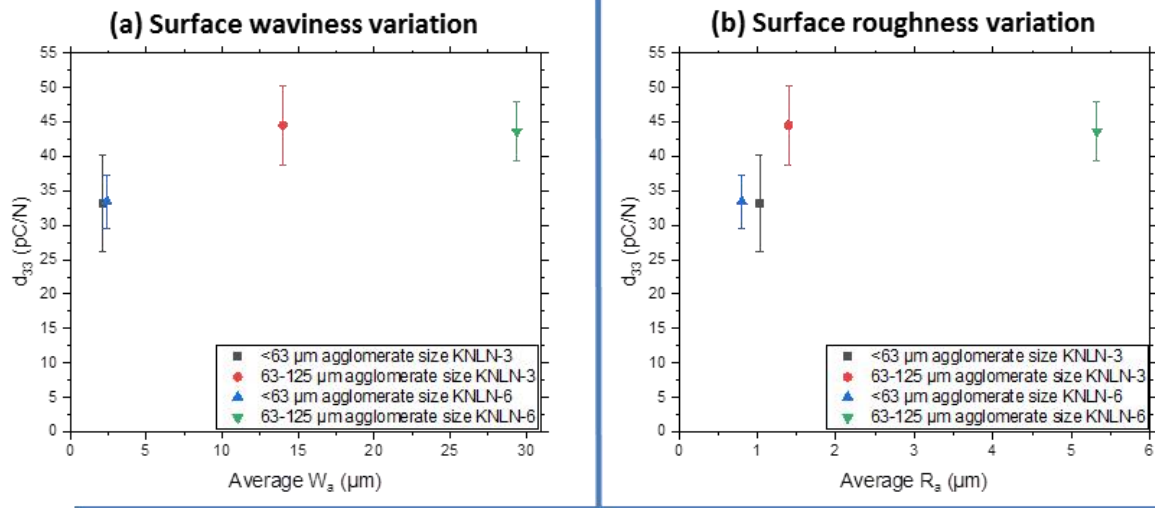
Figure 52: SEM image (100x magnification) of KNLN-6 piezocomposite cross-sections with 63-125  $\mu\text{m}$  agglomerate size (a) and <63  $\mu\text{m}$  agglomerate size (b)

#### 4.1.3 KNLN-6 vs KNLN-3

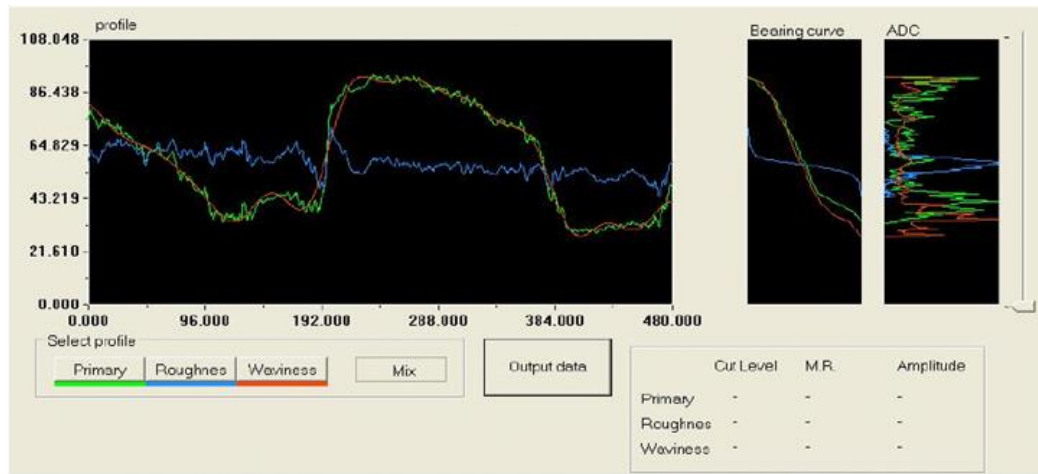
It can also be seen from Figure 51, that the KNLN-6 samples perform to the same extent compared to KNLN-3 samples under equal agglomerate sizes. This shows that, in a random composite, KNLN-6 samples perform equally to KNLN-3 samples (even at high filler loadings), even though in their ceramic counterparts, KNLN-6 performs better compared to KNLN-3. This is likely due to the higher dielectric mismatch between KNLN-6 and the matrix, compensating for any increase in  $d_{33}$ .

#### 4.1.4 Surface roughness and waviness

The line waviness ( $W_a$ ) and roughness ( $R_a$ ) of the samples discussed above was measured with a confocal microscope and is quantitatively plotted against their  $d_{33}$  in Figure 53 (a) and Figure 53 (b) respectively.



**(c) Profile variation of 63-125  $\mu\text{m}$  agglomerate size KNLN-6**



**(d) Composite discs made with 63-125  $\mu\text{m}$  (left) and <63  $\mu\text{m}$  (right) agglomerate sizes**

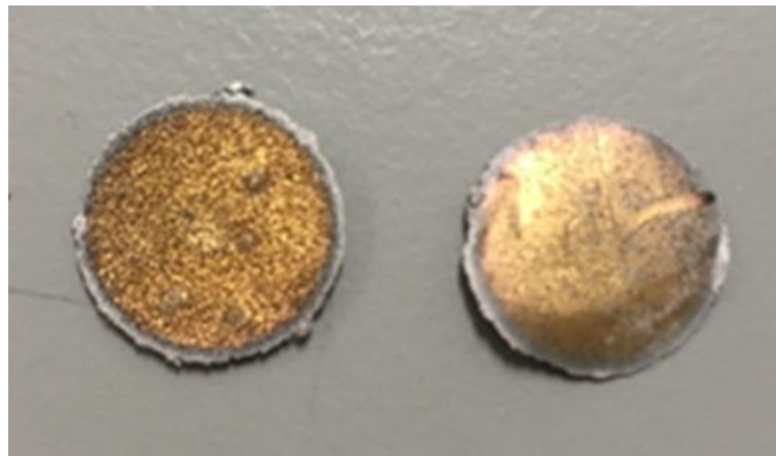


**Figure 53:  $d_{33}$  vs (a) average  $W_a$  and (b)  $R_a$  for the samples in the poling study; (c) primary (green), roughness (blue), waviness (red) profiles of higher sized agglomerate KNLN-6 sample and (d) composite discs made with 63-125  $\mu\text{m}$  (left) and <63  $\mu\text{m}$  agglomerate sizes**

The  $W_a$  and  $R_a$  were averaged out along six lines in the microscopic image to obtain the surface waviness (average  $W_a$ ) and surface roughness (average  $R_a$ ). The waviness corresponds to large undulations that coincides with the

surface profile while the roughness corresponds to small-scale surface irregularities. From the results in Figure 53, we can quantitatively see that the higher sized agglomerated samples had more waviness ( $\approx 30 \mu\text{m}$ ) compared to the lower sized ones ( $\approx 2 \mu\text{m}$ ). However, the roughness of the samples were almost the same amongst all the samples (between 1 to 5  $\mu\text{m}$ ). Hence, waviness can be regarded as the primary measure of the undulations on the surface of the samples. This is further confirmed with the help of the profile images of the higher sized agglomerate KNLN-6 sample seen in Figure 53 (c), where we can see that the waviness more corresponds to the undulations of the primary profile compared to the roughness.

It is also seen from the results that the higher agglomerate sized KNLN-6 had more waviness compared to its KNLN-3 counterpart. This could be because of a higher amount of lithium doping in KNLN-6 (which aids densification) combined with a higher dwelling time (3 hours as opposed to 1 hour for KNLN-3), which effectively increased the agglomerate sizes and numbers. However as mentioned, the  $d_{33}$  of both the composites is seen to be almost equal, showing that this increased waviness has little impact on the  $d_{33}$  and instead was seen to produce more short-circuited samples due to local change in electric field. The high surface waviness is visibly seen for the higher sized agglomerate sample compared to the lower one in Figure 53 (d).

## 4.2 Calcination study

### 4.2.1 First calcination temperature variation

From the previous section, it was established that  $<63 \mu\text{m}$  agglomerate sizes provided ideal poling scenarios. Thus, different KNLN-3 samples were made with that agglomerate size under first calcinations ( $C_1$ ) temperatures of: 750 °C, 850 °C, 900 °C, 950 °C, 1000 °C, 1050 °C, 1100 °C, and 1150 °C (ramp rate kept at 5 °C/minute for all samples) and a dwelling time of 1 hour respectively. The second calcination ( $C_2$ ) for all samples were done at 925 °C for 10 hours with 1 °C/minute ramp rate. Only the effect of varying the  $C_1$  settings was investigated due to time constraints. The specifics of sample preparation are given in Appendix-B2.

#### 4.2.1.1 Comparison of performance

The results of  $d_{33}$  vs the  $C_1$  temperatures of samples analyzed is shown in Figure 54 along with the variations in the  $d_{33}$ .

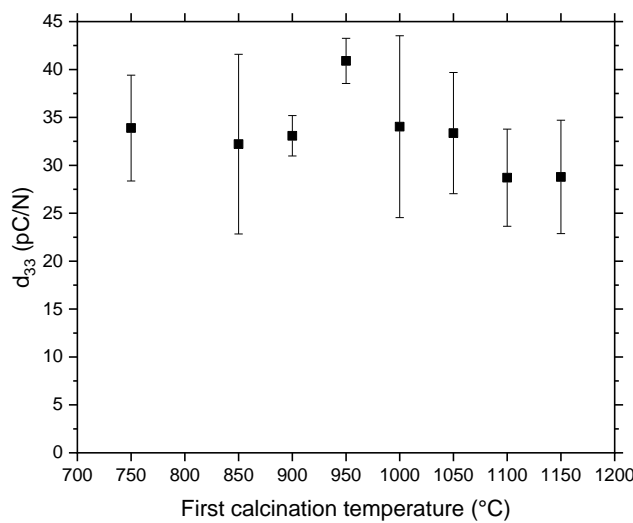


Figure 54:  $d_{33}$  vs  $C_1$  temperatures of samples with  $C_1$  dwelling time of 1 hour

From the results, we see that the value of  $d_{33}$  is highest for the sample with  $C_1=950$  °C-1 h. Further below this  $C_1$  temperature, the  $d_{33}$  decreased initially and then seems to remain mostly constant while above it there is a decreasing trend with increasing temperature.

## 4.2.2 First calcination dwelling time variation

An investigation into the influence of the  $C_1$  dwelling time on the properties of the composite was also carried out as part of the scale-up procedure. From the calcination temperature study, it was seen that the highest  $d_{33}$  was observed in the sample with  $C_1 = 950$  °C-1 h. Additionally, previous work on KNLN-3 was done with a  $C_1$  temperature of 1050 °C [65], [66]. Hence, for the investigation on the effect of dwelling time, these two  $C_1$  temperatures were considered along with an intermediate  $C_1$  temperature of 1000 °C. The  $C_1$  dwelling time was varied between 1 hour and 3 hours for these selected  $C_1$  temperatures. The  $C_2$  was done with the same settings as in [Section-4.2.1](#). The specific calcination route and the materials taken for the production are given in [Appendix B3](#).

### 4.2.2.1 Comparison of performance

The results of the  $d_{33}$  against the  $C_1$  temperature for each of the  $C_1$  dwelling time variation samples is given in Figure 55. It can be seen from the results that the samples with 3 hour  $C_1$  dwelling times had a slightly higher  $d_{33}$  ( $\Delta d_{33} \approx 4$  pC/N which is  $\approx 10$  % more) compared to their 1 hour counterparts for all samples.

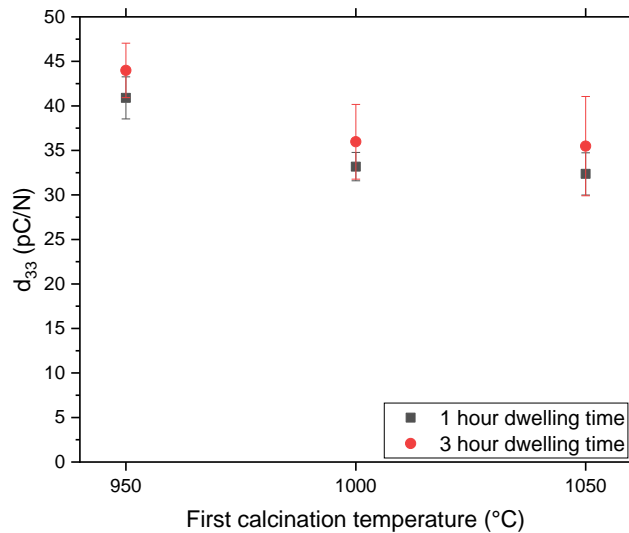


**Figure 55:  $d_{33}$  vs  $C_1$  temperature of the samples for  $C_1$  dwelling times of 1 hour and 3 hours**

The exact reasoning behind this distribution in the two calcination studies could be due to the influence of grain sizes [34] or agglomerate sizes in each of the samples, as explained in [Section-4.1](#). This is because there is an increase in the sintering and grain growth associated with a higher calcination temperatures and dwelling times [100]. In-terms of grain sizes, there seems to be an optimal grain size where the highest  $d_{33}$  is obtained for the ceramic powder as seen in the work of Huan *et al.* [34]. The additional sintering is directly advantageous to the  $d_{33}$  as seen in [Section-4.1](#), since a higher  $d_{33}$  was noticed with an increase in the agglomerate sizes. Hence, an investigation into the microstructure of the samples was done which is discussed in [Section-4.3](#) and [Section-4.4](#). Since very big agglomerates also influenced the surface waviness and consequently the amount of short-circuiting, it was also investigated for all the samples in [Section-4.2.4](#). It was also seen from previous work [100], that at higher calcination temperatures and dwelling times, the evaporation of the precursors occurred for KNLN ceramics. Additionally, it was

seen by Deutz *et Al.* [65] and James *et Al.* [100], that these samples contained crystalline defects and nano-fragments in the powders which could also influence the  $d_{33}$ . These were investigated in [Section-4.2.3](#).

### 4.2.3 Phase purity

Before the comparison of performance, the phase purity of the samples at different  $C_1$  temperatures and dwelling times was investigated by XRD and DSC. In KNLN ceramics the phase purity is affected mainly by the defects created in the crystal lattice owing to alkali evaporation at high calcination temperatures. The alkali evaporation also induces formation of minor secondary phases by a combined effect of alkali evaporation and segregation. These secondary phases have a non-perovskite TTB structure which lowers the polarisable volume in the powder, further reducing the performance [65]. The typical secondary phase observed in KNLN-3 is indexed as:  $K_6Nb_{10.8}O_{30}$ . The phase purity could also be influenced by other phenomena like presence of nano-fragments or oxygen vacancies which is usually seen as peak broadening in the XRD peaks. The XRD and DSC were performed after each calcination and sieving processes in order to obtain a usable powder fit for the analysis.

#### 4.2.3.1 First calcination temperature variation

The XRD results of the  $C_1$  temperature variation samples are shown in Figure 56 after  $C_1$  and  $C_2$  with miller indices labelled for each peak based on previous work [112]. After  $C_1$ , there is a shoulder (indicated by solid black arrow) in the (111) peak for the  $C_1 = 750^\circ\text{C}$ -1 h sample. This is attributed to incomplete calcination, arising from the low  $C_1$  temperature of the sample. However, this shoulder disappears after  $C_2$  for the same sample (indicated by dotted black arrow) indicating complete reaction after  $C_2$  and no precursors being present beyond this point. No secondary phases are formed in all the samples as indicated by the absence of peaks in the region between  $25^\circ$  to  $30^\circ$ .

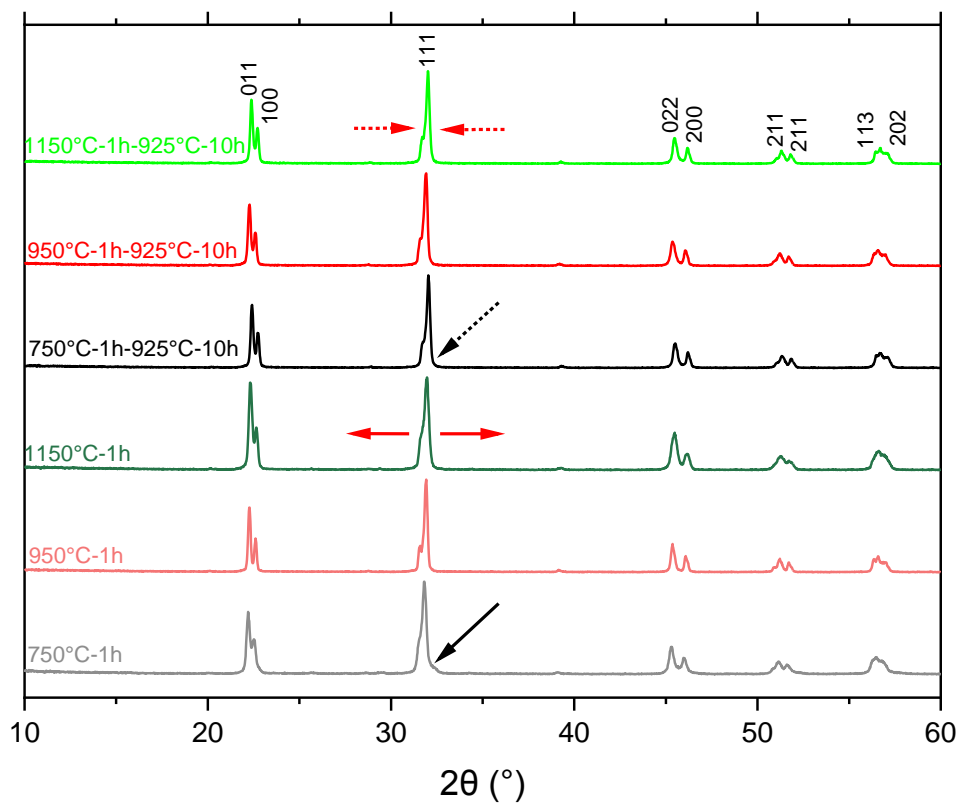


Figure 56: XRD results shown for samples with  $C_1 = 750^\circ\text{C}$ -1 h,  $950^\circ\text{C}$ -1 h,  $1050^\circ\text{C}$ -1 h, and  $1150^\circ\text{C}$ -1 h after  $C_1$  and  $C_2$  ( $925^\circ\text{C}$ -10 h)



On the contrary in samples made with higher  $C_1$  temperature like the  $C_1 = 1150\text{ }^{\circ}\text{C-1 h}$  sample, there is a peak broadening (indicated by solid red arrows) in the (111) peak after  $C_1$  which is usually associated with crystal lattice distortions induced by alkali evaporation in KNLN-3 due to the high temperatures. This could potentially change the Li-doping level in the ceramic as lithium is usually the first to evaporate from KNLN ceramics due to its smaller atomic size [90].

For the same sample, it is seen that after  $C_2$  (indicated by dotted red arrows), that the peak broadening is absent suggesting that there was no alkali evaporation initially. However, it could be attributed to alkali evaporation specific to lithium evaporation which may not be detected by the XRD machine. This is because of the small amount of lithium present in KNLN-3 and its small atomic size. The peak broadening could also be attributed to oxygen vacancies [113] that are present after  $C_1$ , getting filled during the lower temperature treatment of  $C_2$  or the formation of nano-fragments that are formed after sieving that regrow to conventional grains during  $C_2$  which makes the peak broadening disappear. Another reason for the peak broadening could be due to a small amount of sodium and potassium evaporation on the surface of the powder during  $C_1$ . The absence of the peak after  $C_2$  could be due to the homogenization of the defects created by the evaporation over the entire bulk of the powder during  $C_2$ . While the lithium evaporation and presence, effect of nano-fragments are investigated in subsequent sections, the latter phenomena could not be checked due to lack of time.

DSC was specifically done to probe the value of Curie temperature ( $T_C$ ) and onset temperature of PPT ( $T_{O-T}$ ) since these temperatures are sensitive to the lithium content present in the powders. Thus, they provide a means to check the lithium evaporation in the powders. The DSC results of the  $C_1$  temperature variation samples are shown in Figure 57 (a) and Figure 57 (b) after  $C_1$  and after  $C_2$  respectively, as the  $T_{O-T}$  and  $T_C$  temperatures vs calcination scenarios for each sample.

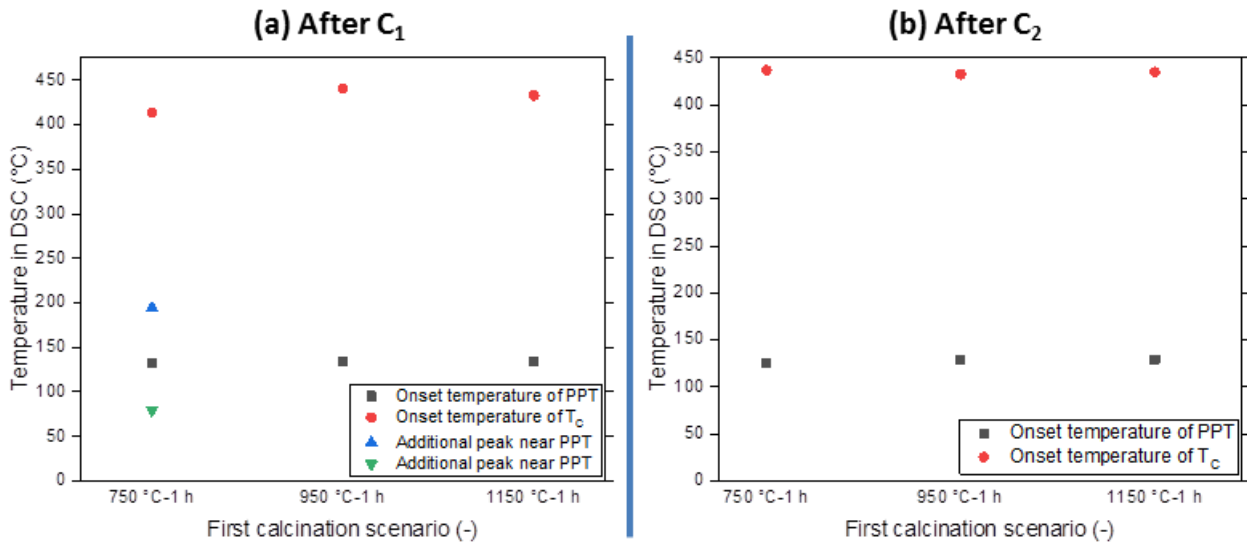


**Figure 57: DSC results of samples with  $C_1 = 750\text{ }^{\circ}\text{C-1 h}$ ;  $950\text{ }^{\circ}\text{C-1 h}$ ;  $1150\text{ }^{\circ}\text{C-1 h}$  after  $C_1$  (a) and after  $C_2$  ( $925\text{ }^{\circ}\text{C-10 h}$ ) (b)**

From the results of Li-doping on KNN ceramics presented in Figure 28, it is already established that the  $T_{O-T}$  should be around  $130\text{ }^{\circ}\text{C}$  for KNLN-3 ceramics. From the DSC results of the  $C_1=950\text{ }^{\circ}\text{C-1 h}$  and  $1150\text{ }^{\circ}\text{C-1 h}$  samples, we see that the onset of  $T_{O-T}$  does occur at around this temperature. Hence, we can establish that there is no lithium evaporation even for the higher  $C_1$  temperature samples after both  $C_1$  and  $C_2$ . Therefore, the peak broadening observed in the XRD after  $C_1$  is most likely due to the formation of nano-fragments after sieving or oxygen vacancies from the high



temperatures. The former is seen to be clearly present through SEM images of the powders after each calcination and sieving as shown in [Section-4.3](#), while investigation into the latter was not explored due to lack of time

Additionally, the lithium amount could also be correlated with the position of the  $T_c$  as mentioned before, which occurs as a trough in the DSC results at about 430 °C for all samples. This value also corresponds to the  $T_c$  observed for KNLN-3 as seen in [Figure 28](#). Since this onset temperature for the Curie transition is constant for all the samples after  $C_1$  and  $C_2$ , it is further confirmed that there is no lithium evaporation in any of the samples.

From the DSC results of the  $C_1=750$  °C-1 h sample, it was seen that several peaks arise above and below the 130 °C temperature mark apart from the peak associated with the PPT as shown in [Figure 57 \(a\)](#). This is attributed to the precursors losing absorbed moisture [114], [115] (presence of the unreacted powder/precursors is also seen in XRD for this sample after  $C_1$  in [Figure 56](#)). Furthermore, in the same sample after  $C_2$  shown in [Figure 57 \(b\)](#), the peaks seem to have disappeared which confirms the reaction to be complete, which is also seen in XRD.

#### 4.2.3.2 First calcination dwelling time variation

The XRD results of the samples with  $C_1$  temperatures of 950 °C and 1050 °C are shown for both  $C_1$  dwelling times of 1 hour and 3 hours in [Figure 58](#) with the miller indices marked for each peak.

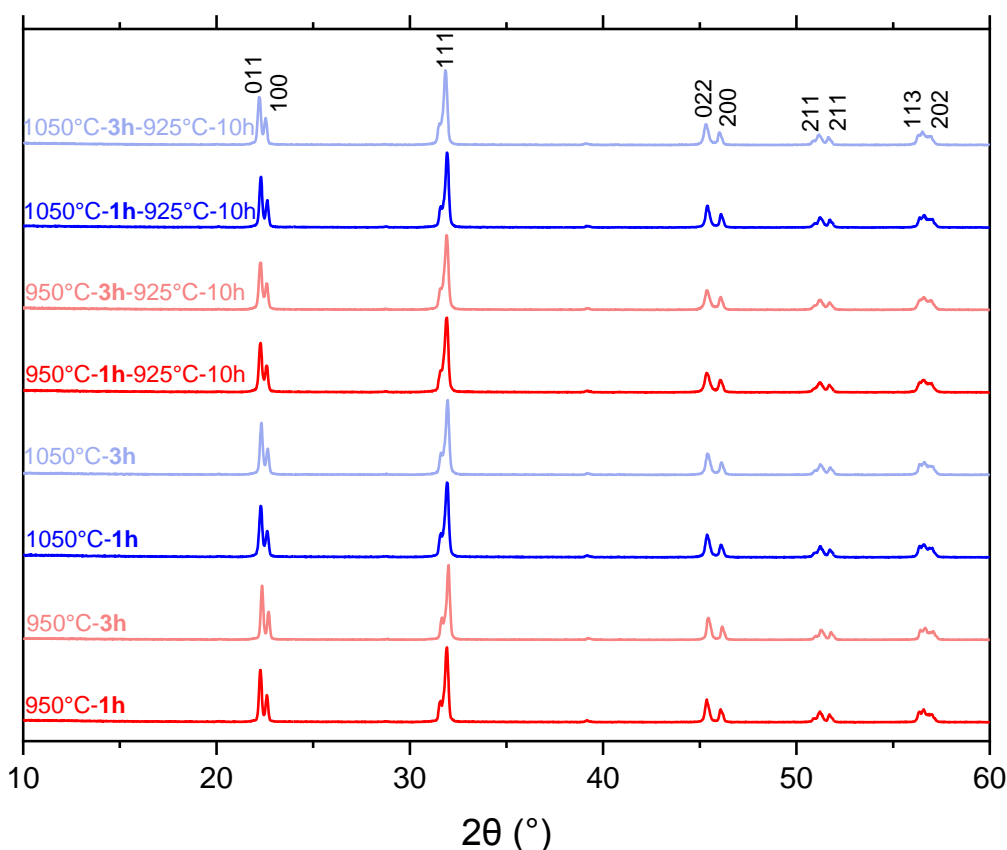


**Figure 58:** XRD results of the samples with  $C_1= 950$  °C-1 h;  $950$  °C-3 h;  $1050$  °C-1 h and  $1050$  °C-3 h after  $C_1$  and  $C_2$  ( $925$  °C-10 h)

From the XRD results, it is clear that in all cases KNLN-3 has been formed with no secondary phases (typically observed in the 25-30 ° region) after both  $C_1$  and  $C_2$  with no remaining reactants. No peak broadening is observed

(typically observed as a broadening in the (111) peak) for any sample which indicates that the phases are formed without any defects even from the increased  $C_1$  dwelling time

The DSC results of the  $C_1$  dwelling time variation samples are shown in Figure 59 after  $C_2$  to check for potential lithium evaporation. DSC results after  $C_1$  are not shown as it was already established that there was no Li evaporation for samples having  $C_1$  temperatures between 950 °C and 1050 °C after  $C_1$ . From the DSC results of the  $C_1$  dwelling time variation samples after  $C_2$ , it can be seen that all the samples had a constant onset temperature for the PPT and  $T_c$  transitions. Additionally, all the onset temperatures corresponded to the values presented in Figure 28, which suggests that there was no lithium evaporation in any of the samples. Thus, it is established through XRD and DSC, that for both  $C_1$  dwelling times tested, no change in phase purity is observed.

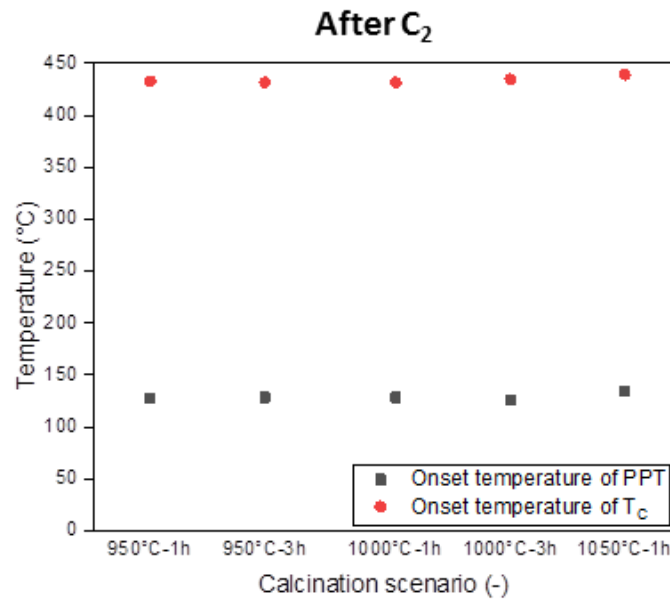


Figure 59: DSC results of the  $C_1$  dwelling time variation samples after  $C_2$  (925 °C-10 h)

#### 4.2.4 Surface waviness

The results of the surface waviness of R50 composites made with the calcination study powders are presented in Figure 60 (a) for the  $C_1$  temperature variation samples and Figure 60 (a) for the  $C_1$  dwelling time variation samples respectively. The surface waviness was investigated for all the samples used for the calcination study with the same settings used in the confocal microscope as in Section-4.1. From the results presented in Figure 60 (a), it can be seen that the average  $W_a$  for all the samples ranged between 0.75  $\mu\text{m}$  for the sample with  $C_1 = 850$  °C-1 h to 3.5  $\mu\text{m}$  for the sample with  $C_1 = 750$  °C-1 h. For the dwelling time variation samples presented in Figure 60 (b), the average  $W_a$  is seen to range from 4  $\mu\text{m}$  for the sample with  $C_1 = 1000$  °C-3 h to 2  $\mu\text{m}$  for the sample with  $C_1 = 950$  °C-1 h.

The very low variation in the surface waviness data compared to the samples in Section-4.1, suggested that the agglomerate sizes were below the thickness of the composite. This is expected since the agglomerates sizes were regulated by passing through a sieve with a mesh size of 63  $\mu\text{m}$ . Therefore, it can be seen that changing the calcination settings does not influence the formation of very large agglomerates that are bigger than the thickness of the composite. Furthermore, these changes in surface waviness have no observable effect on the  $d_{33}$  which is also seen in Section-4.1.4. The small changes in the surface waviness in the samples could be attributed to small-scale sample-to-sample variation. The very low surface variation also aided the poling process since almost none of the samples short-circuited. Hence, the change in the  $d_{33}$  among the calcination study samples should be attributed to

the different microstructures formed inside the composite. This is investigated with SEM images and particle size distributions of the powders after each calcination in [Section-4.3](#) and [Section-4.4](#) respectively.

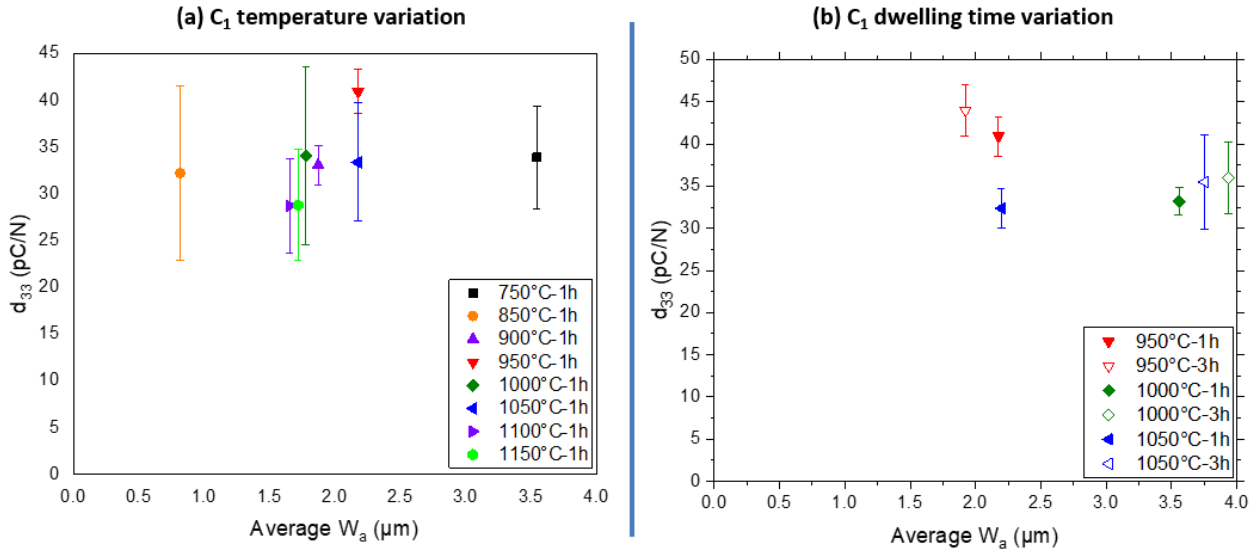


Figure 60:  $d_{33}$  vs the average  $W_a$  for the  $C_1$  temperature variation samples (a) and  $C_1$  dwelling time variation samples (b)

## 4.3 Particle size analysis

### 4.3.1 First calcination temperature variation

SEM was used to visualize the microstructure after each calcination and sieving processes. Sieving was performed before SEM so that a usable powder with no very large agglomerates was obtained. The SEM was performed before the ball-milling process as it drastically affected the microstructure which required a separate study to be performed as described in [Section-4.5](#). The SEM images after  $C_1$  and  $C_2$  is presented for three samples with  $C_1$  scenarios:  $C_1 = 750^\circ\text{C}-1\text{h}$  ((a) after  $C_1$  and (b) after  $C_2$ ),  $C_1 = 950^\circ\text{C}-1\text{h}$  ((c) after  $C_1$  and (d) after  $C_2$ ) and  $C_1 = 1150^\circ\text{C}-1\text{h}$  ((e) after  $C_1$  and (f) after  $C_2$ ) in [Figure 61](#) at 5000x magnification for viewing the grains and in [Figure 62](#) at 50x magnification for viewing the sintered agglomerates.

From [Figure 61 \(a\)](#) and [Figure 61 \(c\)](#), it can be seen that for the  $C_1 = 750^\circ\text{C}-1\text{h}$  and  $950^\circ\text{C}-1\text{h}$  samples, the grain sizes are small after  $C_1$  respectively. From [Figure 61 \(b\)](#) and [Figure 61 \(d\)](#), it can be seen that after  $C_2$ , the grain sizes for both samples seem to reach about the same size. For the  $C_1 = 1150^\circ\text{C}-1\text{h}$  sample, the grain size is largest after  $C_1$  as seen in [Figure 61 \(e\)](#). These grains become the same size compared to the other samples after  $C_2$  as seen in [Figure 61 \(f\)](#). Also, It is seen in [Figure 61 \(e\)](#) that after  $C_1$ , this sample contains nano-particles that stick to the bigger grains. From [Figure 62 \(a\)](#) and [Figure 62 \(c\)](#), it can be seen that for  $C_1 = 750^\circ\text{C}-1\text{h}$  and  $950^\circ\text{C}-1\text{h}$  samples, the sintered agglomerate sizes are small and less in number after  $C_1$  respectively. From [Figure 62 \(b\)](#) and [Figure 62 \(d\)](#), it can be seen that after  $C_2$ , the agglomerates from both samples seem to reach about the same size and number. For the  $C_1 = 1150^\circ\text{C}-1\text{h}$  calcined sample, the agglomerates are largest in size and number after  $C_1$  as seen in [Figure 62 \(e\)](#). These agglomerates become the same size and numbers as the other samples after  $C_2$  as seen in [Figure 62 \(f\)](#).

For the samples with  $C_1 = 750^\circ\text{C}-1\text{h}$  and  $950^\circ\text{C}-1\text{h}$ , there is less grain growth and sintering after  $C_1$  which is attributed to their lower  $C_1$  temperatures. Due to the reduced grain and agglomerate sizes in these samples the effect of ball-milling in breaking the formed grains and agglomerates is reduced. Furthermore, owing to their low grain growth and sintering during  $C_1$ , there is potential energy left within them for subsequent grain growth and

sintering during  $C_2$  which yield a moderate size in their grains and agglomerates after  $C_2$ . This is ascribed to the energy stored within the grain boundaries for grain boundary diffusion and grain boundary migration responsible for grain growth and sintering in ceramics [116].

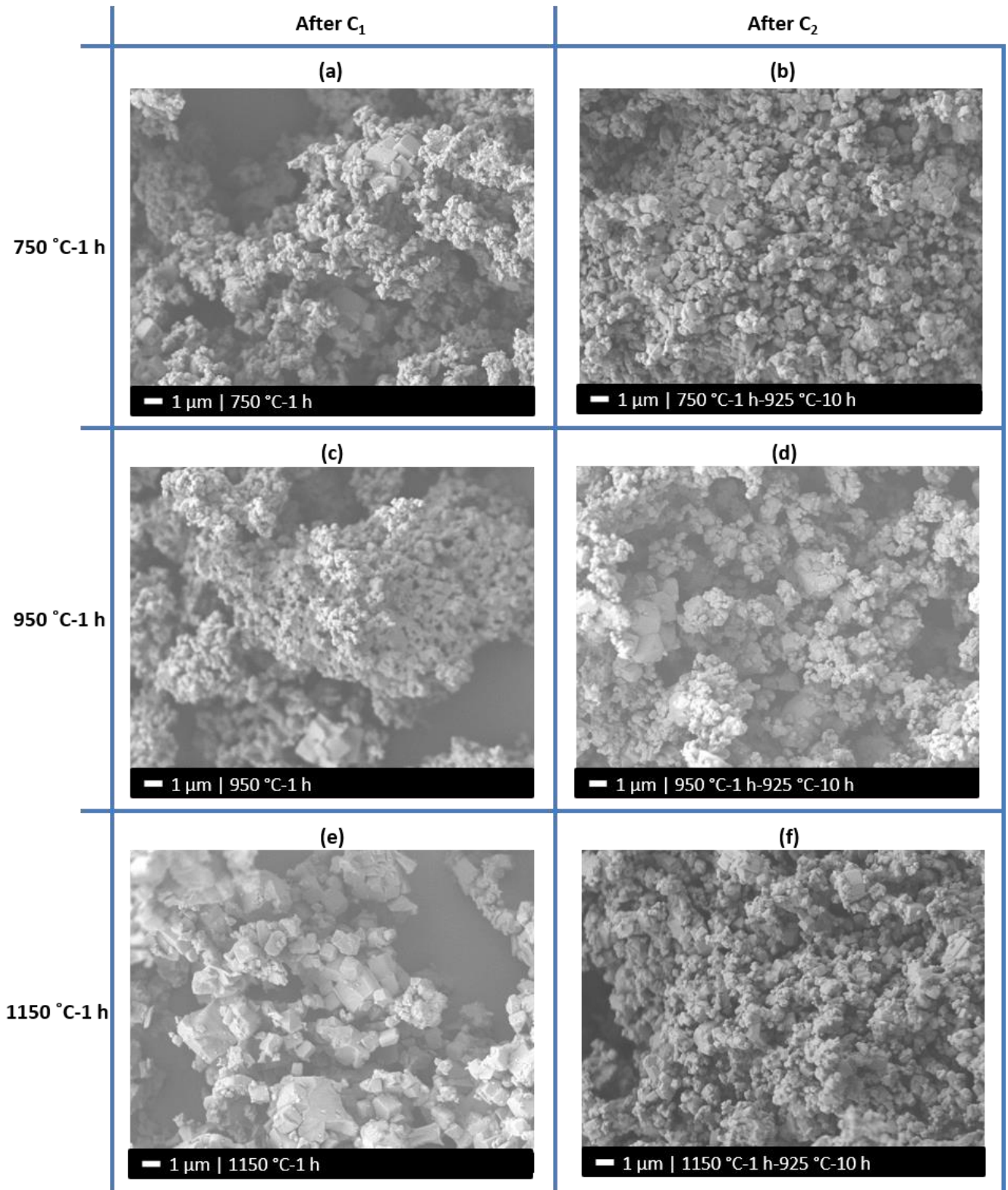
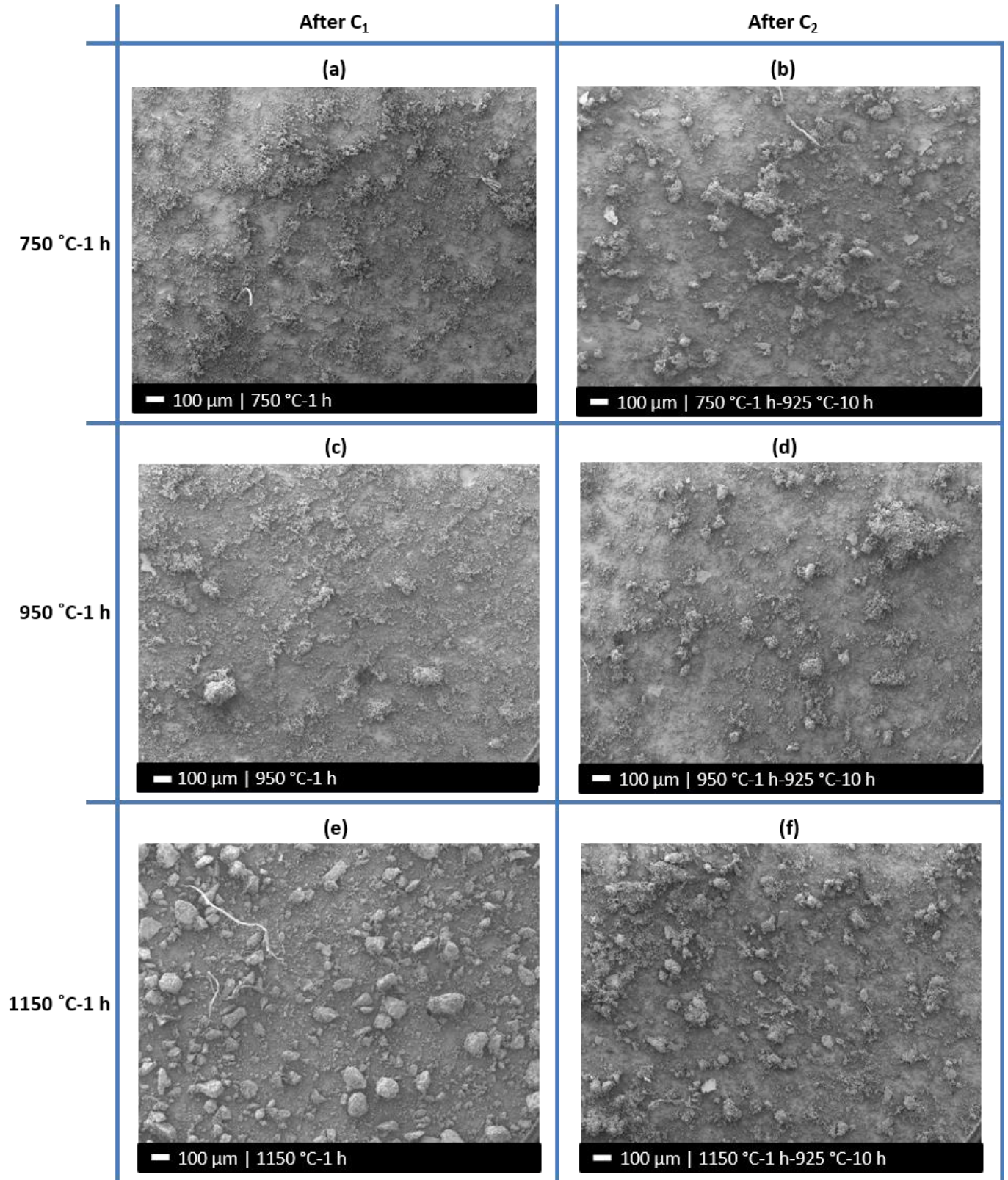


Figure 61: Grains of KNLN-3 visualized with SEM (5000x magnification) for three  $C_1$  temperatures after  $C_1$  and  $C_2$  (925 °C-10 h):  $C_1$  = 750 °C-1 h after  $C_1$  (a),  $C_1$  = 750 °C-1 h after  $C_2$  (b);  $C_1$  = 950 °C-1 h after  $C_1$  (c),  $C_1$  = 950 °C-1 h after  $C_2$  (d);  $C_1$  = 1150 °C-1 h after  $C_1$  (e),  $C_1$  = 1150 °C-1 h after  $C_2$  (f)





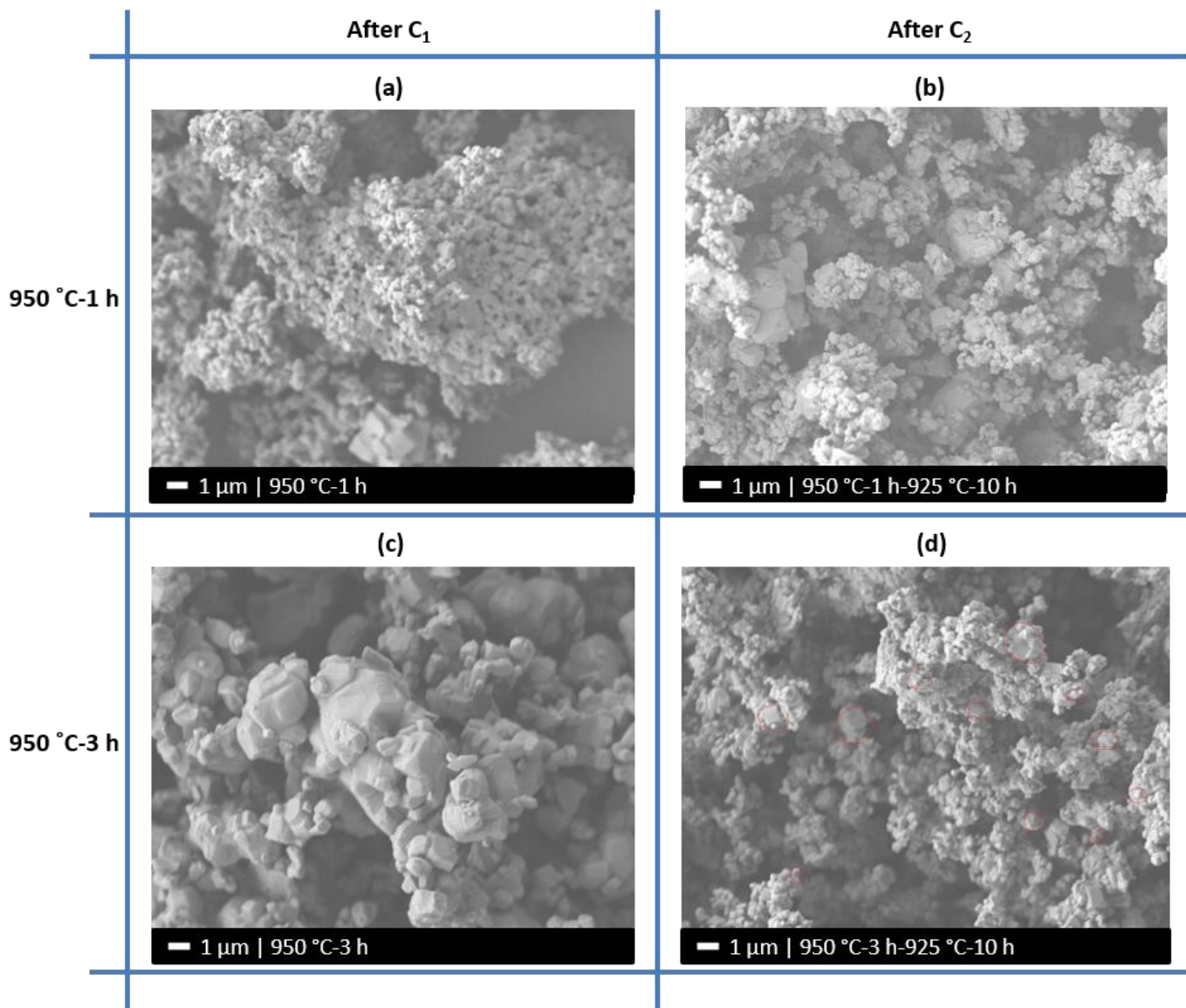
**Figure 62: Sintered agglomerates visualized with SEM (50x magnification) for three  $C_1$  temperatures after  $C_1$  and  $C_2$  (925 °C-10 h):  $C_1$  = 750 °C-1 h after  $C_1$  (a),  $C_1$  = 750 °C-1 h after  $C_2$  (b);  $C_1$  = 950 °C-1 h after  $C_1$  (c),  $C_1$  = 950 °C-1 h after  $C_2$  (d);  $C_1$  = 1150 °C-1 h after  $C_1$  (e),  $C_1$  = 1150 °C-1 h after  $C_2$  (f)**

Similarly, the higher grain sizes; agglomerate sizes and agglomerate numbers after  $C_1$  in the  $C_1$ =1150 °C-1 h sample is attributed to its high  $C_1$  temperature which would have caused additional grain growth and sintering in the powder

respectively. The subsequent reduction in the grain and agglomerate sizes was due to the breakage of agglomerates and grains by the ball-milling process. Furthermore, due to the high grain growth and sintering that occur in the powder during  $C_1$ , the powder has already expended most of the potential energy for grain growth and sintering stored within it. This brings it to a state of thermodynamic equilibrium thus, yielding little to no subsequent regrowth of grains and agglomerates during  $C_2$  after the ball-milling process. Hence, after  $C_2$  the grain and agglomerate size is seen to be comparable to the  $C_1=750\text{ }^{\circ}\text{C-1 h}$  and  $950\text{ }^{\circ}\text{C-1 h}$  samples. It is also seen that after  $C_1$  nano-particles are present for this sample which are produced during the sieving process done before the SEM.

### 4.3.2 First calcination dwelling time variation

The SEM images of powders after  $C_1$  and  $C_2$  is presented for two  $C_1$  temperatures under two  $C_1$  dwelling times:  $C_1 = 950\text{ }^{\circ}\text{C-1 h}$  ((a) after  $C_1$  and (b) after  $C_2$ ),  $C_1 = 950\text{ }^{\circ}\text{C-3 h}$  ((c) after  $C_1$  and (d) after  $C_2$ ),  $C_1 = 1050\text{ }^{\circ}\text{C-1 h}$  ((e) after  $C_1$  and (f) after  $C_2$ ),  $C_1 = 1050\text{ }^{\circ}\text{C-3 h}$  ((g) after  $C_1$  and (h) after  $C_2$ ) in Figure 63 at 5000x magnification for viewing the grains and in Figure 64 at 50x magnification for viewing the sintered agglomerates. The SEM was performed after each calcination and sieving processess but before the ball-milling procedure just like in [Section-4.3.1](#) as the ball-milling process drastically affected the microstructure which required a separate study to be performed as described in [Section-4.5](#)





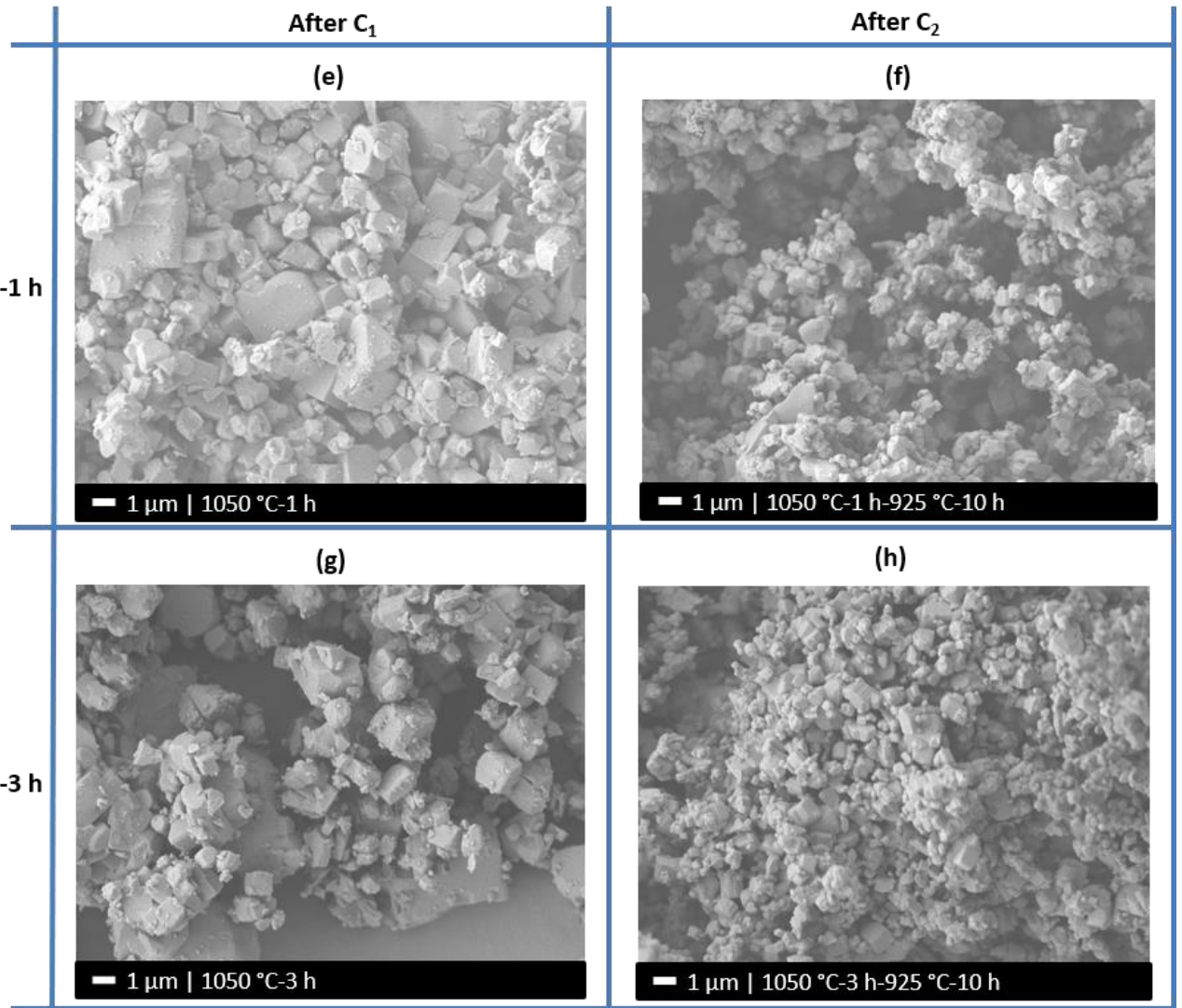
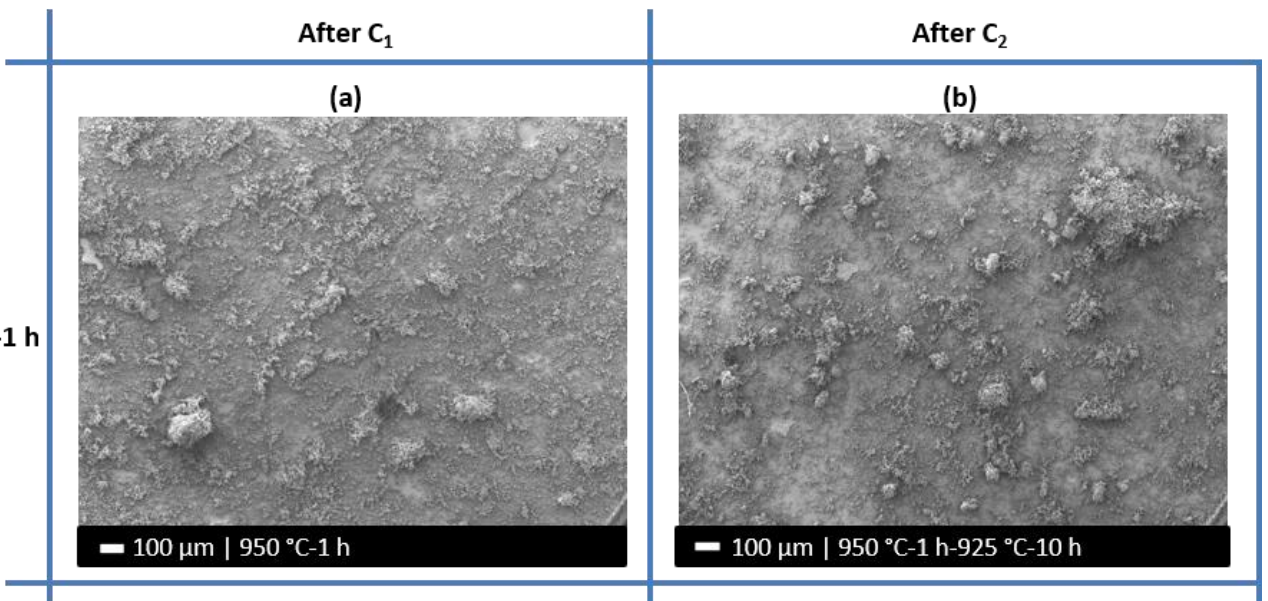


Figure 63: Grains of KNLN-3 visualized with SEM (5000x magnification) for two  $C_1$  temperatures under two  $C_1$  dwelling times after  $C_1$  and  $C_2$ :  $C_1 = 950$  °C-1 h after  $C_1$  (a),  $C_1 = 950$  °C-1 h after  $C_2$  (b);  $C_1 = 950$  °C-3 h after  $C_1$  (c),  $C_1 = 950$  °C-3 h after  $C_2$  (d);  $C_1 = 1050$  °C-1 h after  $C_1$  (e),  $C_1 = 1050$  °C-1 h after  $C_2$  (f) and  $C_1 = 1050$  °C-3 h after  $C_1$  (g),  $C_1 = 1050$  °C-3 h after  $C_2$  (h)



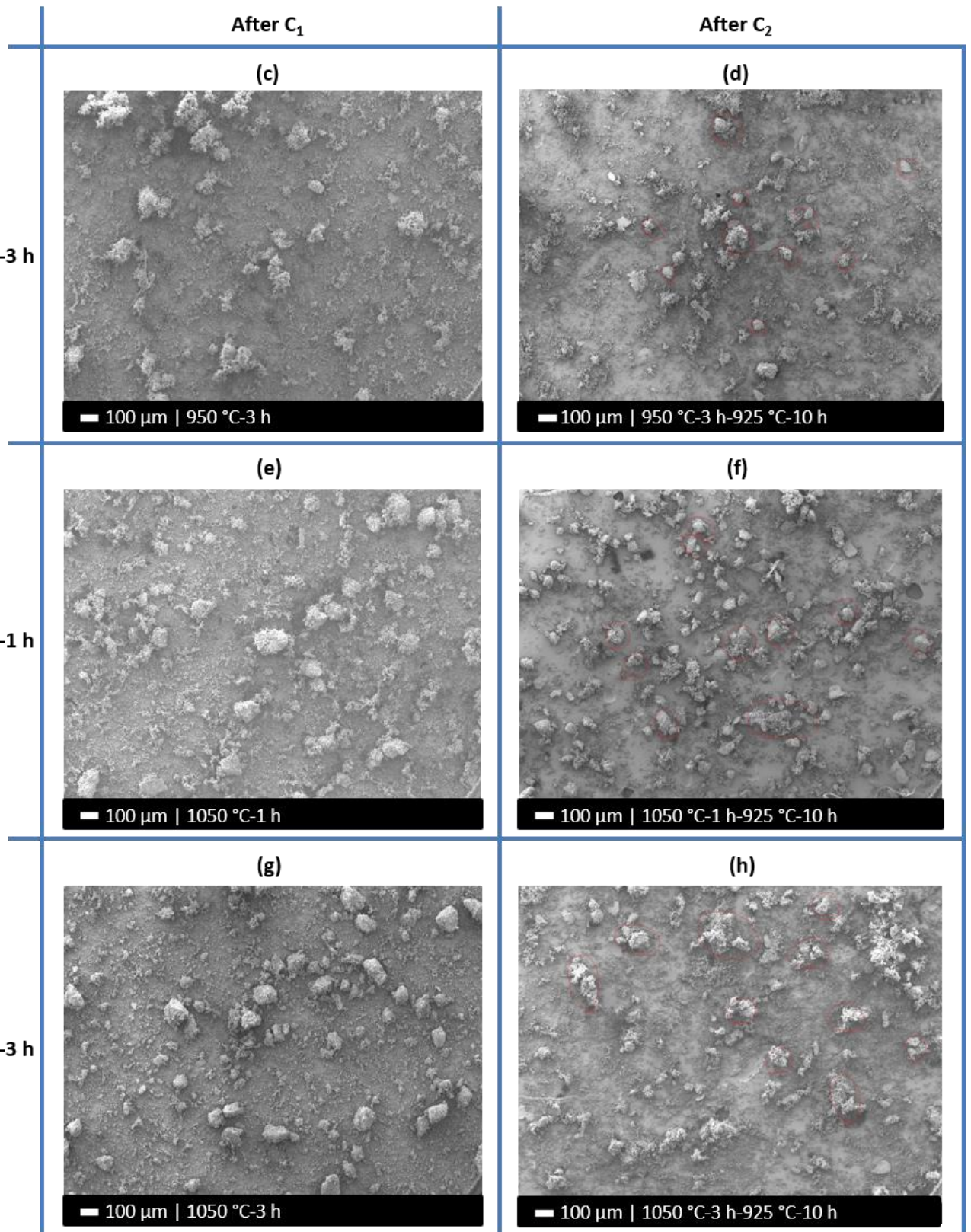


Figure 64: Sintered agglomerates of KNLN-3 powder visualized with SEM (50x magnification) for two  $C_1$  temperatures under two  $C_1$  dwelling times after  $C_1$  and  $C_2$ :  $C_1 = 950$  °C-1 h after  $C_1$  (a),  $C_1 = 950$  °C-1 h after  $C_2$  (b);  $C_1 = 950$  °C-3 h after  $C_1$  (c),  $C_1 = 950$  °C-3 h after  $C_2$  (d);  $C_1 = 1050$  °C-1 h after  $C_1$  (e),  $C_1 = 1050$  °C-1 h after  $C_2$  (f) and  $C_1 = 1050$  °C-3 h after  $C_1$  (g),  $C_1 = 1050$  °C-3 h after  $C_2$  (h)



For  $C_1 = 950\text{ }^{\circ}\text{C}$ -1 h sample after  $C_1$ , the grain size is smaller than the other samples as seen in [Figure 63 \(a\)](#). After  $C_2$ , the grain size becomes comparably equal to the other samples as seen in [Figure 63 \(b\)](#). In the  $C_1 = 950\text{ }^{\circ}\text{C}$ -3 h sample, the grain size is much bigger compared to the  $C_1 = 950\text{ }^{\circ}\text{C}$ -1 h sample after  $C_1$ , as seen [Figure 63 \(c\)](#). The grain size after  $C_2$  becomes comparably equal to the other samples as seen in [Figure 63 \(d\)](#). For the  $C_1 = 1050\text{ }^{\circ}\text{C}$ -1 h and  $1050\text{ }^{\circ}\text{C}$ -3 h samples the grain sizes and their variation after  $C_1$  and  $C_2$  is the same as for the  $C_1 = 950\text{ }^{\circ}\text{C}$ -3 h sample albeit with nano-particles being present after  $C_1$ . These are seen in [Figure 63 \(e\) - \(h\)](#) respectively.

For the  $C_1 = 950\text{ }^{\circ}\text{C}$ -1 h sample, after  $C_1$ , the agglomerate size and numbers are smaller than the other samples as seen in [Figure 64 \(a\)](#). After  $C_2$ , the agglomerate size and numbers becomes comparably equal to the other samples as seen in [Figure 64 \(b\)](#). For the  $C_1 = 950\text{ }^{\circ}\text{C}$ -3 h sample, the agglomerates are much bigger and more in number compared to the  $C_1 = 950\text{ }^{\circ}\text{C}$ -1 h sample after  $C_1$ , as seen [Figure 64 \(c\)](#). The agglomerate size and numbers after  $C_2$  becomes comparably equal to the other samples as seen in [Figure 64 \(d\)](#). For the  $C_1 = 1050\text{ }^{\circ}\text{C}$ -1 h and  $1050\text{ }^{\circ}\text{C}$ -3 h samples the agglomerate sizes, numbers and their variation after  $C_1$  and  $C_2$  is the same as for the  $C_1 = 950\text{ }^{\circ}\text{C}$ -3 h sample. These are seen in [Figure 64 \(e\) - \(h\)](#) respectively.

Higher grains and agglomerate sizes are noticed for the  $C_1 = 950\text{ }^{\circ}\text{C}$ -3 h sample compared to the  $C_1 = 950\text{ }^{\circ}\text{C}$ -1 h sample due to the additional grain growth and sintering associated with a higher  $C_1$  dwelling time. The grain and agglomerate sizes are seen to become practically equal for all samples after  $C_2$ . This is attributed to the breaking of the large grains and agglomerates during ball-milling for samples which have had a higher  $C_1$  dwelling time and  $C_1$  temperature balanced with the amount of potential energy left for subsequent grain growth and sintering in the powder as explained in [Section-4.3.1](#). Through SEM, the effects of each process during preparation of the ceramic was established. However, the exact reason for a trend in the  $d_{33}$  with each calcination scenario remains to be seen with accurate reasoning. For this, a more quantitative analysis on the microstructure of the calcination study samples was performed through particle size distribution analysis which is presented in [Section-4.4](#).

## 4.4 Particle size distribution analysis

Particle size distribution (PSD) analysis was done on the powders that were used for the  $C_1$  temperature variation experiment. The descriptions of the samples that were analyzed is shown in [Appendix B7](#). It is to be noted that, the analysis was not done for  $C_1 = 900\text{ }^{\circ}\text{C}$ -1 h and  $850\text{ }^{\circ}\text{C}$ -1 h samples due to a lack of material. The PSD analysis was performed on the powders that had been subjected to the sieving process following  $C_1$  and  $C_2$  due to the necessity that very large agglomerates (produced after  $C_1$  and  $C_2$ ) must not be present in the powder during analysis to prevent sedimentation. Additionally, the PSD was performed before the ball-milling process as it drastically affected the microstructure and thus, required a separate study to be performed. This is described in [Section-4.5](#).

### 4.4.1 First calcination temperature variation

The PSD curves describing the volume density (%) of particles vs the size classes ( $\mu\text{m}$ ) for the  $C_1$  temperature variation samples after  $C_1$  and  $C_2$  is shown in [Figure 65 \(a\)](#) and [Figure 65 \(b\)](#) respectively. From the PSD results, it is seen that after  $C_1$ , for  $C_1 = 750\text{ }^{\circ}\text{C}$ -1 h and  $950\text{ }^{\circ}\text{C}$ -1 h samples, there is a unimodal distribution of the particles with a tightly distributed peak. The peak is located at a higher particle size in the  $C_1 = 950\text{ }^{\circ}\text{C}$ -1 h sample ( $\approx 7\text{ }\mu\text{m}$ ) compared to the  $C_1 = 750\text{ }^{\circ}\text{C}$ -1 h sample ( $\approx 2\text{ }\mu\text{m}$ ). The  $C_1 = 1050\text{ }^{\circ}\text{C}$ -1 h and  $1150\text{ }^{\circ}\text{C}$ -1 h samples have almost overlapping curves with a bimodal distribution of particles. The lower particle size peak is located close to the peaks of the  $C_1 = 750\text{ }^{\circ}\text{C}$ -1 h and  $950\text{ }^{\circ}\text{C}$ -1 h samples at  $\approx 10\text{ }\mu\text{m}$  and the higher particle size peak is located at  $\approx 100\text{ }\mu\text{m}$ . From the PSD results for the same samples after  $C_2$ , it is seen that all curves acquire a unimodal distribution with particles ranging from  $0.3 - 20\text{ }\mu\text{m}$  in size with a tighter distribution of the peak specifically seen for the  $C_1 = 950\text{ }^{\circ}\text{C}$ -1 h sample.

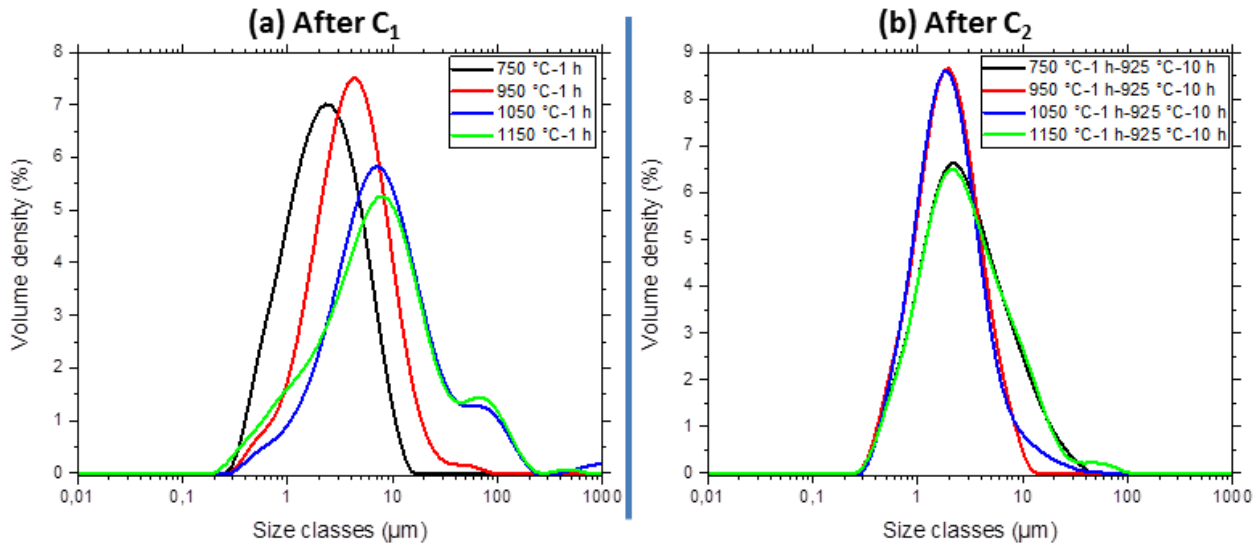


**Figure 65: PSD curves of volume density (%) vs the size classes (μm) for the C<sub>1</sub> temperature variation samples after C<sub>1</sub> (a) and after C<sub>2</sub> (b)**

For C<sub>1</sub> = 750 °C-1 h sample, the peak is unimodal and the particle size corresponding to this peak is lowest after C<sub>1</sub> owing to the lowest amount of grain growth and sintering associated with the C<sub>1</sub> temperature. For the C<sub>1</sub> = 950 °C-1 h sample, the peak is again unimodal but it is located at a higher particle size due to the intermediate C<sub>1</sub> temperature. For the C<sub>1</sub> = 1050 °C-1 h and 1150 °C-1 h samples, there is a bimodal distribution of particles and the lower particle size peak is located at a higher particle size due to the extensive grain growth and sintering that occurs at these C<sub>1</sub> temperatures. After C<sub>2</sub>, all the samples have a mostly unimodal distribution due to a balance between the effectiveness of the ball-milling process on the powder (which breaks up agglomerates and grains for the samples which have them) and the potential energy left for subsequent grain growth and sintering during C<sub>2</sub> (which is mostly present for the lower C<sub>1</sub> temperature samples) as explained in [Section-4.3.1](#). Thus, reproducible results are obtained here with respect to SEM on the variation of C<sub>1</sub> temperature in these powders.

The results of the particle size distribution parameters represented as 'D<sub>x</sub>' vs the C<sub>1</sub> temperatures for the samples are shown in Figure 66. The 'D<sub>x</sub>' parameter in particle size distribution is used to indicate maximum of the sizes of particles present in the sample occupied by the x % of the particles present. Thus, for example, D<sub>10</sub> is the parameter used to describe the size below which only 10 % of the particles fall.

The D<sub>10</sub> here is indicative of the loose grains and the nano-fragments which are typically the smallest particles present in the powders. Generally, the smaller the D<sub>10</sub>, the more numerous the smaller grains that are present in the powder. From Figure 66 (a), it is seen that after C<sub>1</sub>, the D<sub>10</sub> seems to increase from C<sub>1</sub> = 750 °C-1 h up to 1050 °C-1 h and then decreases thereafter with increase in C<sub>1</sub> temperature. A drastic increase in D<sub>10</sub> is seen between C<sub>1</sub>=950 °C-1 h and C<sub>1</sub>=1000 °C-1 h samples. Similarly, a drastic decrease in D<sub>10</sub> is seen between C<sub>1</sub>=1100 °C-1 h and C<sub>1</sub>=1150 °C-1 h samples. A similar trend can be seen for the D<sub>50</sub> and the D<sub>90</sub> vs the C<sub>1</sub> temperatures shown in Figure 66 (b) and Figure 66 (c) where-in there is an increase of the sizes after C<sub>1</sub> up to C<sub>1</sub> temperatures of 1000-1050 °C and there is a decrease in them thereafter. Again, a drastic increase in both the parameters between C<sub>1</sub>=950 °C-1 h and C<sub>1</sub>=1000 °C-1 h samples is observed. After C<sub>2</sub>, all the samples converge to a practically constant value of D<sub>10</sub>, D<sub>50</sub> and D<sub>90</sub>.

The increase of all the D<sub>x</sub> parameters after C<sub>1</sub> up to a C<sub>1</sub> temperature of 1000-1050 °C is attributed to the increased grain growth and sintering that occurs with increasing C<sub>1</sub> temperature. This is also why a drastic increase in the parameters is noticed between C<sub>1</sub>=950 °C-1 h and C<sub>1</sub>=1000 °C-1 h samples as the grain growth and sintering becomes

much more effective during the transition between these two temperatures. The decrease of the  $D_x$  parameters after 1000-1050 °C  $C_1$  temperatures is attributed to partial breakage of grains and agglomerates during sieving as the  $Y_2O_3/Zr_2O_3$  balls used during ball-milling are also used here (to prevent static agglomeration) albeit with a much lower energy. After  $C_2$ , all the samples converge to a practically constant value of the  $D_{10}$ ,  $D_{50}$ ,  $D_{90}$  due to the effectiveness of the ball-milling process on the powder (which breaks up agglomerates and grains for the samples which have them) balanced with the energy left for subsequent grain growth and sintering during  $C_2$  as explained in [Section-4.3.1](#).

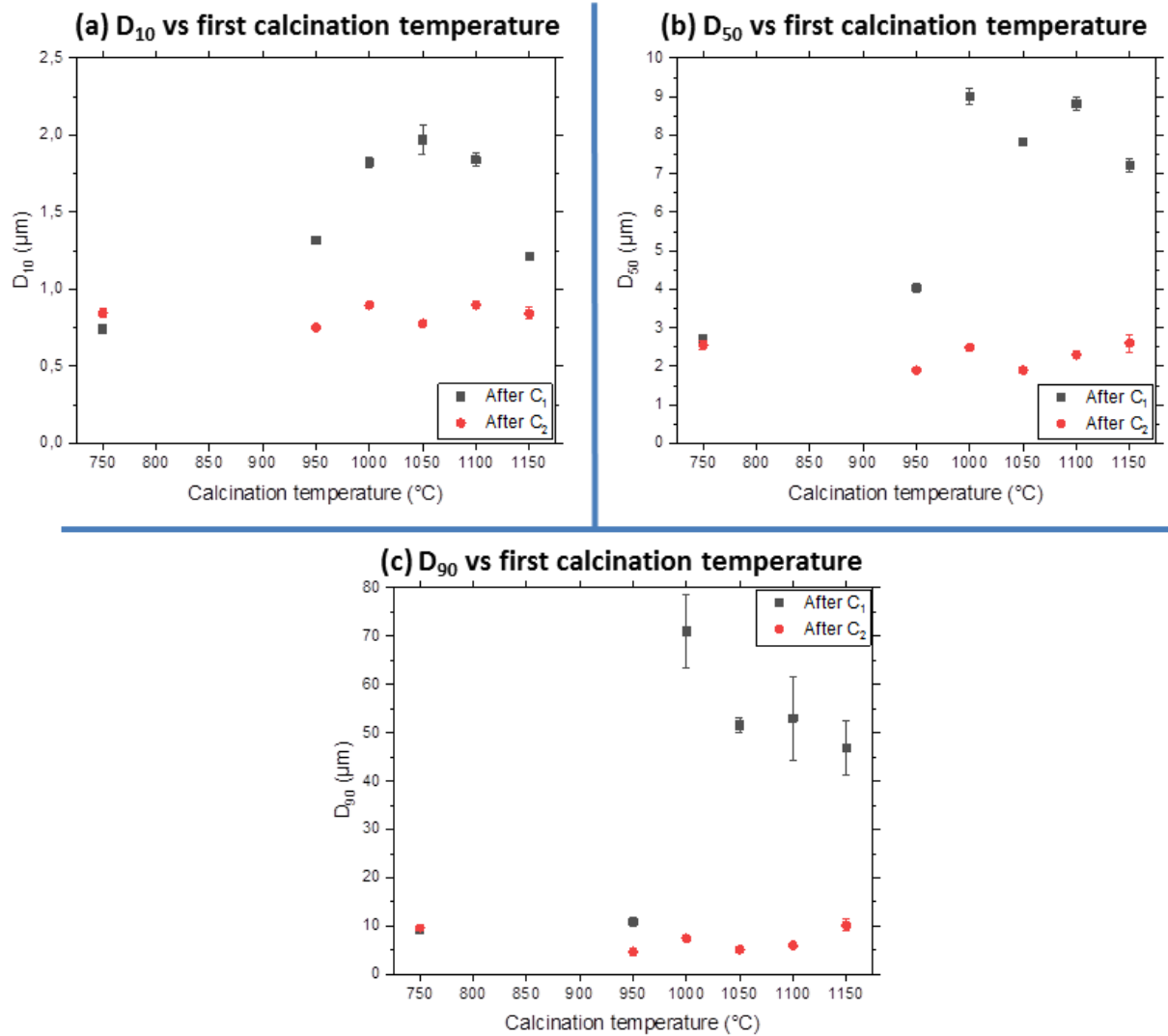


**Figure 66:  $D_{10}$  (a);  $D_{50}$  (b) and  $D_{90}$  (c) vs  $C_1$  temperature of the calcination study samples**

#### 4.4.2 First calcination dwelling time variation

The PSD curves describing the volume density (%) of particles vs the size classes (μm) for the  $C_1$  dwelling time variation samples after  $C_1$  and  $C_2$  is shown in [Figure 67 \(a\)](#) and [Figure 67 \(b\)](#) respectively.

From the PSD results after  $C_1$ , it is seen that the  $C_1 = 950$  °C-1 h and 1050 °C-1 h samples follow a unimodal and bimodal distribution in the particles respectively with the peaks situated at higher particle sizes for the  $C_1 = 1050$  °C-1 h sample, as seen previously in [Figure 65](#). With increasing  $C_1$  dwelling time from 1 hour to 3 hours, the  $C_1 = 950$  °C-1 h sample starts showing a bimodal distribution with its peaks almost corresponding to the peaks of  $C_1 = 1050$  °C-1 h

sample. However, the higher particle size peak is higher (in-terms of volume density) compared to the one in the  $C_1 = 1050\text{ }^{\circ}\text{C}-1\text{ h}$  sample. The same effect is seen for the  $C_1 = 1050\text{ }^{\circ}\text{C}-3\text{ h}$  sample albeit with the peaks located at higher particle sizes. Furthermore, the higher particle size peak is the highest and the lower particle size peak is the lowest in this sample compared to the other samples. After  $C_2$ , it is seen that all the samples converge to an array of unimodal curves with a tight distribution around  $1\text{--}10\text{ }\mu\text{m}$  with only the  $C_1 = 950\text{ }^{\circ}\text{C}-3\text{ h}$  sample having a small amount of particles left in the size class of  $\approx 11\text{ }\mu\text{m}$ .

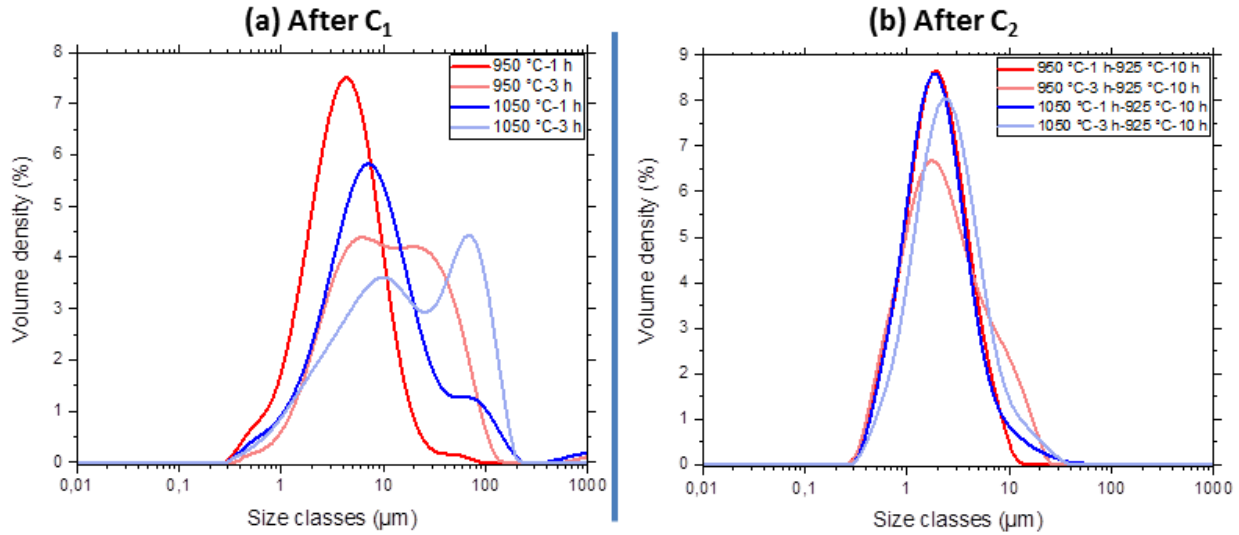


**Figure 67: PSD curves of volume density (%) vs the size classes (μm) for the  $C_1$  dwelling time variation samples after  $C_1$  (a) and after  $C_2$  (b)**

The occurrence of bimodality and the shift of the peaks to higher particle sizes in the  $C_1 = 1050\text{ }^{\circ}\text{C}-1\text{ h}$  sample compared to the  $C_1 = 950\text{ }^{\circ}\text{C}-1\text{ h}$  sample is due to the increased grain growth and sintering that occurs at higher  $C_1$  temperatures as explained before. The same phenomena are seen in the samples with higher  $C_1$  dwelling times again due to an increased grain growth and sintering. After  $C_2$ , all the samples have a unimodal distribution due to a balance between the effectiveness of the ball-milling process on the powder (which breaks up agglomerates and grains for the samples which have them) and the energy left for subsequent grain growth and sintering during  $C_2$  (which is mostly present for the lower  $C_1$  temperature and dwelling time samples) as explained in [Section-4.3.1](#). Thus, reproducible results are obtained with respect to SEM and the particle size distributions on the  $C_1$  dwelling time variation powders.

The results of the particle size distribution parameters represented as ' $D_x$ ' vs the  $C_1$  temperatures are shown in Figure 68. From Figure 68 (a) – (c), it can be seen that after  $C_1$ , the  $D_{10}$ ,  $D_{50}$ ,  $D_{90}$  parameters seem to increase with increasing  $C_1$  temperature (which was already seen previously in the  $C_1$  temperature variation samples) and dwelling times. After  $C_2$ , the  $D_{10}$ ,  $D_{50}$ ,  $D_{90}$  parameters seem to converge to a practically constant value.

The increase in all the  $D_x$  parameters for samples with higher  $C_1$  dwelling times is due to the higher grain growth and sintering that occurs. There is a drastic decrease noticed in the  $D_{50}$ ,  $D_{90}$  of the  $C_1=1050\text{ }^{\circ}\text{C}-1\text{ h}$  sample which is attributed to the breaking of large grains and agglomerates (size range of  $D_{50}$ ,  $D_{90}$  corresponds to large grains and agglomerates) during sieving as explained before. However, the  $D_{50}$ ,  $D_{90}$  increase as the  $C_1$  dwelling time is increased to 3 hours for the same sample which could be due to the sieving process not being effective enough to break the very large grains and agglomerates formed.

After  $C_2$ , all the samples converge to a practically constant value of the  $D_{10}$ ,  $D_{50}$ ,  $D_{90}$  due to the effectiveness of the ball-milling process on the powder (which breaks up agglomerates and grains for the samples which have them) and the energy left for subsequent grain growth and sintering during  $C_2$  as explained before.

With regards to the peak observed in  $d_{33}$  for the  $C_1=950\text{ }^\circ\text{C}$ -1 h sample, it could be due to the tightest distribution of particles exhibited by this sample as seen in Figure 65. Due to this tight distribution of the particles, the densification/packing in its microstructure is less than the other samples which could've indirectly increased the thickness and thus, the  $d_{33}$  of the composite. This is because as the thickness (aspect ratio) of the composite is increased, the  $d_{33}$  is also increased due to non-linear additions from other  $d_{ij}$  modes thus, giving an incorrect value for  $d_{33}$  [117] in the Berlin-Court piezometer.

It is also seen that the  $C_1=1050\text{ }^\circ\text{C}$ -1 h sample also shows an almost equally tight distribution as that of the  $C_1=950\text{ }^\circ\text{C}$ -1 h sample but has a lower  $d_{33}$ . This could be due to the presence of nano-fragments produced during sieving and ball-milling after  $C_1$  and sieving after  $C_2$  of the powder as seen in [Section-4.3](#), that can pack better and potentially reduce the  $d_{33}$ . It could also be that the nano-fragments are non-piezoelectric in nature as discussed in [Section-2.7.4](#), and thus, reduce the  $d_{33}$  even further.

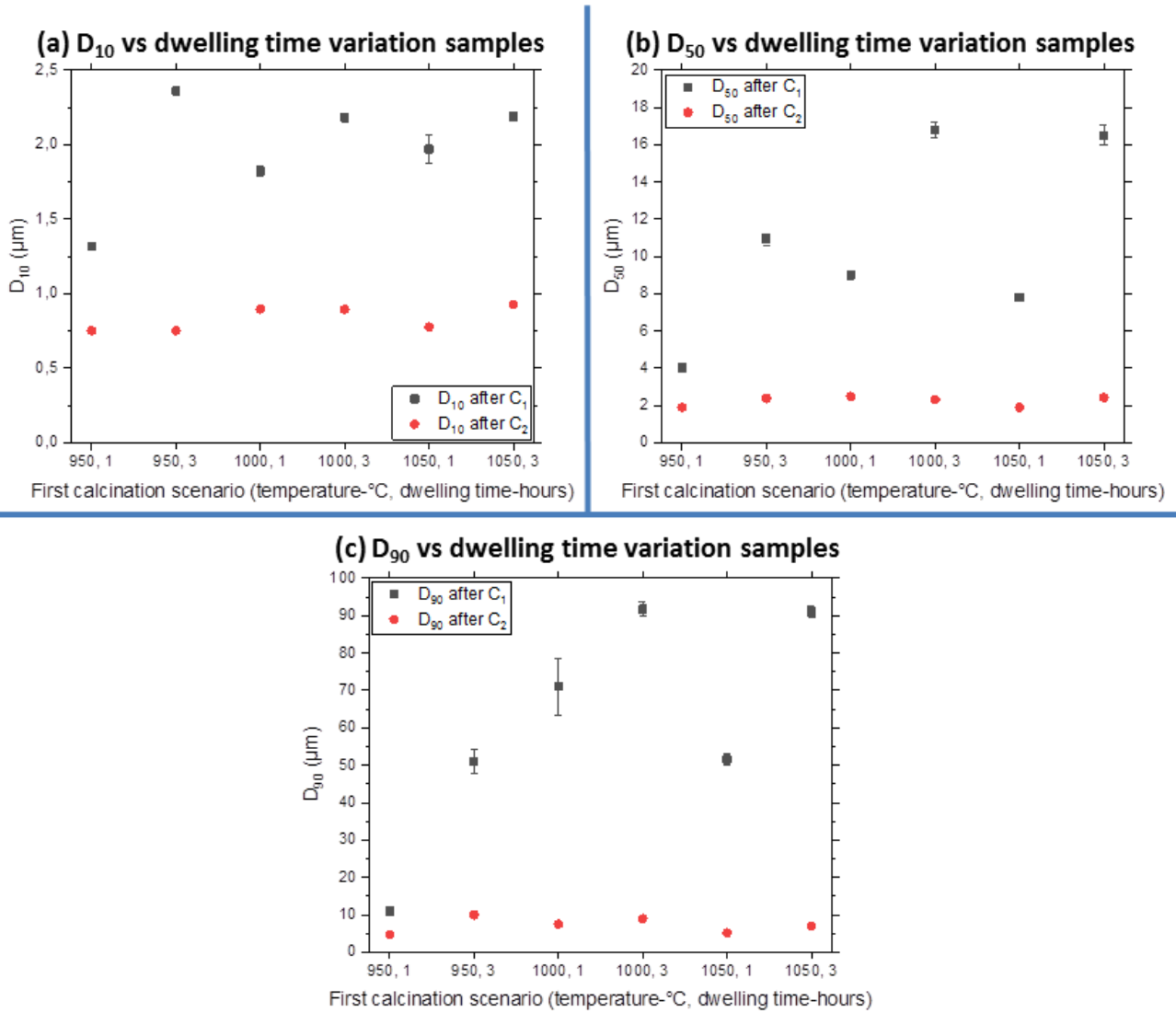


Figure 68: Variation of  $D_{10}$  (a);  $D_{50}$  (b) and  $D_{90}$  (c) for the  $C_1$  dwelling time variation samples

With regards to the peak observed in  $d_{33}$  for the  $C_1=950\text{ }^\circ\text{C}$ -3 h sample, we see that from Figure 67, this sample has the least tight distribution amongst all the other samples. However, in this case it could be the additional densification associated with a higher  $C_1$  dwelling time that effectively reduces interparticle distances within a sintered agglomerate thus, increasing  $d_{33}$ . The other two curves namely those of:  $C_1=1050\text{ }^\circ\text{C}$ -1 h and  $1050\text{ }^\circ\text{C}$ -3 h samples have a lowered  $d_{33}$  despite having a tighter distribution. This could be attributed to the presence of nano-fragments in the ceramic as mentioned before which is also seen in SEM images of the same in [Section-4.3](#). The tight distributions exhibited by the  $950\text{ }^\circ\text{C}$   $C_1$  temperature samples could be due to the perfect balance between grain growth and sintering after  $C_1$  and  $C_2$  with the breakage of the particles during ball-milling after  $C_1$ .

The nano-fragments seen for higher  $C_1$  temperature samples are  $\approx 0.1\text{ }\mu\text{m}$  and lower in size as seen through SEM which are seen to be not detected by the PSD possibly due to them sticking to larger grains. Due to this a separate study was done which investigated the effect of different amounts of these nano-fragments on the performance on the composite by varying the amount of times ball-milling was done during production of the ceramic. This is described in [Section-4.5](#).

Hence, in-order to quantitatively describe the trends in  $d_{33}$  noticed for these samples mentioned, an accurate measurement of porosities/interparticle distances present in a sintered agglomerate must be conducted however, this was not done due to a lack of time. Additionally, to investigate the effects of the thickness of the composite on the performance (since an uncontrollable increase in thickness could be the cause of a spike in the  $d_{33}$  as described for the  $C_1 = 950\text{ }^\circ\text{C}$ -1 h sample), a contact-less poling method known as corona poling was done on the samples (where poling process is independent of the thickness of the composite) and the performances were compared between each sample. This is described in [Section-4.9](#).

## 4.5 Ball-milling analysis

In order to analyse the effect of ball-milling and consequently the nano-fragments generated on the microstructure and  $d_{33}$ , a batch of powder was made with  $C_1 = 1050\text{ }^\circ\text{C}$ -1 h with  $C_2$  ( $925\text{ }^\circ\text{C}$ -10 h) kept the same as the previous experiments. This batch of powder was separated into several portions that each received different scenarios of ball milling. Three samples were prepared based on three ball-milling scenarios: (1) No ball-milling after both  $C_1$  and  $C_2$ ; (2) Ball-milled once after  $C_1$  and (3) Ball-milled after both  $C_1$  and  $C_2$ . The description of the samples are given in [Appendix-B4](#).

The batch of powder visualized under different stages of calcination and ball-milling are shown with 5000x magnification in [Figure 69](#) for viewing the grains and with 50x magnification in [Figure 70](#) for viewing the sintered agglomerates. The different stages and the corresponding images of the sample under the different magnifications are described as follows: (a) Main batch of powder after  $C_1$ ; (b) sample in (a) after  $C_2$ ; (c) sample in (a) after ball-milling; (d) sample in (c) after  $C_2$  and (e) sample in (d) after ball-milling

From the SEM images, it can be seen that the sample which was not ball-milled at all produced almost cubic grains with hardly any nano-fragments present after  $C_1$  (shown in [Figure 69 \(a\)](#)) and  $C_2$  ([Figure 69 \(b\)](#)). There is also a clear indication of unhindered grain growth happening during each calcination as the grain size increases after  $C_2$  compared to  $C_1$ .

When the sample is ball-milled after  $C_1$ , there is a complete destruction of the sintered microstructure producing a mixture of nano-fragments, broken grains and fully formed grains due to the ball-milling as seen in [Figure 69 \(c\)](#). After performing  $C_2$  on this sample, all the grains are seen to be regrown into fully formed grains due to sintering albeit with a lot more variation in the grain sizes as seen in [Figure 69 \(d\)](#). When this sample is now ball-milled again



after  $C_2$ , there is a complete destruction of the grain structures, just like the powder seen after the previous ball-milling as shown in Figure 69 (e).

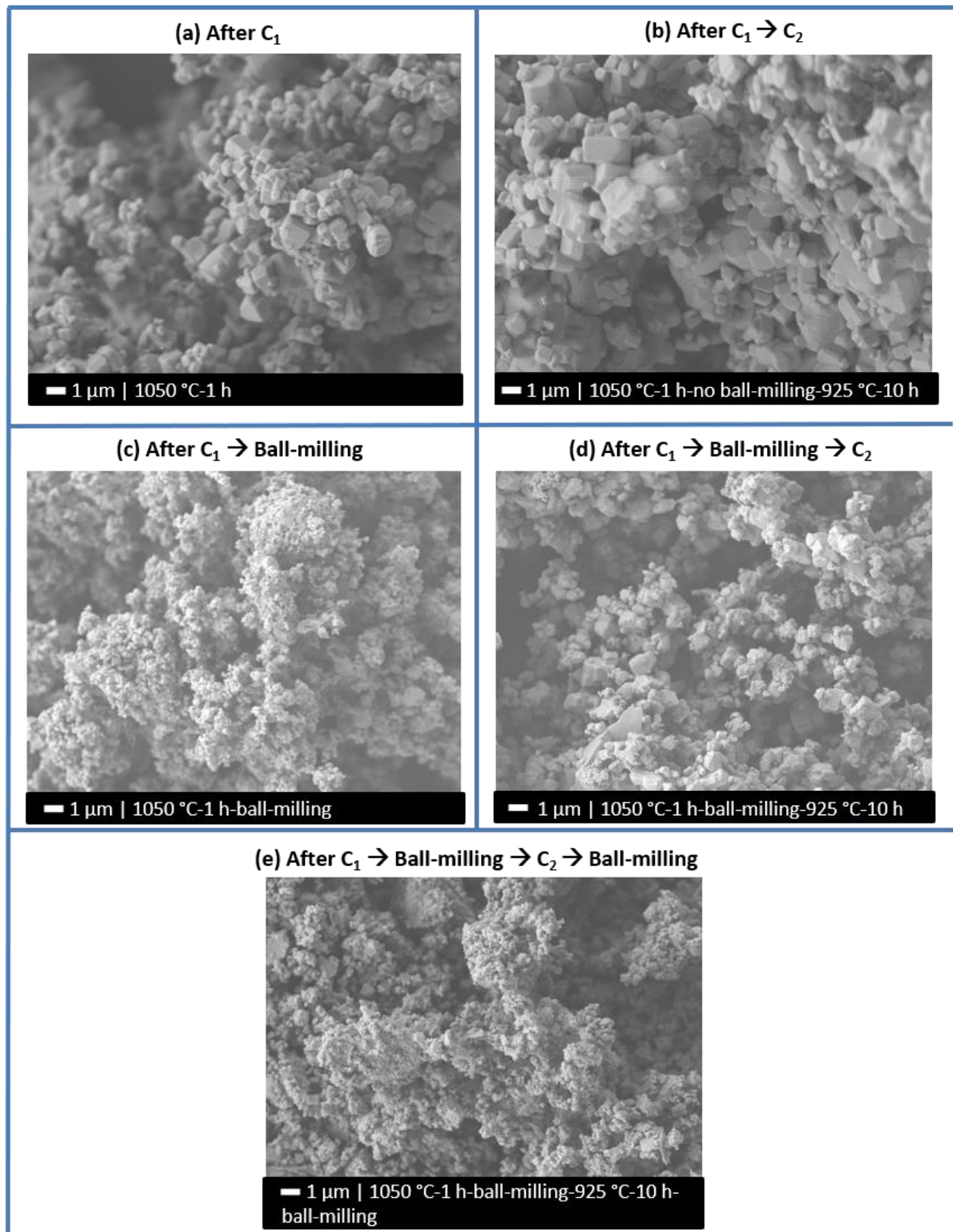


Figure 69: SEM images of the microstructure with 5000x magnification at different instances in the processing route of the ceramic: (a) After  $C_1$  of precursors, before any ball milling; (b) After  $C_2$  with no ball-milling done on sample in (a); (c) After ball-milling performed on sample in (a); (d) Sample from (c) after  $C_2$ ; and (e) After ball-milling performed on sample in (d)

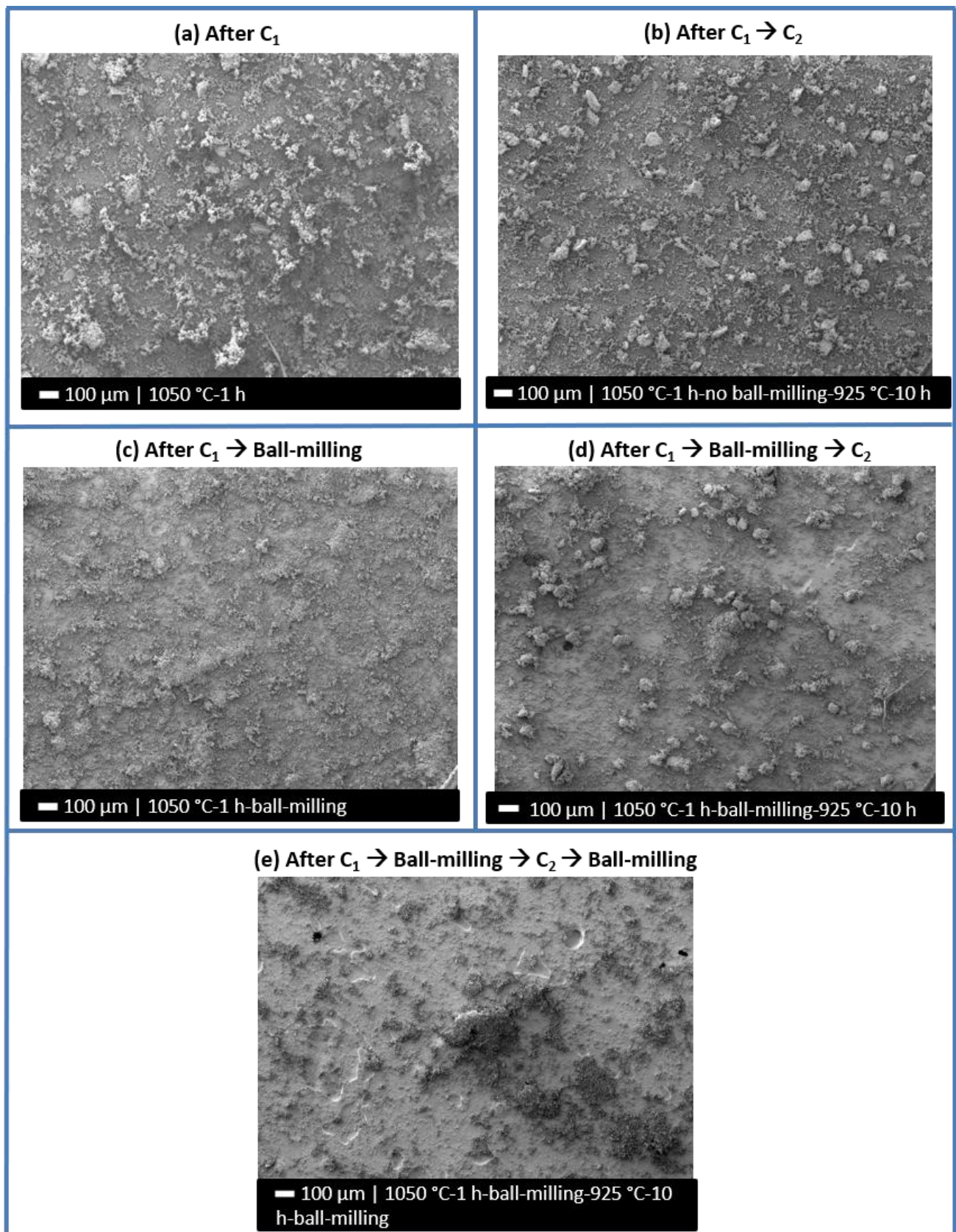
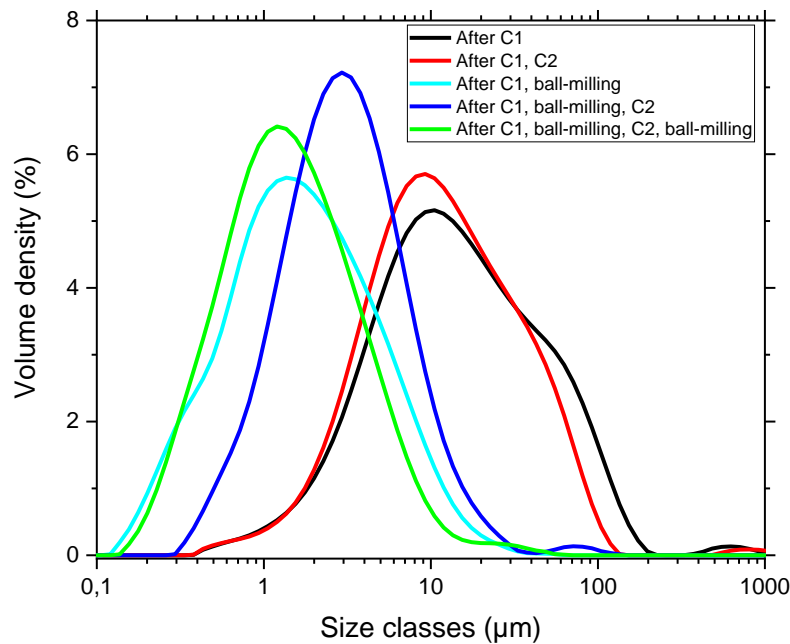


Figure 70: SEM images of the sintered agglomerates with 50x magnification at different instances in the processing route of the ceramic: (a) After  $C_1$  of precursors, before any ball milling; (b) After  $C_2$  with no ball-milling done on sample in (a); (c) After ball-milling performed on sample in (a); (d) Sample from (c) after  $C_2$  and (e) After ball-milling performed on sample in (d)



The same trend in the grains through the different calcinations and ball-milling scenarios can also be observed with the sintered agglomerates seen in Figure 70. The initial powder after  $C_1$  has a moderate amount of sintered agglomerates seen in Figure 70 (a). When this sample is calcined again the agglomerates grow to a bigger size and also more number of agglomerates are formed as seen Figure 70 (b) due to sintering. When the initial powder after  $C_1$  is ball-milled, there are no agglomerates remaining due to their breakage during ball-milling as seen Figure 70 (c). When this sample is calcined again, the agglomerates are formed again but they are lesser in numbers than the sample that was calcined directly after  $C_1$  due to the ball-milling which broke most of them as seen in Figure 70 (d). When this sample is ball-milled a second time, there is again complete breakage of the formed agglomerates (only agglomerates formed due to static agglomeration seen) as seen in Figure 70 (e).

PSD was performed on the sample after each calcination and ball-milling process to get quantitative information on the size of the grains and agglomerates after each process. It was also done to check whether the nano-fragments are detected in PSD under high amounts which is the case after each ball-milling scenario. The PSD curves and the variation of the ' $D_x$ ' parameters for the sample after each calcination and ball-milling process is shown in Figure 71 and Figure 72 respectively.



**Figure 71: Volume density (%) vs size classes (μm) of particles present in the sample after each calcination and ball-milling process**

From the PSD curves seen in Figure 71, it can be seen that the sample directly after  $C_1$  and after  $C_1$ ,  $C_2$  with no ball-milling in-between produce broad peaks with particles ranging from 0.4-200 μm in size. The samples also have a slight bimodal distribution compared to the other samples. The sample after  $C_1$ ,  $C_2$  with a ball-milling step in-between produces a very tight distribution in the particles with a unimodal distribution around 7 μm. The samples analyzed directly after the ball-milling following the calcinations also produce a unimodal and tight distribution of particles albeit with the peak situated at lower particles sizes  $\approx 1$  μm.

The high particle sizes and slight bimodal nature of the samples after each calcination without ball-milling is expected since there is no ball-milling step that breaks up the agglomerates formed that are typically in the  $\approx 100$  μm range.

Thus, there is almost an unhindered growth of the agglomerates and grains which yields a broad distribution of particles. The sample after  $C_1$ ,  $C_2$  but with a ball-milling step in-between produces a tight distribution of particles due to the breaking of the agglomerates and grains by the ball-milling step balanced with the energy left in the powder to regrow the particles present during  $C_2$ . The samples directly analyzed after each ball-milling step following the calcinations are seen to have peaks at lower particle sizes owing to the breakage of the microstructure during ball-milling. They are also seen to contain mostly nano-fragments in their powders as shown in Figure 69. However, the majority of the particles are seen to occupy a particle size of  $\approx 1 \mu\text{m}$  which meant that the nano-fragments are again not detected with the PSD even under high concentrations due to them sticking to bigger grains as seen in Section-4.4.2.

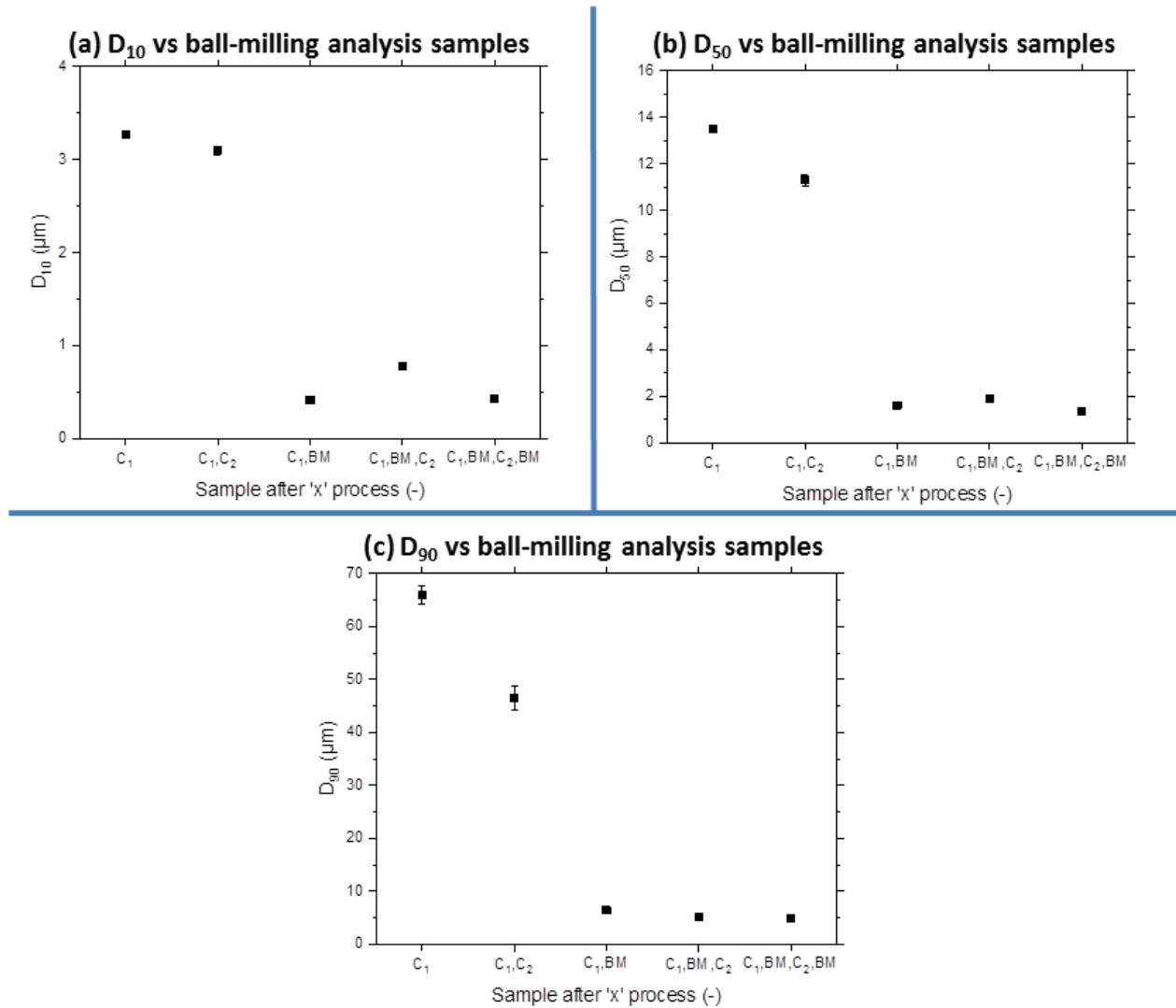


**Figure 72: (a)  $D_{10}$ , (b)  $D_{50}$ , and (c)  $D_{90}$  vs the sample after 'x' process (BM: ball-milling)**

From the results of the ' $D_x$ ' variation vs the sample after each calcination and ball-milling shown in Figure 72, it can be seen that the samples analyzed after  $C_1$  and  $C_1$ ,  $C_2$  with no ball-milling step in-between have the largest  $D_x$  parameters. This is due to the unhindered growth and grains and agglomerates owing to the lack of a ball-milling step as mentioned before. The latter sample has a lower  $D_{90}$  owing to the hand-milling step which partially broke up the agglomerates. The other samples namely: 'After  $C_1$ , ball-milling'; 'After  $C_1$ , ball-milling', ' $C_2$  and After  $C_1$ , ball-milling,  $C_2$ , ball-milling' have low and almost equal values for the  $D_x$  parameters owing to the ball-milling step which

breaks the agglomerates and grains. The sample after  $C_1$ , ball-milling,  $C_2$  shows a higher  $D_{10}$  than the other two samples owing to grain growth during  $C_2$ .

The results of the samples in-terms of the  $d_{33}$  vs average  $W_a$  is shown in Figure 73. From Figure 73, it is clearly seen that the unball-milled sample had the highest  $d_{33}$ . This could be due to the lack of nano-fragments present and the high number of agglomerates present in the sample which decreased the interparticle distances thus, aiding poling. The sample which had been ball-milled once had a similar  $d_{33}$  but with a higher amount of variation in  $d_{33}$  owing to the higher variation of grain and agglomerate sizes present. The similarity in  $d_{33}$  with the unball-milled sample could be due to the tighter particle size distribution creating a higher thickness thus, increasing the  $d_{33}$  as explained in Section-4.4.2.

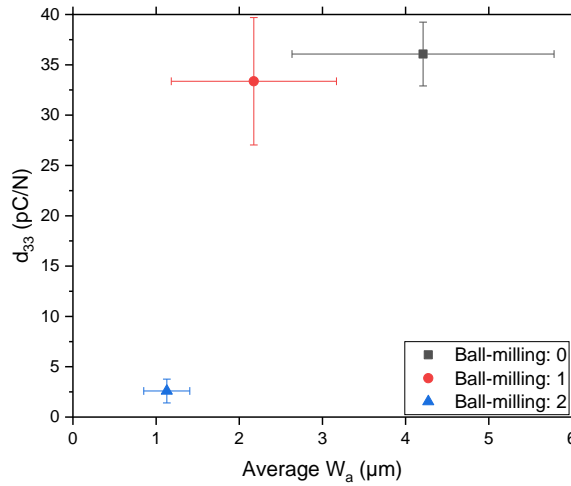


**Figure 73:  $d_{33}$  vs average  $W_a$  for the samples prepared with different amounts of ball-milling**

The sample which had been ball-milled twice showed a complete degradation in the  $d_{33}$  value by about 30 pC/N compared to the previous two samples. This could be attributed to either excessive number of nano-fragments present which meant that these fragments are non-piezoelectric or it could be the general lack of agglomerates produced which are essential to improve  $d_{33}$  as seen in Section-4.1 or a combination of both. The lowered  $d_{33}$  is observed despite a tight distribution in the particles which confirms the effect of the nano-fragments in decreasing  $d_{33}$ . This also could be why the higher  $C_1$  temperature samples in Section-4.2 had a lower  $d_{33}$  despite having a tight distribution of particles. As almost all the particles were seen to be nano-fragments, the variation in  $d_{33}$  is also very low. The exact reason for the lack of piezoelectricity in these fragments could be attributed to a high number of defects formed in the crystal lattices during the breaking of the grains thus, destroying the piezoelectricity due to a reduction in the polarisable volume. It could also be because of a decrease in the domain wall density as the size of the grains reaches nano-dimensions that makes it difficult to pole the ceramic. Raman/FTIR and TEM can be used to investigate into these phenomena respectively but these were not done due to lack of time.

From Figure 73, it can be seen that the unball-milled sample has the highest average  $W_a$  which corresponded to 4.5  $\mu\text{m}$ . This was due to the lack of ball-milling in its preparation which ensured the agglomerates were not broken. Thus, the growth of the agglomerates in this sample was undisturbed which gave the high average  $W_a$ . As the number of ball-milling scenarios increased, the average  $W_a$  decreased for the same reason. However, no short-circuiting was seen in any sample as none of them had excessive surface waviness ( $>15 \mu\text{m}$ ) as seen in the highly agglomerated samples in Section-4.1, since the agglomerate sizes for all the samples were restricted by the mesh sizes of the sieves

used during sieving. Given the small variation in the  $d_{33}$  of the single ball milling and unmilled powder it was decided to continue to use the powder with the single ball-milling as the preparation of this powder requires less time and man-power, making it more scalable (due to hand-milling being less scalable than ball-milling). Thus, the sample ball-milled once represents an optimized sample in-terms of microstructure, number of nano-particles present, performance and surface waviness.

To conclude there seems to be a trade-off between the tightness of particle size distribution (which produces a higher thickness and consequently a higher  $d_{33}$ ), agglomerates formed (higher agglomerate sizes seem to increase  $d_{33}$ ) and the nano-fragments produced (which seems to decrease  $d_{33}$ ). The tightness of the particle size distribution and the agglomerates formed seem to depend on the effectiveness of the breakage of the agglomerates and grains during ball-milling balanced with the energy left for grain growth and sintering in subsequent calcinations. The nano-fragments depend on the ball-milling step and the size of grains and agglomerates formed after  $C_1$ .

## 4.6 Agglomeration variation analysis

Based on the results from the other tests presented in [Section-4.2](#), [Section-4.3](#) and [Section-4.4](#), ceramic powder with calcination route:  $C_1=950\text{ }^{\circ}\text{C}$ -3 hours,  $C_2=925\text{ }^{\circ}\text{C}$ -10 hours was seen to be the best performing as a composite. Hence, a more elaborate agglomeration variation test was performed on this powder with agglomeration sizes (corresponding to the mesh size of sieves used) ranging from:  $>125\text{ }\mu\text{m}$ ,  $90\text{-}125\text{ }\mu\text{m}$ ,  $63\text{-}90\text{ }\mu\text{m}$ ,  $25\text{-}63\text{ }\mu\text{m}$ ,  $<25\text{ }\mu\text{m}$ . This was done to properly optimize the amount of agglomeration present in the sample with the acquired  $d_{33}$  and surface waviness (which is directly related to the short-circuiting within the samples). The performance of these powders with respect to their agglomeration sizes is presented in Figure 74. The description of each of the powders used in the analysis is given in [Appendix-B5](#).

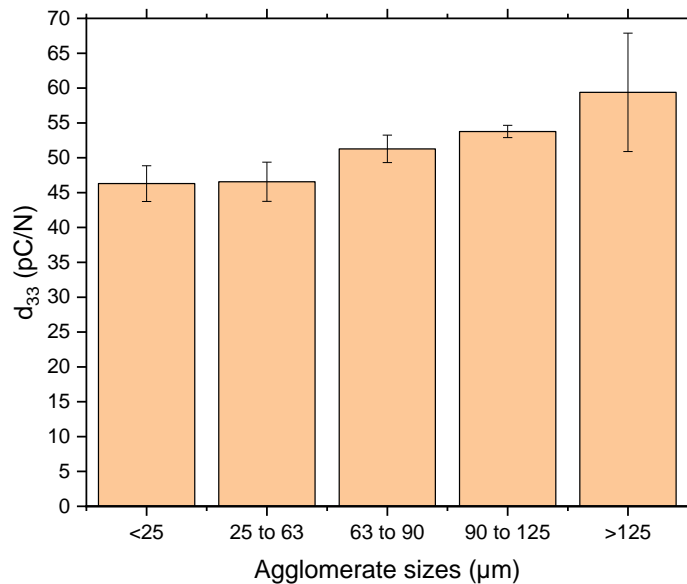


**Figure 74: Variation of  $d_{33}$  with respect to the agglomerate size present in the powder**

From Figure 74, it can be seen that the  $d_{33}$  peaks at about 60 pC/N for the  $>125\text{ }\mu\text{m}$  agglomerate size sample and decreases steadily as the agglomerate size decreases. The high  $d_{33}$  can be due to the pseudo 1-3 composite effect. This is because the bigger size of agglomerates yields a higher connectivity that mimicks 1-3 composites which pole much more efficiently compared to 0-3 composites, as was seen in [Section-4.1.2](#). The composite becomes

predominantly a 0-3 composite from an agglomerate size of 25-63  $\mu\text{m}$  and lower, which is seen by the  $d_{33}$  stabilising for these samples.

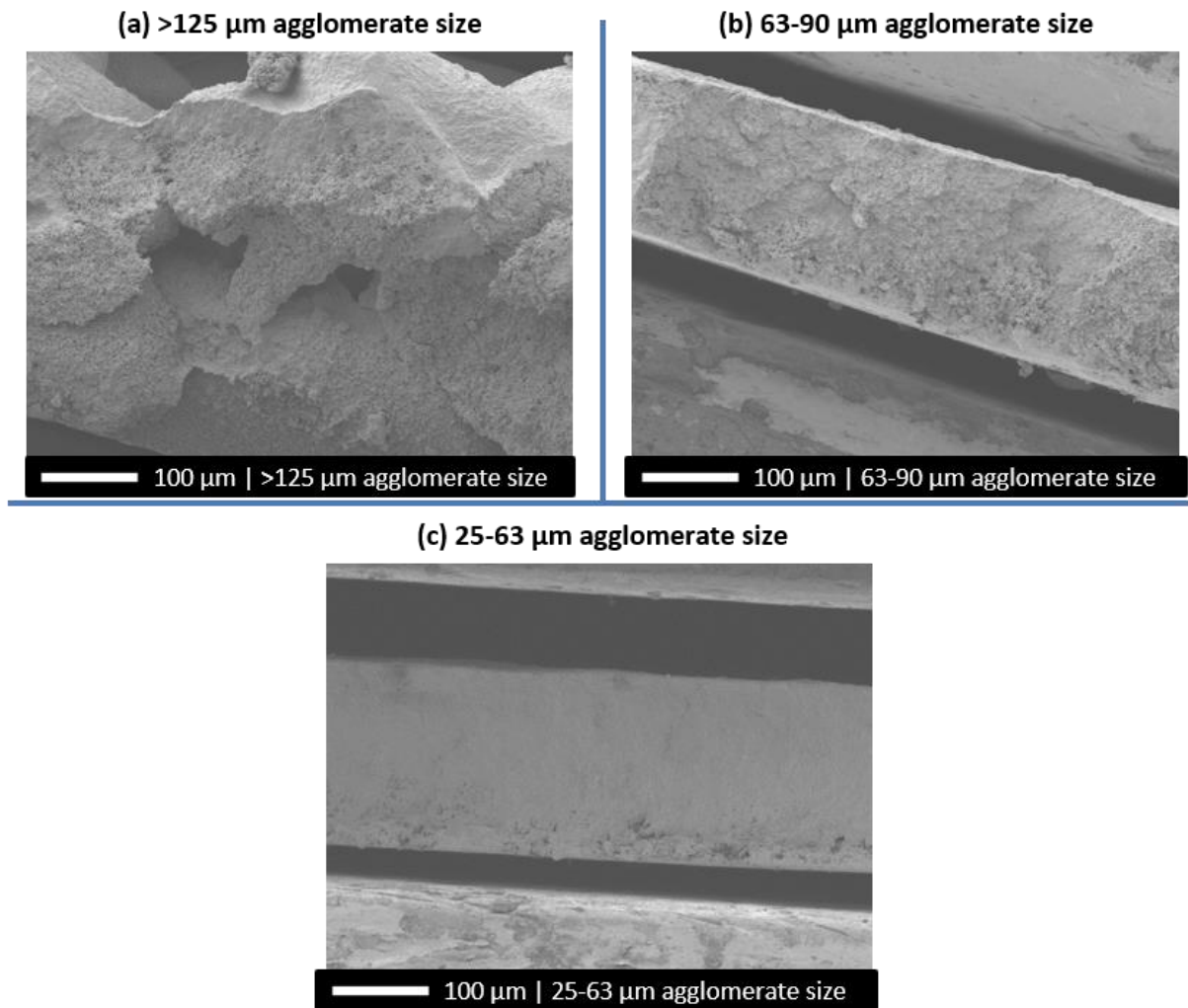


Figure 75: Cross-sectional images from SEM (200x magnification) of the >125  $\mu\text{m}$  (a); 63-90  $\mu\text{m}$  (b) and 25-63  $\mu\text{m}$  (c) agglomerate size samples

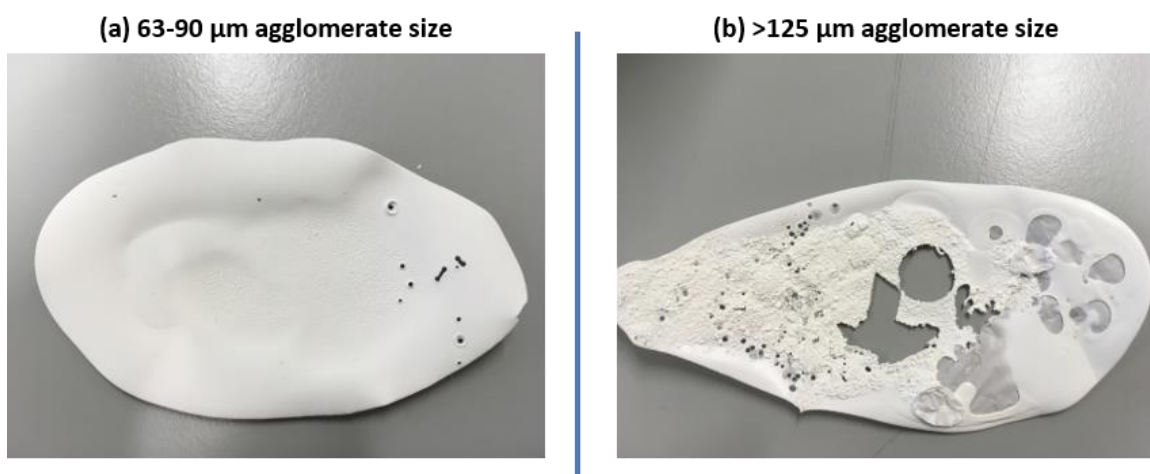


Figure 76: Composite samples made with (a) 63-90  $\mu\text{m}$  and (b) >125  $\mu\text{m}$  agglomerate size ceramic powders

The interconnectivity present in the composite can be clearly seen in SEM images of the cross sections in Figure 75, where there is a decrease in the size of the agglomerates yielding less interconnectivity as we go from  $>125\ \mu\text{m}$  (Figure 75 (a)) to  $63\text{--}90\ \mu\text{m}$  (Figure 75 (b)) to  $25\text{--}63\ \mu\text{m}$  (Figure 75 (c)) agglomerate size samples. Additionally, there is a high variation in the  $d_{33}$  of the  $>125\ \mu\text{m}$  agglomerate size sample. This was due to the inhomogeneity created within the composite during casting caused by the large size of the agglomerates present. The composite is shown alongside the  $63\text{--}90\ \mu\text{m}$  agglomerate size sample for comparison in Figure 76. The SEM images of the same top surfaces of the two samples is shown in Figure 77 at  $50\times$  magnification which again shows the inhomogeneity present in the  $>125\ \mu\text{m}$  agglomerate size sample at a microscopic level compared to the  $63\text{--}90\ \mu\text{m}$  agglomerate size sample.

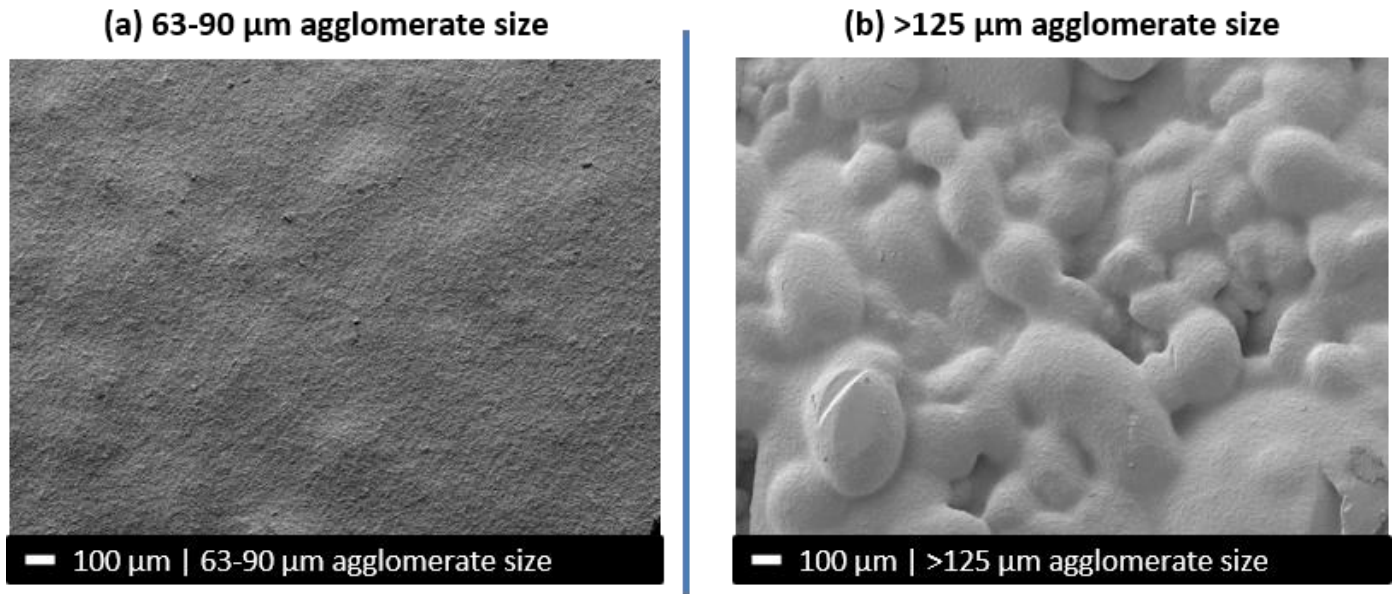


Figure 77: Top surfaces of (a)  $63\text{--}90\ \mu\text{m}$  and (b)  $>125\ \mu\text{m}$  agglomerate size sample when viewed in SEM at  $50\times$  magnification

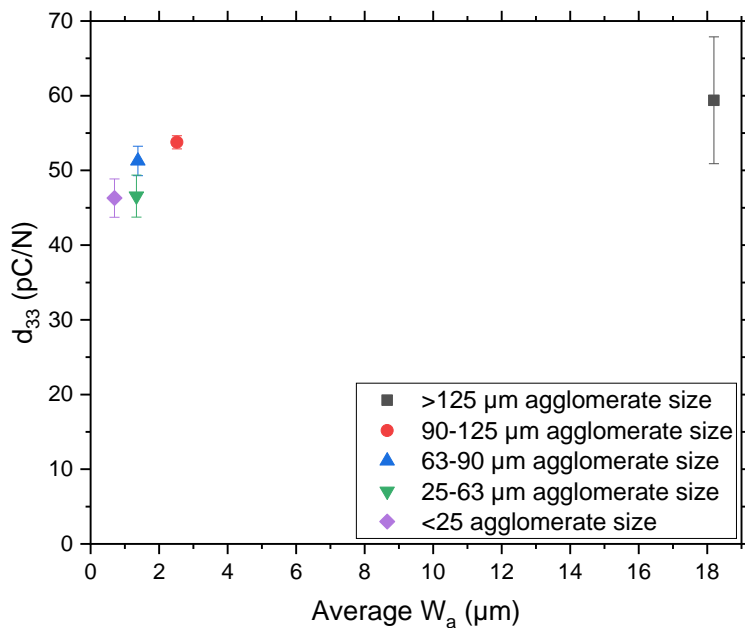
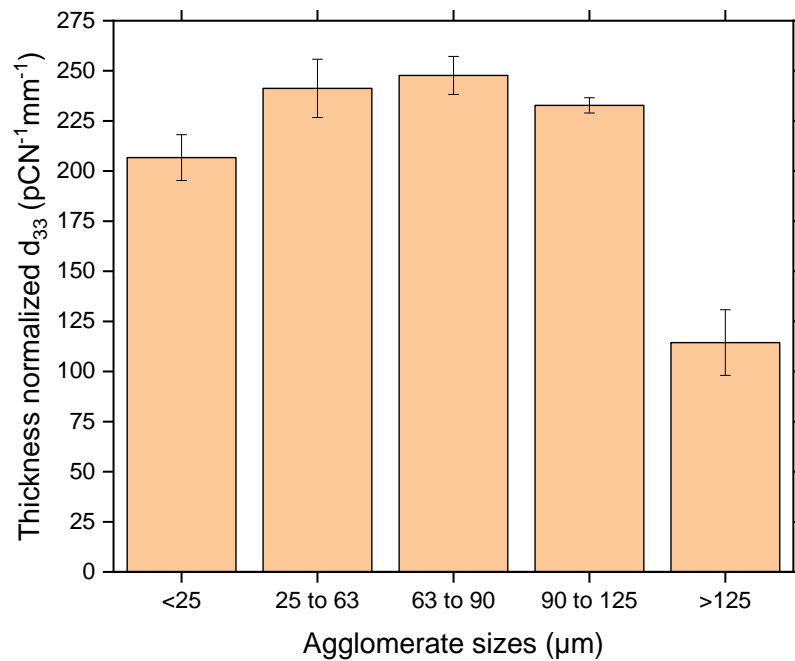


Figure 78:  $d_{33}$  vs average  $W_a$  for the agglomerate sizes present in the sample

The average  $W_a$  of all the samples with respect to their  $d_{33}$  is shown in Figure 78. Although, there is a decreasing trend in the average  $W_a$  of the samples with decreasing agglomerate size, the average  $W_a$  for the  $>125\ \mu\text{m}$  agglomerate size sample is about  $18\ \mu\text{m}$ , which is well above the next biggest sample of about  $3.5\ \mu\text{m}$ . The other samples have practically the same average  $W_a$  since all of their values are around  $0.5$  to  $3.5\ \mu\text{m}$ .

The high average  $W_a$  of the composite made from  $>125\ \mu\text{m}$  particles does not form a smooth surface on the top as seen in Figure 77. Given that the thickness of the composites is typically in the range of  $100$ - $200\ \mu\text{m}$ , it is unsurprising that the biggest sizes of the agglomerates do not pack efficiently thus, creating exceptionally high average  $W_a$ . This created a high number of short-circuits in the sample during poling and hindered the formation of good quality electrodes.



**Figure 79:  $d_{33}$  normalized with the thickness of the composites vs the agglomerate sizes present in the ceramic**

Although,  $>125\ \mu\text{m}$  agglomerate size sample showed the highest  $d_{33}$ , it had various other disadvantages associated with it as explained before. Apart from these, it was also seen that the thicknesses of the composite were not the same due to the large variation in the size of agglomerates between the samples. Thus, in-order for a fair comparison of  $d_{33}$  between the samples, the  $d_{33}$  must be normalized by the thickness. This is because the thickness of the composite plays a vital role in determining the  $d_{33}$  of the composite as previous work done on PZT ceramics suggest that the  $d_{33}$  scales with the thickness of the composite due to non-linear additions to the  $d_{33}$  measurement by other  $d_{ij}$  modes [117]. This gives an incorrect reading of the  $d_{33}$  due to the thickness as seen previously with the calcination study samples in Section-4.4. The  $d_{33}$  results of all the samples normalized by the thickness is shown in Figure 79. From the results, it is clearly seen that the  $63$ - $90\ \mu\text{m}$  agglomerate size sample performs the best in-terms of  $d_{33}$  compared to the other samples.

Based on the results, the  $63$ - $90\ \mu\text{m}$  agglomerate size is seen to be the optimal agglomerate size for composites as not only does it yield a good  $d_{33}$  that is close to the sample which has the highest agglomeration, but it also has a very smooth surface yielding less short-circuiting that is ideal for poling and the final end performance.



## 4.7 Composite synthesis method analysis

While solution casting provides good results, the solvents that are typically required to solution cast the CFE matrix (DMF, THF or DEP) are highly toxic and undesirable to use on a large industrial scale. Additionally, usage of solvents implies that there will be solvent evaporation in the samples thus, giving rise to porosities within the sample that decreases the density and the  $d_{33}$ . Therefore, in order to determine if it is possible to remove these solvents, hot-pressing was carried out as a potential solvent-less synthesis method. The KNLN-3 powder used was prepared with the calcination route:  $C_1=1050\text{ }^{\circ}\text{C}$ -1 hour;  $C_2=925\text{ }^{\circ}\text{C}$ -10 hours. For comparison of the performances between the solution-casting and hot-pressing methods, R40 composites were produced in both cases since R50 composites were not possible to produce with hot-pressing due to the high viscosities observed for the ceramic-polymer mixture during extrusion. Additionally, the surface wavinesses were also compared to analyse whether the hot-pressed sample would have comparable surface waviness to the previously used solution-cast samples. The solution cast and hot-pressed composite discs are shown in Figure 80 (left) and Figure 80 (right) respectively. The cross-sectional SEM images of the same set of composites are shown in Figure 81 (a) and Figure 81 (b) respectively.

It can be seen from Figure 80, that visibly there is no difference in the topology of the composite discs with both types of composite casting. There is a discolouration noticed in the hot-pressed sample compared to the solution cast sample. This was attributed to the slight decomposition/degradation of the CFE polymer due to the high temperatures. Size exclusion chromatography or other similar techniques could be used to see if the polymer molecular weight has changed but, as the composites remain robust and flexible and due to time constraints, this was not done.

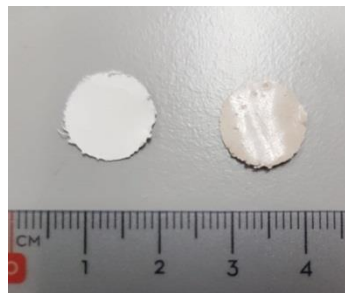


Figure 80: Solution cast (left) and hot-pressed (right) R40 composites of KNLN-3 and CFE

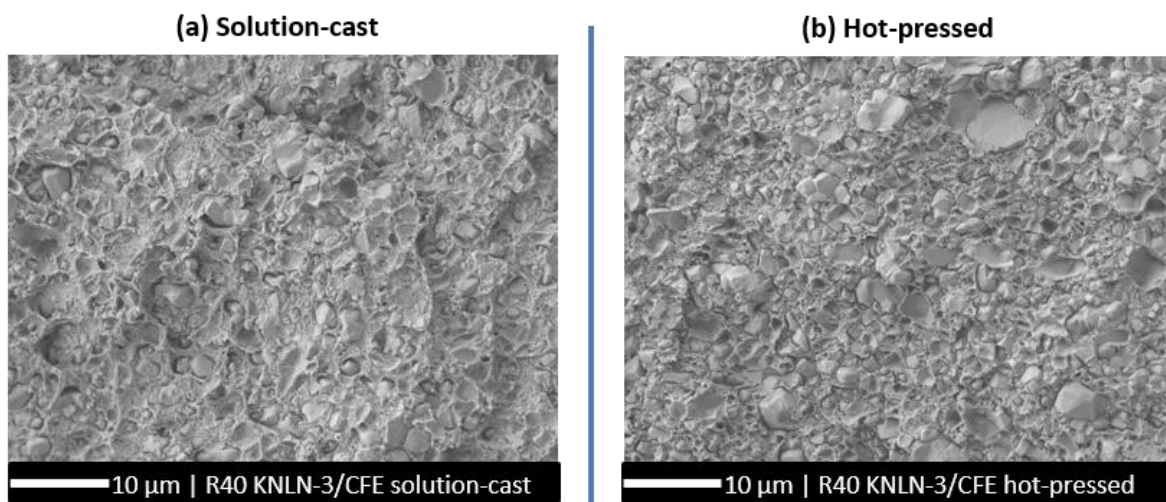
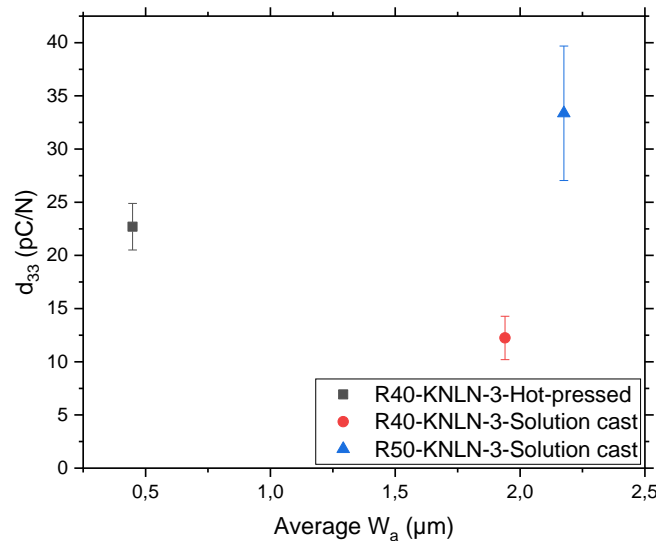


Figure 81: Cross-section images of the solution-cast (a) and hot-pressed (b) composite made with KNLN-3 ceramic as seen through SEM (2000x magnification)



Nevertheless, from Figure 81 (a) and Figure 81 (b), it can be seen that there is no change in the microstructure of the composite with both types of composite casting which suggests that the decomposition of the polymer may not affect the microstructure of the composite and that the polymer-ceramic interactions remain unchanged by hot pressing. This shows that the voids observed at the polymer-ceramic interfaces for the solution-cast sample (Figure 81 (a)) are not related to solvent evaporation but rather the poor ceramic-polymer interactions.

The results of the performance of the hot-pressed and the solution cast KNLN-3 composites against the surface waviness is given in Figure 82. Additionally, the R50 solution cast KNLN-3 composite is also shown for comparison.



**Figure 82:  $d_{33}$  vs average  $W_a$  for the hot-pressed and solution cast R40 KNLN-3/CFE composites compared with the solution cast R50 KNLN-3/CFE composite**

It can be seen from Figure 82, that the hot-pressed sample performs better than the solution cast variant by an order of 10 pC/N. The surface waviness of all the samples is less than 2  $\mu\text{m}$  owing to the lack of big sized agglomerates introduced during sieving.

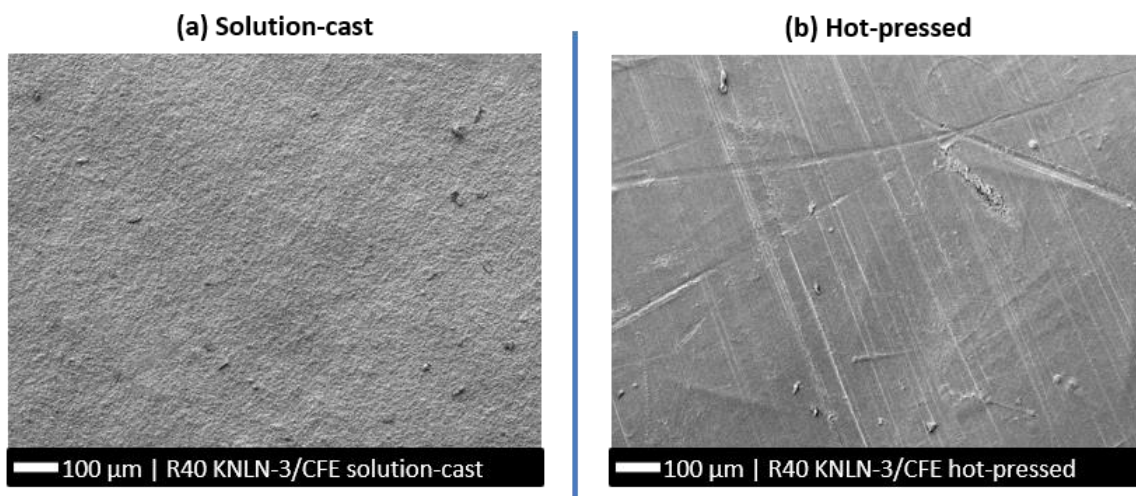


**Figure 83: Top surface of (a) solution-cast and (b) hot-pressed R40 composite samples viewed through SEM at 100x magnification**

This is also notably seen in the SEM images of the top surfaces of both the composites presented in Figure 83. From the images it is seen that both the composite surfaces are relatively smooth compared to the highly agglomerate samples presented in [Section-4.6](#).

Since the microstructure and surface topology were seen to be consistent in both samples, the higher performance of the hot-pressed sample can be solely due to no solvent evaporation taking place in it which creates no porosities in the sample. This improves the density and the overall properties present in the composite since the composite poles better (lesser porosities/higher density implies a higher dielectric constant). This is clearly seen when the  $d_{33}$  of the same samples are plotted against their relative densities in Figure 84. It is seen that the hot-pressed sample has a much higher relative density  $\approx 86\%$  compared to both the R40 and R50 solution cast samples which have a relative density  $\approx 80\%$ .

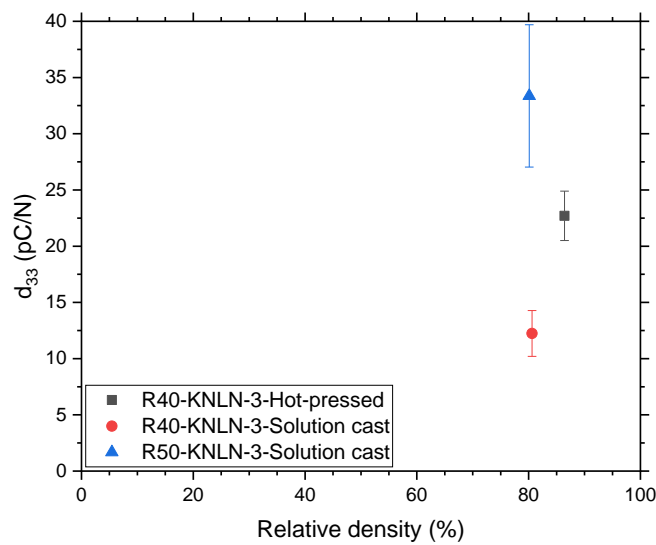


**Figure 84:  $d_{33}$  vs relative density of the R40 hot-pressed and R40, R50 solution-cast composite samples**

It is also seen that there is a dramatic drop in the  $d_{33}$  between the R50 and R40 solution cast composites due to the additional ceramic powder present in the R50 composite. The  $d_{33}$  of this composite also surpasses that of the R40 hot-pressed sample for the same reason. This is in agreement with previous work on random composites where a strong, non-linear, dependence of  $d_{33}$  on ceramic content is observed [118].

To conclude, the hot-pressing method has many benefits compared to its solution-cast counterpart due to the lack of a solvent needed during synthesis. However, additional investigation must be done on generating a lower viscosity during the extrusion stage of the hot-press synthesis such that R50 composites can be made that will potentially have a higher  $d_{33}$  than its solution-cast counterpart.

## 4.8 Precursor optimization

Due to the high price of highly pure (99.99 % trace-metals basis)  $\text{Nb}_2\text{O}_5$ , a short study was conducted to determine if a lower grade (99.9 % trace-metals basis)  $\text{Nb}_2\text{O}_5$  would provide the same properties. In this analysis, high purity (99.99 %) and a low purity (99.9 %)  $\text{Nb}_2\text{O}_5$  were used to make the KNLN-3 powder and then made into a composite with CFE. The two powders were tested for their phase purity and the composites were tested for their  $d_{33}$ . This was

done in hopes of potentially replacing the more pure niobium oxide with the less pure one, if the properties of both their powders and composites are the same which will dramatically reduce costs and aid in scale-up.

All KNLN-3 powders were made with calcination route:  $C_1=950\text{ }^{\circ}\text{C}$ -1 hour,  $C_2=925\text{ }^{\circ}\text{C}$ -10 hours. The phase purity of the KNLN-3 powders made with the both less and more pure  $\text{Nb}_2\text{O}_5$  were analysed in XRD. The comparison of the XRD patterns between the KNLN-3 powder made with the more pure and less pure  $\text{Nb}_2\text{O}_5$  is shown in Figure 85. From Figure 85, it can be seen that there is a shoulder in the (111) peak (indicated by solid black arrow) in the KNLN-3 made with less pure  $\text{Nb}_2\text{O}_5$  after  $C_1$ . This could be attributed to the presence of unreacted powder in the sample. The peaks become sharper, more intense and the shoulder under the (111) peak disappears after  $C_2$  for the same sample (indicated by dotted black arrow). There are also no secondary phases forming in any of the samples which usually occur at the  $25^{\circ}$  to  $30^{\circ}$  region.

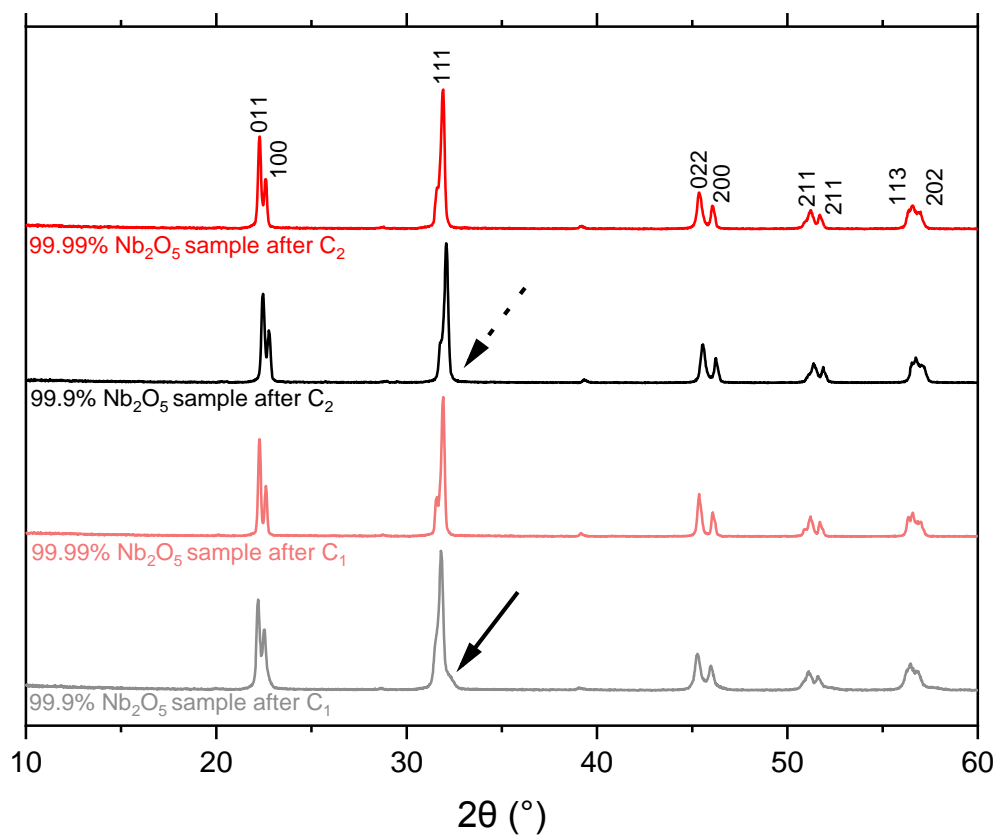


**Figure 85: XRD curves of the KNLN-3 powders made with less pure and more pure  $\text{Nb}_2\text{O}_5$  after  $C_1$  and  $C_2$**

The unreacted components present after  $C_1$  for the KNLN-3 made with less pure  $\text{Nb}_2\text{O}_5$  could be due to the precursors taking a longer time to react as the  $\text{Nb}_2\text{O}_5$  is less pure. After  $C_2$ , the samples with more pure and less pure  $\text{Nb}_2\text{O}_5$  seem to have the same composition with no changes in phase purity as the peaks are indistinguishable from each other.

The difference in the reaction rates between the more and less pure  $\text{Nb}_2\text{O}_5$  during  $C_1$  could also be due to the fact that the more pure  $\text{Nb}_2\text{O}_5$  is seen to have a more finely divided microstructure with distinct grains as seen in Figure 86 (a) compared to that of the less pure  $\text{Nb}_2\text{O}_5$  seen in Figure 86 (b) when visualized with SEM. This enables the more pure  $\text{Nb}_2\text{O}_5$  to have more surface area for contact with the other precursors yielding a faster reaction.

The comparison of  $d_{33}$  of the composites made from the KNLN-3 powders with less pure and more pure  $\text{Nb}_2\text{O}_5$  is shown in Figure 87. From Figure 87, it can be seen that the KNLN-3 made with less pure  $\text{Nb}_2\text{O}_5$  performs almost as well as its more pure counterpart, the difference being only 4 pC/N with strongly overlapping standard deviations. This could be attributed to sample to sample variation as there are no phase purity changes seen by either of the powders after  $\text{C}_2$  with XRD in Figure 85. Hence, the less pure form of  $\text{Nb}_2\text{O}_5$  is seen to be a satisfactory replacement for the more pure form in the making of the KNLN-3 powder and composite.

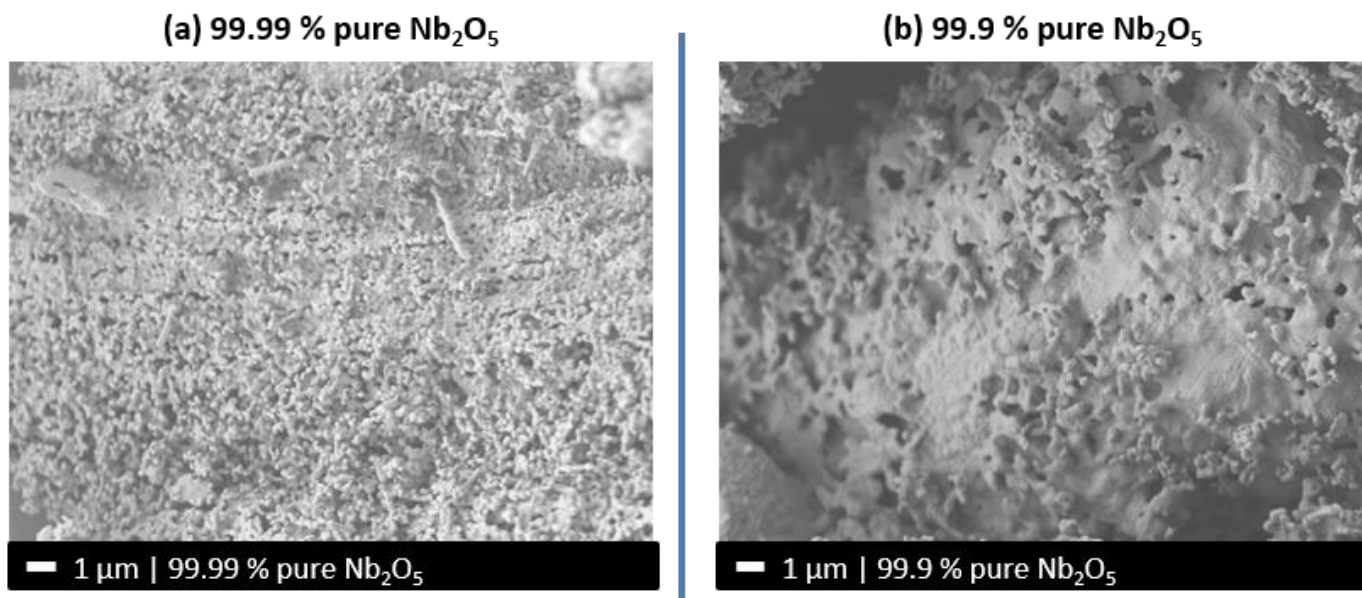


Figure 86: Microstructure of 99.99 % pure  $\text{Nb}_2\text{O}_5$  (a) and 99.9 % pure  $\text{Nb}_2\text{O}_5$  (b) visualized with SEM at 5000x magnification

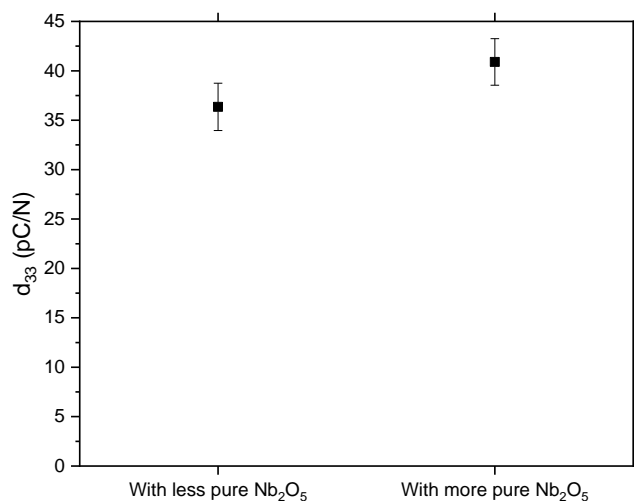
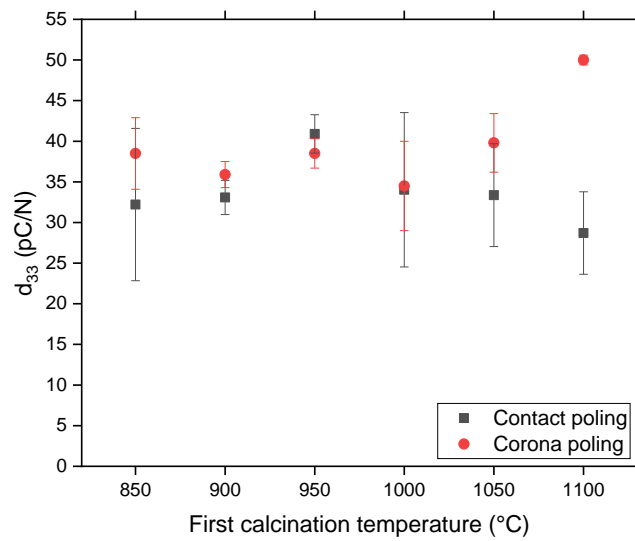


Figure 87:  $d_{33}$  vs the KNLN-3 samples made with less pure and more pure  $\text{Nb}_2\text{O}_5$

## 4.9 Poling method analysis

The poling process is influenced by several factors as explained in Section-2.4.2.2. One of these factors is the surface topology of the composites which may breakdown the electrode creating short-circuits with contact poling.

Additionally, it was also noticed through this study that the microstructure and thickness of composite are also influential to the poling process during contact poling. However, with poling methods like corona poling (a corona discharge is used to pole the composite without any contacts), the contact between the machine and the composite is eliminated thus, removing the influence of the factors mentioned before on the poling. An added benefit which comes with using corona poling is that the poling can be performed in the same production line as the composite production thus, decreasing production time which will aid in scale-up. Based on the comparison of  $d_{33}$  between corona poled and contact poled samples, an optimal poling method can be evaluated that will aid in scale-up. The samples that were poled with corona poling are described in [Appendix-B8](#). The agglomerated samples and dwelling time samples which were planned to be corona poled were not done due to lack of time with the corona poling set-up. However, most of the calcination temperature variation samples were poled with corona poling and their respective  $d_{33}$  plotted against the calcination temperatures are shown in Figure 88 for both the poling methods.



**Figure 88:  $d_{33}$  vs calcination temperature of samples poled with contact and corona poling**

From the results, it is seen that almost all of the corona poled samples perform the same when compared with their contact poling counterparts with strongly overlapping standard deviations. It is also noticed that the standard deviations are seen to be lesser in the corona poled samples compared to the contact poled samples. This is because, corona poling is insensitive to properties in the composite that influence contact poling such as surface topology and density. Thus, local changes in electric field due to surface waviness and porosities (generated by solvent evaporation) inside the composite are not influential during poling. Hence, we get a more consistent  $d_{33}$  value of the composite than in contact poling.

Additionally, we notice that most of the samples have a constant  $d_{33}$  value from  $C_1=850$  °C-1 h to the 950 °C-1 h samples and a peak is no longer seen in the latter. This is because corona poling is insensitive to the microstructure of the composites and hence, the tight distribution of the particles which were hypothesized to be contributing a better  $d_{33}$  (by indirectly increasing thickness) as described in [Section-4.4](#), no longer apply.

Furthermore, it is also noticed that the  $C_1=1050$  °C-1 h and 1100 °C-1 h samples possess higher  $d_{33}$  with corona poling than contact poling with the latter sample showing a drastic difference in  $d_{33}$  ( $\approx 20$  pC/N) between the two poling methods. This is again attributed to the insensitivity of corona poling to the microstructure as well as thickness of the ceramic filler present in the composite. This is clearly seen in Figure 89, when the contact poling results show the

same trend as the corona poling results with respect to  $d_{33}$  when normalized with their respective composite thicknesses. A clear increasing trend is noticed due to the lowered thickness of the composites.

To conclude, corona poling is a viable replacement for contact poling since the samples poled with corona poling have an equal or greater  $d_{33}$  compared to samples poled with contact poling and it eliminates factors like surface topology, thickness and microstructure of the composites which influence poling.

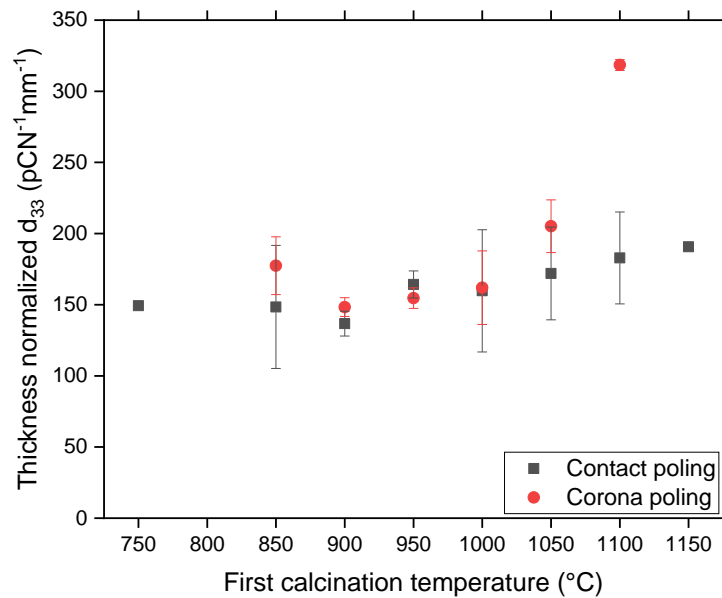


**Figure 89:  $d_{33}$  of the contact and corona poled samples vs their respective  $C_1$  temperatures after normalizing with composite thickness**

## 4.10 Mechanical testing

Tensile testing was done on samples with the best performing powder with calcination route:  $C_1=950$  °C-3 hours,  $C_2=925$  °C-10 hours. Tensile testing was done to calculate the stiffness of the ceramic composite under different ceramic loadings (0 % to 60 % vol. of filler) to determine the optimum ceramic loading that preserves flexibility whilst having a good amount of stiffness and piezoelectric properties. The samples used are described in [Appendix-B6](#).

### 4.10.1 Tensile testing

Tensile testing was done with the DMA apparatus due to the apparatus having a more sensitive load cell that can better quantify the smaller order of stresses that occur in polymeric samples than a larger, more dedicated tensile testing setup. The analysis was done at constant and ambient temperature. The stress vs strain curves and Young's modulus ( $E$ ) calculated from these curves of the different samples that were tested is shown in [Figure 90 \(a\)](#) and [Figure 90 \(b\)](#) respectively. The samples with added glass fibres were not done due to lack of time.

From [Figure 90 \(a\)](#), it can be seen that from 0 V% to 30 V% ceramic filler loading, the curves follow that of a typical polymer within an elastic region (where stress increases with strain) followed by a region where chain alignment of the polymer occurs (where stress is constant with strain, even above than 25 %). Hence, it can be said that from 0 V% to 30 V% ceramic filler loading, the samples are mostly dominated by the polymer which confirms their flexibility to be high. Conversely, the samples with higher than 30 V% ceramic filler loading start to show ceramic like properties



with the 60 V% ceramic filler loading sample showing almost a complete ceramic like behaviour and a corresponding increase in the Young's modulus in Figure 90 (b). This is also seen in the images captured with a camera fitted in the DMA apparatus for the 0 V% ceramic loading sample shown in Figure 91 (a) at the beginning of test and Figure 91 (b) at the end of the test compared to the same for the 60 V% ceramic loading samples shown in Figure 91 (c) at the beginning of test and Figure 91 (d) at the end of the test.

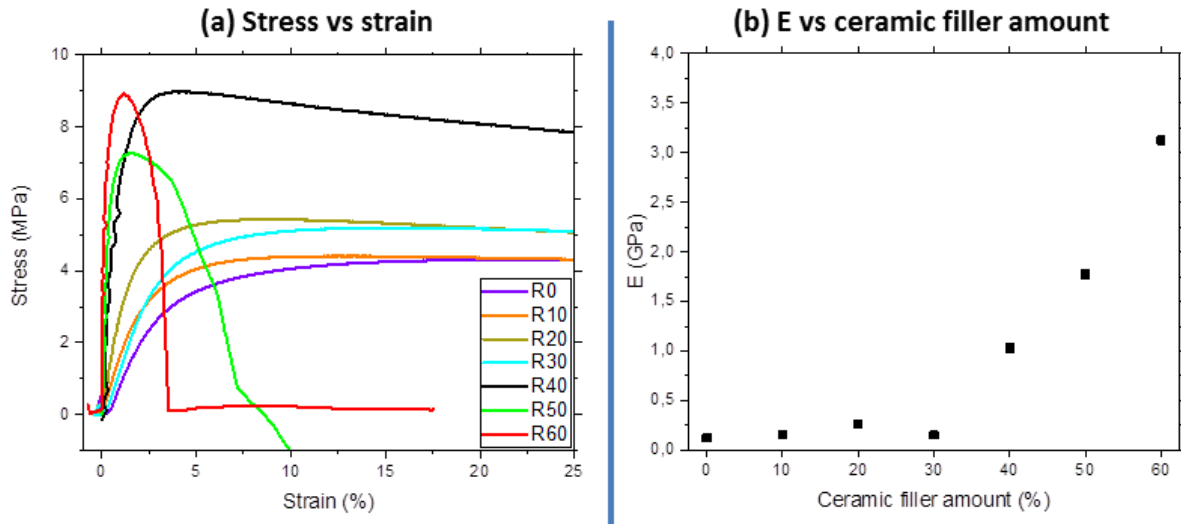


Figure 90: Stress vs strain curves (a) and Young's modulus vs ceramic filler amount (b) for all the samples tested in DMA

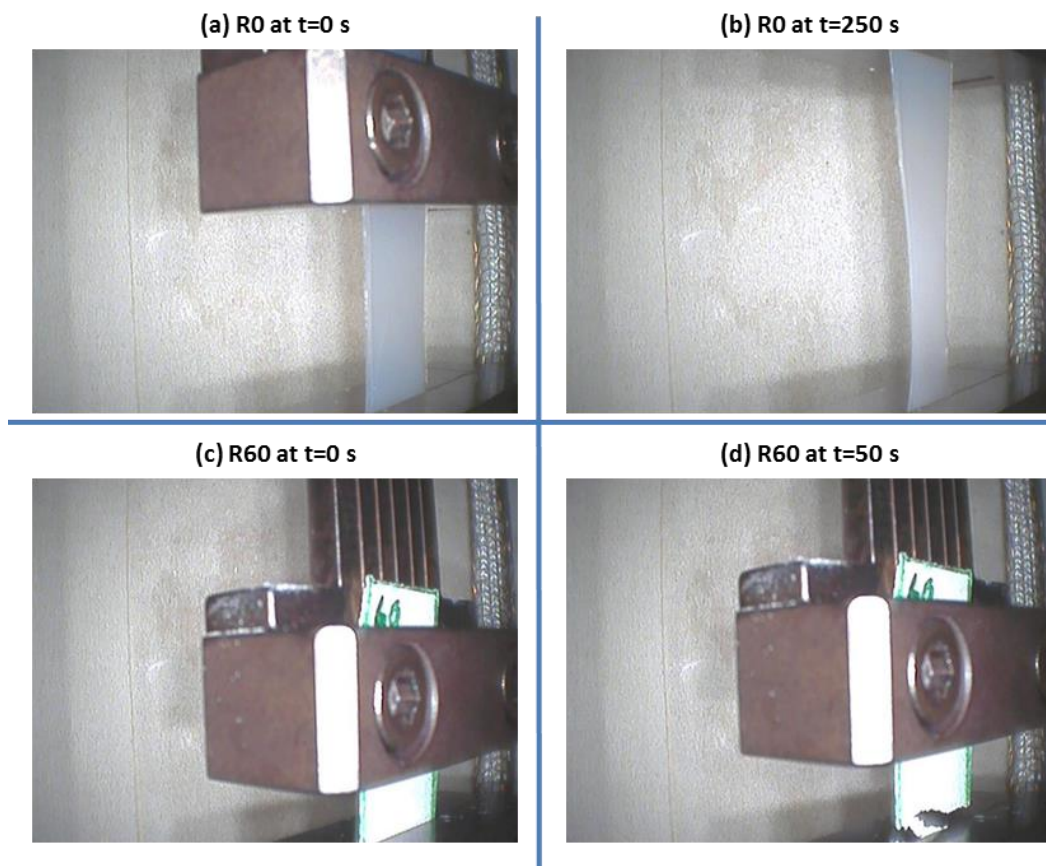


Figure 91: R0 sample at beginning of tensile test (a); R0 sample at end of tensile test (b); R60 sample at beginning of tensile test (c); R60 sample at end of tensile test (d)



The E for the lower loading samples is very low ([Figure 90 \(b\)](#)), with all samples having E less than 0.5 GPa due to their mechanical properties dominated by the polymer. Additionally, these samples also had a very low  $d_{33}$  as seen from previous work [65] which suggests that these ceramic filler loadings are not ideal for providing good haptic feedback. The 60 V% ceramic filler loading sample shows the highest amount of E which is expected out of a sample which has its mechanical properties dominated by the ceramic. However, due to its brittle nature seen in [Figure 91](#), it is also not the ideal ceramic filler loading as the composite is too fragile.

The 40 V% ceramic loading sample shows the ideal type of behavior expected out of simultaneously stiff and flexible materials because it has a high amount of stiffness (comparable to the 50 V% ceramic loading sample) of about 1.2 GPa whilst also displaying the polymeric chain alignment phenomenon mentioned before which confirms a higher level of flexibility compared to the 50 % ceramic loading sample which breaks at 10 % strain. However, from [Section-4.7](#), it is clearly seen that there is a dramatic difference in the  $d_{33}$  of the composite between the 40 % and 50 % ceramic loading with 50 V% ceramic loading showing a  $d_{33}$  that is 15 pC/N higher than the 40 V% ceramic loading. Hence, as the piezoelectric properties are currently the most important factor in determining composite quality, the 50 V% ceramic loading is chosen instead of the 40 V% as the optimum ceramic loading since the three parameters: flexibility, stiffness and piezoelectric properties are optimized in it.

#### 4.10.2 Torsional testing

Torsional testing was also done on the best performing KNLN-3 powder used in [Section-4.10.1](#), using a rheometer due to a smaller load cell. Torsional testing was done to calculate the stiffness of the composite samples made with the specified powder under different loadings, similar to tensile testing. In this test, the normal force ( $F_N$ ) was calculated upon a certain deformation that quantifies the stiffness of the composite. Additionally, 2 % (by weight of CFE polymer) glass fibres were added additional to the amount of polymer for each sample to investigate if the stiffness can be increased without changing the flexibility and piezoelectric properties. This is because a high stiffness may become necessary in the device development stage of this project and possible methods of addressing this will need to be determined without increasing the ceramic filler amount. The normal force of each ceramic filler loading sample with and without glass fibres is shown in [Figure 92](#).

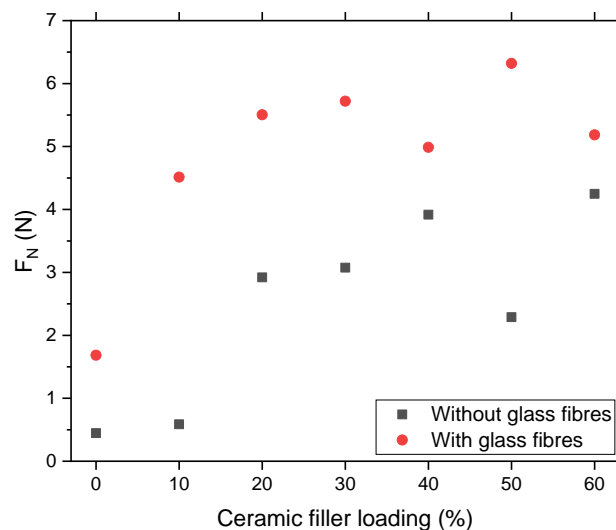


**Figure 92: Normal force vs ceramic filler loadings for all the mechanical testing samples taken with and without glass fibres**

From Figure 92, it is seen that with increase in the ceramic filler loading and the addition of glass-fibres there is generally an increase in the  $F_N$  for all samples. However, there are some exceptions to this such as the 50 V% ceramic filler loading sample which has a lower  $F_N$  compared to the 40 V% ceramic filler loading sample and in the 50 V% and 40 V% ceramic filler loading samples with added glass fibres which have an abnormally high and low value of  $F_N$  respectively. This could be attributed to sample to sample variations and inhomogeneity introduced by the inclusion of glass fibers respectively. More replications of this experiment would be required to confirm this but time constraints prevented further analysis.

It should be noted that typical force of a keystroke is in the range of 0.5 to 2 N for physical keyboards [119] and hence, all the samples are potentially viable user interfaces. Whether they can generate the required haptic feedback force is yet to be measured but they will ideally produce accelerations of approximately 5 – 10 m/s. However, only the 40 V%, 50 V% and 60 V% ceramic filler loading samples are practically relevant due to their superior piezoelectric properties. Amongst these, the 50 V% ceramic filler loading is chosen to be the optimum since it preserves a reasonable flexibility compared to its 60 V% counterpart whilst also having drastically better piezoelectric properties than its 40 V% counterpart.



**Figure 93: 0% ceramic filler loading sample without (a) and with (b) glass fibres**

Additionally, in the chosen ceramic filler loading, the sample without glass fibres is taken as the optimum because addition of glass fibres made the samples very brittle and visibly heterogenous as the glass fibres did not dissolve in the DMF even at the maximum mixing speed. This is seen clearly for the 0 V% ceramic filler loading samples without and with glass fibres in Figure 93 (a) and Figure 93 (b) respectively.

# 5 Conclusions and future work

## 5.1 Conclusions

This study presents optimized production processes for scaling-up the production of KNLN-3 ceramic powder used in flexible haptic feedback devices as piezocomposites in combination with CFE polymer. The study also presents a brief mechanical testing of the composites produced with the optimized powder, in-order to quantify parameters which are relevant when considering the haptic feedback. The relevant conclusions for each of the optimization processes and mechanical testing conducted is presented in the subsequent sections.

### 5.1.1 Study of poling conditions, agglomerate size and Li content

From the study on poling conditions, it was found that there is an optimum for poling conditions which was seen to be 10 kV/mm for 10 minutes or 5 kV/mm for 20 minutes. Higher poling voltages and times created short-circuits while vice-versa produced little to no poling. From the study on agglomerate size, it was seen that higher agglomerate sized samples performed better than lower agglomerate sizes samples however, the higher agglomerate sizes also had more short-circuits due to a high surface waviness. From the study on Li-content, the KNLN-6 and KNLN-3 ceramics performed equally in a composite under all agglomerate sizes due to the dielectric mismatch balancing with the powder piezoelectric performance and agglomerate numbers.

### 5.1.2 Calcination study

From the calcination study, through XRD and DSC, it was seen that their phase purity remained unchanged in all of the samples (no visible alkali evaporation was noticed in any of the samples) and the reaction to produce KNLN-3 powder was completed for all powders after  $C_2$ . For higher temperature samples, peak broadening was noticed which could be due to nano-fragments, oxygen vacancies or undetectable Na or K evaporation from surface being present. The nano-fragments were confirmed to be present via SEM images but the latter two are yet to be investigated. A  $C_1$  temperature of 950 °C and  $C_1$  dwelling time of 3 hours were seen to yield the best performance. Additionally, the surface waviness was low and practically constant amongst the samples due to the same size of sieves used which aided poling as no samples short-circuited.

### 5.1.3 Microstructure analysis

From the ceramic powders viewed through SEM, it can be seen that grain growth and sintering starts to happen during  $C_1$  for  $C_1$  temperatures at and above 950 °C and  $C_1$  dwelling times of 3 hours improves this. Below 950 °C, the grains and agglomerates are seen to be not fully formed. The grain sizes and agglomerate sizes are seen to practically constant in all samples after  $C_2$  due to a balance between grain growth and sintering after  $C_1$ , grain and agglomerate breakage during ball-milling and the energy stored for subsequent grain growth and sintering after  $C_2$ . Therefore, any significant differences in these powders cannot be detected by the techniques used.

From the PSD results of the powders, it was seen that reproducible results are obtained in-terms of particle sizes and distributions with respect to SEM for all the powders after  $C_1$  and  $C_2$ . The exact reason for the peaks in  $d_{33}$  produced for the 950 °C  $C_1$  temperature samples could be due to the balance between the tightness of the particle size distribution (which leads to inefficient packing of particles producing a high thickness in the composite and hence, a higher  $d_{33}$ ) with the amount of nano-fragments produced.

### 5.1.4 Ball-milling analysis

From the ball-milling analysis, it is seen that not ball-milling the sample produced favourable results with respect to  $d_{33}$ , microstructure and surface waviness. The sample which was ball-milled once had a similar average  $d_{33}$  but its

variation was higher owing to the ball-milling which broke the agglomerates and grains before  $C_2$ . The sample ball-milled twice had a severely reduced  $d_{33}$  which could be due to the presence of nano-particles or the lack of agglomerates. When ball milling is not employed at all, the handmilling required to break up the powder more gently is prohibitive to large scale production and so, as it has no appreciable effect on the  $d_{33}$ , the ball milling step was conserved. A method of more gently milling the powder should be determined to replace the ball milling step for an improvement to the microstructure.

### 5.1.5 Agglomeration variation analysis

From the agglomeration variation analysis, the 63-90  $\mu\text{m}$  agglomerate size range is seen to be optimum for producing a good quality composite with high  $d_{33}$ . This is due to a balance between the  $d_{33}$ , surface waviness and thickness produced in the composite due to the size of the agglomerates ( $d_{33}$  scales with the aspect ratio of the ceramic particles). Very high agglomerate sizes also caused excessive short-circuiting in the samples while lower agglomerate sizes had lower  $d_{33}$  but with practically the same surface waviness which resulted in no short-circuiting.

### 5.1.6 Composite synthesis method analysis

Based on the composite synthesis methods analysed, hot-pressing yields better performance in the composite compared to solution casting, likely due to its improved density. The porosity of solution cast composites hinders poling and can create short-circuits in the sample that eventually produce a lower  $d_{33}$ . Additional investigation must be done on generating a lesser viscosity so that R50 composites can be made with hot-pressing. In this way, the properties can be compared with the R50 solution-cast composites easily to better give information on which synthesis is more viable.

### 5.1.7 Precursor optimization

The KNLN-3 ceramic powder made with a less pure form of  $\text{Nb}_2\text{O}_5$  is seen to perform equally compared to the more pure form as a composite. Furthermore, no changes in purity in the each of the ceramic powders was seen through XRD and the KNLN-3 ceramic powder was seen to be formed completely after  $C_2$  for both the samples. Hence, the less pure form of  $\text{Nb}_2\text{O}_5$  can be said to replace the more pure form as the starting precursor.

### 5.1.8 Poling method analysis

Based on the poling methods analysed, the  $d_{33}$  obtained in the composites by contact poling seem to have almost the same  $d_{33}$  compared to those poled by corona poling with strongly overlapping standard deviations. Thus, corona poling can be seen as a viable replacement over contact poling. The corona poling was seen to be insensitive to microstructure and thickness of the composites which could have resulted in the higher values of  $d_{33}$  observed in the higher  $C_1$  temperatures samples as opposed to contact poling which had a peak in  $d_{33}$  for  $C_1=950^\circ\text{C}$ -1 h sample due to its high thickness formed by a tight distribution of particles.

### 5.1.9 Mechanical testing

From the two mechanical tests conducted, the R50 composite with no glass fibres was chosen as the ideal composite sample as it is the most optimized sample with respect to stiffness,  $F_N$ , flexibility and piezoelectric properties. However, further optimisation of the glass fiber content is required due to inhomogeneity in the final films.

## 5.2 Future work

Based on the work done and results obtained, the following work can be done for the future to further enhance the optimization towards scale-up and the subsequent mechanical testing:

1. Surface area analysis can be performed on the powders to better quantify the relative densities of the sintered agglomerates to investigate whether the increase in  $d_{33}$  for some samples is due to the tightness of the particle sizes that produces lesser packing. A pore-size analyzer relying on the BET (Brunauer, Emmett and Teller) method can be potentially used for this purpose.
2. TEM (transmission electron microscopy) can be used to view the defect structure of the nano-fragments produced in the samples to investigate the cause of their non-piezoelectricity. Raman, FTIR spectroscopy can be used to investigate the chemical bonds present in the nano-fragments for the same purpose (as a probe to check the defects present in the crystal lattice of the nano-fragments). Additionally, Raman and FTIR spectroscopy can also be performed to check the oxygen vacancies that could be potentially created in the samples.
3. Corona poling should be done on the dwelling time variation samples and the samples with very large agglomerates. Since corona poling involves the use of a corona to pole the composite and does not require electrodes, the surface waviness and electrode quality would not impact the poling of the composite and would not cause any short-circuits. These results can be compared with the contact poling results to see which type of poling is more viable for scale-up as well as which powders are truly the optimum.
4. XRD can be rerun for all the samples with a higher resolution to check the Na, K alkali evaporation for them. This was because it is still currently debatable as to what exactly causes the peak broadening noticed after  $C_1$  for higher  $C_1$  temperature samples.
5. PSD analysis can be re-run with a refined trial that adequately separates the smaller nano-particles which may stick to the bigger grains. This will provide more quantitative evidence as to which  $C_1$  temperatures and dwelling times yield the most nano-particles and the subsequent effect on the  $d_{33}$  trend.
6. Data points which were planned but not done due to lack of time/material can be done to get a more refined trend of the experimental results.
7. An intermediate dwelling time of 2 hours and intermediate  $C_1$  temperatures between 900 °C and 1000 °C (in intervals of 20 °C) can be made and analyzed to get a more specific location for the peak in  $d_{33}$ .
8. The  $C_2$  settings can be varied to find out how it can influence the powder and the composite. Additionally, the ramp rate and cooling rate of both  $C_1$  and  $C_2$  can be changed to see their influence on the powder and composite.
9. The ball-milling settings such as: size of balls used, rotations per minute of ball-mill, time of ball-milling and number of balls used can be varied to find a gentler method of milling.
10. SEC (size exclusion chromatography) can be performed on the hot-pressed samples to check for potential degradation of the CFE polymer and correlated with the  $d_{33}$ .
11. A more elaborate set of mechanical tests can be performed on the optimized composite that involves measurement of more parameters such as  $d_{13}$ , blocking force, compressability etc.

# Appendix-A: Bibliography

- [1] P. K. Panda and B. Sahoo, "PZT to lead free piezo ceramics: A review," *Ferroelectrics*, vol. 474, no. 1, pp. 128–143, Jan. 2015.
- [2] V. Tikka and P. Laitinen, "Designing haptic feedback for touch display: Experimental study of perceived intensity and integration of haptic and audio," *Lect. Notes Comput. Sci. (including Subser. Lect. Notes Artif. Intell. Lect. Notes Bioinformatics)*, vol. 4129 LNCS, pp. 36–44, 2006.
- [3] P. Poncet *et al.*, "Design and realization of electroactive polymer actuators for transparent and flexible haptic feedback interfaces," *2016 17th Int. Conf. Therm. Mech. Multi-Physics Simul. Exp. Microelectron. Microsystems, EuroSimE 2016*, pp. 1–5, 2016.
- [4] J. Holterman and P. Groen, *An introduction to piezoelectric materials and components*. Stichting Applied Piezo, 2012.
- [5] G. Gautschi, "Background of Piezoelectric Sensors," in *Piezoelectric Sensorics: Force Strain Pressure Acceleration and Acoustic Emission Sensors Materials and Amplifiers*, Berlin, Heidelberg: Springer Berlin Heidelberg, 2002, pp. 5–11.
- [6] J. Tichý, J. Erhart, E. Kittinger, and J. Přívratská, "Fundamentals of Piezoelectric Sensorics: Mechanical, Dielectric, and Thermodynamical Properties of Piezoelectric Materials."
- [7] J. Curie and P. Curie, "Développement par compression de l'électricité polaire dans les cristaux hémiedres à faces inclinées," *Bull. la Société minéralogique Fr.*, vol. 3, no. 4, pp. 90–93, 1880.
- [8] G. Lippmann, "Principe de la conservation de l'électricité, ou second principe de la théorie des phénomènes électriques," *J. Phys. Theor. Appl*, vol. 1881, no. 1, pp. 381–394.
- [9] Mildred Dresselhaus, "Perovskite Solar Cell," 2019. [Online]. Available: <https://www.cei.washington.edu/education/science-of-solar/perovskite-solar-cell/>. [Accessed: 06-Nov-2019].
- [10] S. Stølen, E. Bakken, and C. E. Mohn, "Oxygen-deficient perovskites: Linking structure, energetics and ion transport," *Physical Chemistry Chemical Physics*, vol. 8, no. 4, pp. 429–447, 2006.
- [11] E. Ringgaard and T. Wurlitzer, "Lead-free piezoceramics based on alkali niobates," *J. Eur. Ceram. Soc.*, 2005.
- [12] P. K. Panda, "Review: Environmental friendly lead-free piezoelectric materials," *J. Mater. Sci.*, vol. 44, no. 19, pp. 5049–5062, Oct. 2009.
- [13] Z. G. Ye, "High-Performance Piezoelectric Single Crystals of Complex Perovskite Solid Solutions," *MRS Bull.*, vol. 34, no. 4, pp. 277–283, 2009.
- [14] M. Birkholz, "ZEITSCHRIFT FOR PHYSIK B Crystal-field induced dipoles in heteropolar crystals II: physical significance," 1995.
- [15] R. C. Garimella, V. R. Sastry, and M. S. Mohiuddin, "Piezo-Gen - An Approach to Generate Electricity from Vibrations," *Procedia Earth Planet. Sci.*, vol. 11, pp. 445–456, 2015.
- [16] G. H. Haertling, "Ferroelectric Ceramics: History and Technology."
- [17] S. J. Orfanidis, "Electromagnetic Waves and Antennas," 1999.
- [18] D. O'Hare, "Hydrothermal Synthesis," *Encycl. Mater. Sci. Technol.*, pp. 3989–3992, Jan. 2001.
- [19] Wikipedia contributors, "Hydrothermal synthesis," *Wikipedia, The Free Encyclopedia*, 2019. [Online].



Available: [https://en.wikipedia.org/w/index.php?title=Hydrothermal\\_synthesis&oldid=921517496](https://en.wikipedia.org/w/index.php?title=Hydrothermal_synthesis&oldid=921517496). [Accessed: 06-Nov-2019].

- [20] Q. Zhou, K. H. Lam, H. Zheng, W. Qiu, and K. K. Shung, "Piezoelectric single crystal ultrasonic transducers for biomedical applications," *Progress in Materials Science*, vol. 66. Elsevier Ltd, pp. 87–111, 2014.
- [21] R. . Ballas, *Piezoelectric Multilayer Beam Bending Actuators*, 1st ed. Berlin: Springer Berlin Heidelberg, 2007.
- [22] R. G. Ke, "PIEZO ELECTRICITY, PYROELECTRICITY, AND FERROELECTRICITY IN ORGANIC MATERIALS<sup>1,2</sup>," 1978.
- [23] S. Hashmi, G. Ferreira Batalha, C. J. Van Tyne, and B. Yilbas, "COMPREHENSIVE MATERIALS PROCESSING EDITOR-IN-CHIEF ASSESSING PROPERTIES OF CONVENTIONAL AND SPECIALIZED MATERIALS."
- [24] M.-J. Pan and C. A. Randall, "A Brief Introduction to Ceramic Capacitors."
- [25] N. A. Benedek and C. J. Fennie, "Why Are There So Few Perovskite Ferroelectrics?," Jul. 2013.
- [26] V. M. Goldschmidt, "Die Gesetze der Krystallochemie," *Naturwissenschaften*, vol. 14, no. 21, pp. 477–485, May 1926.
- [27] R. E. Cohen, "Origin of ferroelectricity in perovskites: The principal problems from a theoretical perspective," *Ferroelectrics*, vol. 150, no. 1, pp. 1–12, 1993.
- [28] G. Philippot, C. Elissalde, M. Maglione, and C. Aymonier, "Supercritical fluid technology: A reliable process for high quality BaTiO<sub>3</sub> based nanomaterials," *Advanced Powder Technology*, vol. 25, no. 5. Elsevier B.V., pp. 1415–1429, 01-Sep-2014.
- [29] N. Nair, "Screen/Stencil printing of flexible polymer/composite based piezoelectric material for haptic feedback and ultrasound applications Screen/stencil printing of flexible polymer/composite based piezoelectric material for haptic feedback and noise and Ultrasound application," 2017.
- [30] Y. Zhao, G.-C. Wang, and T.-M. Lu, *Characterization of Amorphous and Crystalline Rough Surface--Principles and Applications*, vol. 37. Elsevier, 2000.
- [31] S. Kawada, M. Kimura, Y. Higuchi, and H. Takagi, "(KNa)NbO<sub>3</sub>-Based multilayer piezoelectric ceramics with nickel inner electrodes," *Appl. Phys. Express*, vol. 2, no. 11, Nov. 2009.
- [32] A. Claudia Arias and K. Tae Hoon, "Characterization and applications of piezoelectric polymers Tae hoon Kim," 2015.
- [33] C. A. Randall, N. Kim, J.-P. Kucera, W. Cao, and T. R. Shrout, "Intrinsic and Extrinsic Size Effects in Fine-Grained Morphotropic-Phase-Boundary Lead Zirconate Titanate Ceramics."
- [34] Y. Huan, X. Wang, J. Fang, and L. Li, "Grain size effects on piezoelectric properties and domain structure of BaTiO<sub>3</sub> ceramics prepared by two-step sintering," *J. Am. Ceram. Soc.*, vol. 96, no. 11, pp. 3369–3371, Nov. 2013.
- [35] Contributors to Orangeleaf Systems Ltd, "Sintering in the Powder Metallurgy Process," *Orangeleaf Systems Ltd*, 2019. [Online]. Available: <https://www.pm-review.com/introduction-to-powder-metallurgy/sintering-in-the-powder-metallurgy-process/>. [Accessed: 07-Nov-2019].
- [36] Y. Yang *et al.*, "Electret film-enhanced triboelectric nanogenerator matrix for self-powered instantaneous tactile imaging," *ACS Appl. Mater. Interfaces*, vol. 6, no. 5, pp. 3680–3688, 2014.
- [37] H. Peng, X. Sun, W. Weng, and X. Fang, "5 - Energy Harvesting Based on Polymer," in *Polymer Materials for Energy and Electronic Applications*, H. Peng, X. Sun, W. Weng, and X. Fang, Eds. Academic Press, 2017, pp. 151–196.

- [38] J. S. Harrison, "Piezoelectric Polymers," 2001.
- [39] H. Tanaka, K. Takayama, and S. Taki, "The Piezoelectricity of Poly (vinylidene Fluoride) Related content Piezoelectricity of Poly (vinylidene Fluoride) under High Pressure," 1969.
- [40] K. Tashiro, H. Tadokoro, and M. Kobayashi, "Structure and piezoelectricity of poly(vinylidene fluoride)," *Ferroelectrics*, vol. 32, no. 1, pp. 167–175, 1981.
- [41] M. Tamura, K. Ogasawara, N. Ono, and S. Hagiwara, "Piezoelectricity in uniaxially stretched poly(vinylidene fluoride)," *J. Appl. Phys.*, vol. 45, no. 9, pp. 3768–3771, Sep. 1974.
- [42] E. Fukada and T. Furukawa, "Piezoelectricity and ferroelectricity in polyvinylidene fluoride."
- [43] Y. Ting, H. Gunawan, A. Sugondo, and C. W. Chiu, "A new approach of polyvinylidene fluoride (PVDF) poling method for higher electric response," in *Ferroelectrics*, 2013, vol. 446, no. 1, pp. 28–38.
- [44] T. T. Wang, "Piezoelectricity in  $\beta$ -phase poly(vinylidene fluoride) having a 'single-crystal' orientation," *J. Appl. Phys.*, vol. 50, no. 10, pp. 6091–6094, 1979.
- [45] T. Yagi and M. Tatemoto, "A Fluorine-19 NMR Study of the Microstructure of Vinylidene Fluoride-Trifluoroethylene Copolymers," 1979.
- [46] T. Yamada, T. Ueda, and T. Kitayama, "Ferroelectric-to-paraelectric phase transition of vinylidene fluoride-trifluoroethylene copolymer," *J. Appl. Phys.*, vol. 52, no. 2, pp. 948–952, 1981.
- [47] G. T. Davis, T. Furukawa, A. J. Lovinger, and M. G. Broadhurst, "Structural and Dielectric Investigation on the Nature of the Transition in a Copolymer of Vinylidene Fluoride and Trifluoroethylene (52/48 mol %)," 1982.
- [48] A. J. Lovinger, G. Davis, T. Furukawa, and M. G. Broadhurst, "Crystalline Forms in a Copolymer of Vinylidene Fluoride and Trifluoroethylene (52/48 mol %)," *Macromolecules*, vol. 15, no. 2, pp. 323–328, 1981.
- [49] T. Furukawa, "Ferroelectric properties of vinylidene fluoride copolymers," *Phase Transitions*, vol. 18, no. 3–4, pp. 143–211, Aug. 1989.
- [50] K. Omote, H. Ohigashi, and K. Koga, "Temperature dependence of elastic, dielectric, and piezoelectric properties of 'single crystalline' films of vinylidene fluoride trifluoroethylene copolymer," *J. Appl. Phys.*, vol. 81, no. 6, pp. 2760–2769, Mar. 1997.
- [51] P. H. Ducrot, I. Dufour, and C. Ayela, "Optimization of PVDF-TrFE Processing Conditions for the Fabrication of Organic MEMS Resonators," *Sci. Rep.*, vol. 6, Jan. 2016.
- [52] N. Spampinato, J. Maiz, G. Portale, M. Maglione, G. Hadziioannou, and E. Pavlopoulou, "Enhancing the ferroelectric performance of P(VDF-co-TrFE) through modulation of crystallinity and polymorphism," *Polymer (Guildf)*, vol. 149, pp. 66–72, Aug. 2018.
- [53] L. E. Cross, "Relaxor ferroelectrics: an overview," *Ferroelectrics*, vol. 151, no. 1, pp. 305–320, 1994.
- [54] Q. Zhang, V. Bharti, and X. Zhao, "Giant Electrostriction and Relaxor Ferroelectric Behavior in Electron-Irradiated Poly(vinylidene fluoride-trifluoroethylene) Copolymer," *Science (80-. )*, vol. 280, no. 2101, p. 4, 1998.
- [55] Q. Chen *et al.*, "Relaxor ferroelectric polymers-fundamentals and applications," in *Ferroelectrics*, 2007, vol. 354, no. 1, pp. 178–191.
- [56] B. Chu, "PVDF-BASED COPOLYMERS, TERPOLYMERS AND THEIR MULTI-COMPONENT MATERIAL SYSTEMS FOR CAPACITOR APPLICATIONS," 2008.

- [57] Z. M. Dang, J. K. Yuan, J. W. Zha, T. Zhou, S. T. Li, and G. H. Hu, "Fundamentals, processes and applications of high-permittivity polymer-matrix composites," *Progress in Materials Science*, vol. 57, no. 4, pp. 660–723, May-2012.
- [58] R. E. Newnham, D. P. Skinner, and L. E. Cross, "Connectivity and piezoelectric-pyroelectric composites," *Mater. Res. Bull.*, vol. 13, no. 5, pp. 525–536, 1978.
- [59] A. Safari, "Development of Piezoelectric Composites For Transducers," <http://dx.doi.org/10.1051/jp3:1994191>, vol. 4, Jul. 1994.
- [60] D. A. Van Den Ende, S. E. Van Kempen, X. Wu, W. A. Groen, C. A. Randall, and S. Van Der Zwaag, "Dielectrophoretically structured piezoelectric composites with high aspect ratio piezoelectric particles inclusions," *J. Appl. Phys.*, vol. 111, no. 12, Jun. 2012.
- [61] R. E. Newnham, A. Safari, G. Sa-Gong, and J. Giniewicz, "FLEXIBLE COMPOSITE PIEZOELECTRIC SENSORS."
- [62] J. Khaliq *et al.*, "Effect of the piezoelectric ceramic filler dielectric constant on the piezoelectric properties of PZT-epoxy composites," *Ceram. Int.*, vol. 43, no. 2, pp. 2774–2779, Feb. 2017.
- [63] H. Khanbareh *et al.*, "Large area and flexible micro-porous piezoelectric materials for soft robotic skin," *Sensors Actuators, A Phys.*, vol. 263, pp. 554–562, Aug. 2017.
- [64] K. S. Challagulla and T. A. Venkatesh, "Electromechanical response of piezoelectric foams," *Acta Mater.*, vol. 60, no. 5, pp. 2111–2127, Mar. 2012.
- [65] D. Deutz, "Flexible piezoelectric composites Bridging the gap between materials and applications," TUDelft, 2017.
- [66] V. L. Stuber *et al.*, "Flexible Lead-Free Piezoelectric Composite Materials for Energy Harvesting Applications," *Energy Technol.*, vol. 7, no. 1, pp. 177–185, Jan. 2019.
- [67] M. Kimura, A. Ando, D. Maurya, and S. Priya, "Lead Zirconate Titanate-Based Piezoceramics," in *Advanced Piezoelectric Materials*, Elsevier, 2017, pp. 95–126.
- [68] Y. Xie and M. Eng, "Synthesis and Characterization of Piezo-/ferroelectric Lead Zirconate-Titanate (PZT) Single Crystals and Related Ternary Ceramics," 2008.
- [69] B. JAFFE, W. R. COOK, and H. JAFFE, "CHAPTER 6 - PROPERTIES OF PbTiO<sub>3</sub>, PbZrO<sub>3</sub>, PbSnO<sub>3</sub>, AND PbHfO<sub>3</sub> PLAIN AND MODIFIED," in *Piezoelectric Ceramics*, B. JAFFE, W. R. COOK, and H. JAFFE, Eds. Academic Press, 1971, pp. 115–134.
- [70] P. Marton, I. Rychetsky, and J. Hlinka, "Domain walls of ferroelectric BaTiO<sub>3</sub> within the Ginzburg-Landau-Devonshire phenomenological model," *Phys. Rev. B - Condens. Matter Mater. Phys.*, vol. 81, no. 14, Apr. 2010.
- [71] B. Noheda, D. E. Cox, G. Shirane, J. A. Gonzalo, L. E. Cross, and S. E. Park, "A monoclinic ferroelectric phase in the Pb(Zr<sub>1-x</sub>Ti<sub>x</sub>)O<sub>3</sub> solid solution," *Appl. Phys. Lett.*, vol. 74, no. 14, pp. 2059–2061, Apr. 1999.
- [72] C. Galassi, E. Roncari, C. Capiani, and F. Craciun, "Processing and Characterization of High Q<sub>m</sub> Ferroelectric Ceramics."
- [73] X. X. Wang, K. Murakami, O. Sugiyama, and S. Kaneko, "Piezoelectric properties, densification behavior and microstructural evolution of low temperature sintered PZT ceramics with sintering aids," 1200.
- [74] T. R. N. Kutty and R. Balachandran, "DIRECT PRECIPITATION OF LEAD ZIRCONATE TITANATE BY THE HYDROTHERMAL METHOD," 1984.
- [75] C. A. Oliveira, E. Longo, J. A. Varela, and M. A. Zaghete, "Synthesis and characterization of lead zirconate

- titanate (PZT) obtained by two chemical methods," *Ceram. Int.*, vol. 40, no. 1 PART B, pp. 1717–1722, 2014.
- [76] K. Uchino, *Ferroelectric devices, second edition*. 2009.
- [77] P. Devi *et al.*, "EFFECT OF Sr ON STRUCTURAL AND DIELECTRIC PROPERTIES OF LEAD LANTHANUM ZIRCONATE TITANATE PEROVSKITE CERAMICS," 2012.
- [78] C. Tapaonoi, S. Tashiro, H. Igarashi -Dielectric Properties of PbMg, C. Junichi Kato, Y. Yokotani, and M. Nishida, "Electric Properties of  $\text{Pb}(\text{Sb}_{1/2}\text{Nb}_{1/2})\text{O}_3$ – $\text{PbTiO}_3$ – $\text{PbZrO}_3$  Ceramics," Japan, 1994.
- [79] K. Uchino, Y. Sasaki, and T. Sugihara, "Stability of  $\text{pbzro}_3$ – $\text{pbtio}_3$ – $\text{pb}(\text{mn}_{1/3}\text{sb}_{2/3})\text{o}_3$  piezoelectric ceramics under vibration-level change," *Jpn. J. Appl. Phys.*, vol. 34, no. 9, pp. 5328–5331, 1995.
- [80] R. Gupta, S. Verma, D. Singh, K. Singh, and K. K. Bamzai, "Effect of Ni/Nb on structure, electrical and ferroelectric properties of 0.5PNN-0.5PZT ceramics," *Process. Appl. Ceram.*, vol. 9, no. 1, pp. 1–9, Mar. 2015.
- [81] J. Rödel, W. Jo, K. T. P. Seifert, E. M. Anton, T. Granzow, and D. Damjanovic, "Perspective on the development of lead-free piezoceramics," *J. Am. Ceram. Soc.*, vol. 92, no. 6, pp. 1153–1177, Jun. 2009.
- [82] Y. Li, K. S. Moon, and C. P. Wong, "Electronics without lead," *Science*, vol. 308, no. 5727, pp. 1419–1420, 03-Jun-2005.
- [83] Y.-M. Li, W. Chen, Q. Xu, J. Zhou, H.-J. Sun, and M.-S. Liao, "Dielectric and Piezoelectric Properties of  $\text{Na}_{0.5}\text{Bi}_{0.5}\text{TiO}_3$ – $\text{K}_{0.5}\text{Bi}_{0.5}\text{TiO}_3$ – $\text{NaNbO}_3$  Lead-Free Ceramics," 2005.
- [84] T. Takenaka, K. Maruyama, and K. Sakata, " $(\text{Bi}_{1/2}\text{Na}_{1/2})\text{TiO}_3$ – $\text{BaTiO}_3$  System for Lead-Free Piezoelectric Ceramics," *Jpn. J. Appl. Phys.*, vol. 30, no. Part 1, No. 9B, pp. 2236–2239, 1991.
- [85] A. Sasaki, T. Chiba, Y. Mamiya, and E. Otsuki, "Dielectric and Piezoelectric Properties of  $(\text{Bi}_{0.5}\text{Na}_{0.5})\text{TiO}_3$ – $(\text{Bi}_{0.5}\text{K}_{0.5})\text{TiO}_3$  Systems," *Jpn. J. Appl. Phys.*, vol. 38, no. Part 1, No. 9B, pp. 5564–5567, 1999.
- [86] Y. Saito *et al.*, "Lead-free piezoceramics," *Nature*, vol. 432, no. 7013, pp. 84–87, 2004.
- [87] I. Coondoo, N. Panwar, and A. Kholkin, "Lead-free piezoelectrics: Current status and perspectives," *J. Adv. Dielectr.*, vol. 3, no. 2, p. 1330002, Apr. 2013.
- [88] S. Zhang, R. Xia, and T. R. Shrout, "Lead-free piezoelectric ceramics vs. PZT?," *J. Electroceramics*, vol. 19, no. 4, pp. 251–257, Dec. 2007.
- [89] T. R. Shrout and S. J. Zhang, "Lead-free piezoelectric ceramics: Alternatives for PZT?," *J. Electroceramics*, vol. 19, no. 1, pp. 111–124, Sep. 2007.
- [90] J. F. Li, K. Wang, F. Y. Zhu, L. Q. Cheng, and F. Z. Yao, "(K, Na)  $\text{NbO}_3$ -based lead-free piezoceramics: Fundamental aspects, processing technologies, and remaining challenges," *J. Am. Ceram. Soc.*, vol. 96, no. 12, pp. 3677–3696, Dec. 2013.
- [91] R. . Jaeger and L. Egerton, "Hot Pressing of Potassium-Sodium Niobates," Ontario, 1962.
- [92] J. F. Li, K. Wang, B. P. Zhang, and L. M. Zhang, "Ferroelectric and piezoelectric properties of fine-grained  $\text{Na}_{0.5}\text{K}_{0.5}\text{NbO}_3$  lead-free piezoelectric ceramics prepared by spark plasma sintering," *J. Am. Ceram. Soc.*, vol. 89, no. 2, pp. 706–709, Feb. 2006.
- [93] D. Liu, D. Hongliang, F. Tang, F. Luo, D. Zhu, and W. Zhou, "Effect of heating rate on the structure evolution of  $(\text{K}_{0.5}\text{Na}_{0.5})\text{NbO}_3$ – $\text{LiNbO}_3$  lead-free piezoelectric ceramics," *J. Electroceramics*, vol. 20, Apr. 2008.
- [94] Y. Wang, D. Damjanovic, N. Klein, and N. Setter, "High-temperature instability of Li- and Ta-modified (K,Na) $\text{NbO}_3$  piezoceramics," *J. Am. Ceram. Soc.*, vol. 91, no. 6, pp. 1962–1970, Jun. 2008.

- [95] Y. Saito and H. Takao, "High performance lead-free piezoelectric ceramics in the (K,Na)NbO<sub>3</sub>-LiTaO<sub>3</sub> solid solution system," in *Ferroelectrics*, 2006, vol. 338, pp. 17–32.
- [96] Y. Guo, K. I. Kakimoto, and H. Ohsato, "Phase transitional behavior and piezoelectric properties of (Na<sub>0.5</sub>K<sub>0.5</sub>)NbO<sub>3</sub>-LiNbO<sub>3</sub> ceramics," *Appl. Phys. Lett.*, vol. 85, no. 18, pp. 4121–4123, Nov. 2004.
- [97] H. P. Kim, C. W. Ahn, Y. Hwang, H. Y. Lee, and W. Jo, "Strategies of a potential importance, making lead-free piezoceramics truly alternative to PZTs," *Journal of the Korean Ceramic Society*, vol. 54, no. 2. Korean Ceramic Society, pp. 86–95, 01-Mar-2017.
- [98] E. Hollenstein, D. Damjanovic, and N. Setter, "Temperature stability of the piezoelectric properties of Li-modified KNN ceramics," *J. Eur. Ceram. Soc.*, vol. 27, no. 13–15, pp. 4093–4097, 2007.
- [99] V. L. Stuber, T. R. Mahon, S. van der Zwaag, and P. Groen, "The effect of the intrinsic electrical matrix conductivity on the piezoelectric charge constant of piezoelectric composites," *Mater. Res. Express*, vol. 7, no. 1, p. 15703, 2019.
- [100] N. K. James, D. B. Deutz, R. K. Bose, S. van der Zwaag, and P. Groen, "High Piezoelectric Voltage Coefficient in Structured Lead-Free (K,Na,Li)NbO<sub>3</sub> Particulate—Epoxy Composites," *J. Am. Ceram. Soc.*, vol. 99, no. 12, pp. 3957–3963, 2016.
- [101] D. B. Deutz, N. T. Mascarenhas, S. van der Zwaag, and W. A. Groen, "Poling piezoelectric (K,Na,Li)NbO<sub>3</sub>-polydimethylsiloxane composites," *Ferroelectrics*, vol. 515, no. 1, pp. 68–74, 2017.
- [102] R. Gao, X. Chu, Y. Huan, X. Wang, and L. Li, "(K, Na) NbO<sub>3</sub> based piezoceramics prepared by a two-step calcining and ball milling route," *Mater. Lett.*, vol. 123, pp. 242–245, May 2014.
- [103] J. Wu and Y. Wang, "Two-step sintering of new potassium sodium niobate ceramics: A high d<sub>33</sub> and wide sintering temperature range," *Dalt. Trans.*, vol. 43, no. 34, pp. 12836–12841, Sep. 2014.
- [104] J. Wu, D. Xiao, and J. Zhu, "Potassium-sodium niobate lead-free piezoelectric materials: Past, present, and future of phase boundaries," *Chem. Rev.*, vol. 115, no. 7, pp. 2559–2595, 2015.
- [105] P. Bomlai, P. Wichianrat, S. Muensit, and S. J. Milne, "Effect of calcination conditions and excess alkali carbonate on the phase formation and particle morphology of Na<sub>0.5</sub>K<sub>0.5</sub>NbO<sub>3</sub> powders," *J. Am. Ceram. Soc.*, vol. 90, no. 5, pp. 1650–1655, 2007.
- [106] D. Maurya, Y. Yan, and P. Jeba, *Development of KNN-Based Piezoelectric Materials*, vol. 9781441995, no. October. 2013.
- [107] V. Vivekananthan, N. R. Alluri, Y. Purusothaman, A. Chandrasekhar, and S. J. Kim, "A flexible, planar energy harvesting device for scavenging road side waste mechanical energy: Via the synergistic piezoelectric response of K<sub>0.5</sub>Na<sub>0.5</sub>NbO<sub>3</sub>-BaTiO<sub>3</sub>/PVDF composite films," *Nanoscale*, vol. 9, no. 39, pp. 15122–15130, 2017.
- [108] Z. Yang, H. Peng, W. Wang, and T. Liu, "Crystallization behavior of poly(ε-caprolactone)/layered double hydroxide nanocomposites," *J. Appl. Polym. Sci.*, vol. 116, no. 5, pp. 2658–2667, 2010.
- [109] M. Rawat and K. L. Yadav, "Dielectric, enhanced magnetic and magnetodielectric properties of hot pressed (BNBT-BFO)/PVDF composite films," *J. Polym. Res.*, vol. 22, no. 12, pp. 1–7, 2015.
- [110] D. Waller and A. Safari, "Corona poling of pzt ceramics and flexible piezoelectric composites," *Ferroelectrics*, vol. 87, no. 1, pp. 189–195, 1988.
- [111] Y. Bai, K. Ding, G. P. Zheng, S. Q. Shi, J. L. Cao, and L. Qiao, "The electrocaloric effect around the orthorhombic-tetragonal first-order phase transition in BaTiO<sub>3</sub>," *AIP Adv.*, vol. 2, no. 2, 2012.

- [112] N. T. Mascarenhas, "2015 Highly flexible lead-free piezoelectric composites for vibration damping and noise cancellation application," pp. 1–93, 2015.
- [113] X. Wang *et al.*, "Oxygen-vacancy-related high-temperature dielectric relaxation in SrTiO<sub>3</sub> ceramics," *J. Appl. Phys.*, vol. 107, no. 11, 2010.
- [114] L. C. Sögütöglü, P. A. J. Donkers, H. R. Fischer, H. P. Huinink, and O. C. G. Adan, "In-depth investigation of thermochemical performance in a heat battery: Cyclic analysis of K<sub>2</sub>CO<sub>3</sub>, MgCl<sub>2</sub> and Na<sub>2</sub>S," *Appl. Energy*, vol. 215, no. 2018, pp. 159–173, 2018.
- [115] A. Harabor, P. Rotaru, and N. A. Harabor, "Two phases in a commercial anhydrous sodium carbonate by air contact," *Ann. Univ. Craiova, Phys.*, vol. 23, pp. 79–88, 2013.
- [116] U. Sutharsini, R. Singh, and M. T. and R. Singh, "Two step sintering of ceramics," *Intech*, vol. i, no. tourism, p. 13, 2016.
- [117] A. F. Barzegar, D. Damjanovic, and N. Setter, "The effect of boundary conditions and sample aspect ratio on apparent  $d_{33}$ / piezoelectric coefficient determined by direct quasistatic method," *IEEE Trans. Ultrason. Ferroelectr. Freq. Control*, vol. 51, no. 3, pp. 262–270, 2004.
- [118] V. L. Stuber, T. R. Mahon, S. van der Zwaag, and W. A. Groen, "The effect of the intrinsic electrical matrix conductivity on the piezoelectric charge constant of piezoelectric composites," *Mater. Res. Express*, Nov. 2019.
- [119] C. M. Wu, C. W. Hsu, T. K. Lee, and S. Smith, "A virtual reality keyboard with realistic haptic feedback in a fully immersive virtual environment," *Virtual Real.*, vol. 21, no. 1, pp. 19–29, 2017.



## Appendix-B: Sample descriptions

Different samples were prepared based on the type of experiment that was done. Hence, a summary of all the samples that were prepared for each type of testing based on their production route is given in the subsequent sections.

### B1: Poling study samples

The types of piezocomposite samples made for agglomerate comparison are given in Table 3. The exact values for calcination temperature, dwelling time and poling settings were chosen from previous work done by Deutz *et al.* [65].

Table 3: Agglomerate comparison samples

Sample code	Ceramic type	T <sub>C1</sub> (°C)	t <sub>C1</sub> (hours)	T <sub>C2</sub> (°C)	t <sub>C2</sub> (hours)	Agglomerate sizes (μm)	Poling settings
SA16	KNLN-3	1050	1	925	10	63 to 125	5 kV for 20 minutes
SA17	KNLN-6	950	3	925	10	63 to 125	5 kV for 20 minutes
SA1'	KNLN-6	950	3	925	10	<63	10 kV for 10 minutes
SA2'	KNLN-3	1050	1	925	10	<63	10 kV for 10 minutes

### B2: First calcination temperature variation samples

The types of piezocomposite samples made for C<sub>1</sub> temperature variation are given in Table 4.

Table 4: C<sub>1</sub>temperature variation samples

Sample code	Ceramic type	T <sub>C1</sub> (°C)	t <sub>C1</sub> (hours )	T <sub>C2</sub> (°C)	t <sub>C2</sub> (hours)	Agglomerate sizes (μm)	Poling settings
SA15	KNLN-3	750	1	925	10	<63	10 kV for 10 minutes
SA5	KNLN-3	850	1	925	10	<63	10 kV for 10 minutes
SA4	KNLN-3	900	1	925	10	<63	10 kV for 10 minutes
SA7	KNLN-3	950	1	925	10	<63	10 kV for 10 minutes
SA3	KNLN-3	1000	1	925	10	<63	10 kV for 10 minutes
SA2'	KNLN-3	1050	1	925	10	<63	10 kV for 10 minutes
SA8	KNLN-3	1100	1	925	10	<63	10 kV for 10 minutes
SA14	KNLN-3	1150	1	925	10	<63	10 kV for 10 minutes

## B3 Dwelling time variation samples

The types of piezocomposite samples made for the dwelling time variation experiment are presented in [Table 5](#).

**Table 5: Dwelling time variation samples**

Sample code	Ceramic type	T <sub>C1</sub> (°C)	t <sub>C1</sub> (hours)	T <sub>C2</sub> (°C)	t <sub>C2</sub> (hours)	Agglomerate sizes (μm)	Poling settings	Precursor type
SA7	KNLN-3	950	1	925	10	<63	10 kV for 10 minutes	Non-premilled
SA22'	KNLN-3	950	3	925	10	<63	10 kV for 10 minutes	Non-premilled
SA10	KNLN-3	1000	1	925	10	<63	10 kV for 10 minutes	Premilled
SA11	KNLN-3	1000	3	925	10	<63	10 kV for 10 minutes	Premilled
SA13	KNLN-3	1050	1	925	10	<63	10 kV for 10 minutes	Premilled
SA12	KNLN-3	1050	3	925	10	<63	10 kV for 10 minutes	Premilled

## B4 Ball-milling samples

The types of piezocomposite samples made for the ball-milling analysis experiment are presented in [Table 6](#).

**Table 6: Nano-fragment analysis composite samples**

Sample code	Ceramic type	T <sub>C1</sub> (°C)	t <sub>C1</sub> (hours)	Ball-milling after C <sub>1</sub>	T <sub>C2</sub> (°C)	t <sub>C2</sub> (hours)	Ball-milling after C <sub>2</sub>	Washing after C <sub>2</sub> ball-milling	Poling settings
SA18	KNLN-3	1050	1	No	925	10	No	N/A	10 kV for 10 minutes
SA19	KNLN-3	1050	1	Yes	925	10	Yes	No	10 kV for 10 minutes
SA20	KNLN-3	1050	1	Yes	925	10	Yes	Yes	10 kV for 10 minutes
SA2'	KNLN-3	1050	1	Yes	925	10	No	N/A	10 kV for 10 minutes

## B5 Agglomerate comparison samples

As elaborated in [Section-4](#), the optimized powder seemed to be that of the SA22'. Thus, for the agglomerate comparison experiment, this powder was used to make the piezocomposite samples. The composite samples are presented in Table 7. The agglomerate size column in Table 7, refers to the mesh size used by the sieves after C<sub>2</sub>.

**Table 7: Agglomerate comparison study composite samples**

Sample code	Ceramic	T <sub>C1</sub>	t <sub>C1</sub>	T <sub>C2</sub>	t <sub>C2</sub>	Agglomerate	Poling settings
-------------	---------	-----------------	-----------------	-----------------	-----------------	-------------	-----------------

	type	(°C)	(hours)	(°C)	(hours)	size	
SA22'	KNLN-3	950	3	925	10	>125	5 kV for 5 minutes
SA22'	KNLN-3	950	3	925	10	90 to 125	5 kV for 5 minutes
SA22'	KNLN-3	950	3	925	10	63 to 90	5 kV for 5 minutes
SA22'	KNLN-3	950	3	925	10	25 to 63	5 kV for 5 minutes
SA22'	KNLN-3	950	3	925	10	<25	5 kV for 5 minutes

## B6 Mechanical testing samples

As elaborated in [Section-4](#), the optimized powder seemed to be that of the SA22'. Thus, for mechanical testing experiments, this powder was used to make the piezocomposite samples. The composite samples are presented in [Table 8](#). Additionally, for torsion testing, 2% weight of CFE polymer was added as glass fibres for better comparison of the stiffness parameters. The same was not done for DMA due to lack of time.

**Table 8: Mechanical testing composite samples**

Sample code	Ceramic type	T <sub>c1</sub> (°C)	t <sub>c1</sub> (hours)	T <sub>c2</sub> (°C)	t <sub>c2</sub> (hours)	Ceramic filler amount (Volume %)	Glass fibres	Cast height (mm)
R0-SA22'	N/A	N/A	N/A	N/A	N/A	0	No	2
R0-SA22'-GF	N/A	N/A	N/A	N/A	N/A	0	Yes	2
R10-SA22'	KNLN-3	950	3	925	10	10	No	2
R10-SA22'-GF	KNLN-3	950	3	925	10	10	Yes	2
R20-SA22'	KNLN-3	950	3	925	10	20	No	2
R20-SA22'-GF	KNLN-3	950	3	925	10	20	Yes	2
R30-SA22'	KNLN-3	950	3	925	10	30	No	1.5
R30-SA22'-GF	KNLN-3	950	3	925	10	30	Yes	1.5
R40-SA22'	KNLN-3	950	3	925	10	40	No	1.5
R40-SA22'-GF	KNLN-3	950	3	925	10	40	Yes	1.5
R50-SA22'	KNLN-3	950	3	925	10	50	No	1
R50-SA22'-GF	KNLN-3	950	3	925	10	50	Yes	1

R60-SA22'	KNLN-3	950	3	925	10	60	No	1
R60-SA22'-GF	KNLN-3	950	3	925	10	60	Yes	1

## B7 Particle size distribution samples

The powders made for the calcination study were tested for their particle size distributions. These are described in Table 9.

**Table 9: Particle size distribution powders**

Sample code	Ceramic type	T <sub>c1</sub> (°C)	t <sub>c1</sub> (hours)	T <sub>c2</sub> (°C)	t <sub>c2</sub> (hours)	Agglomerate sizes (μm)
SA15	KNLN-3	750	1	925	10	<63
SA4	KNLN-3	900	1	925	10	<63
SA3	KNLN-3	1000	1	925	10	<63
SA2'	KNLN-3	1050	1	925	10	<63
SA8	KNLN-3	1100	1	925	10	<63
SA14	KNLN-3	1150	1	925	10	<63

## B8 Poling method variation samples

All the composites made for the calcination study and agglomerate variation were planned to be poled by corona poling and tested for their  $d_{33}$  at SABIC technology centre in Bangaluru, India. However, the dwelling time variation samples, agglomeration samples and some calcination temperature variation were not poled by corona poling due to lack of powder. The composites which were tested are described in Table 10.

**Table 10: Corona poling samples**

Sample code	Ceramic type	T <sub>c1</sub> (°C)	t <sub>c1</sub> (hours)	T <sub>c2</sub> (°C)	t <sub>c2</sub> (hours)	Agglomerate sizes (μm)
SA5	KNLN-3	850	1	925	10	<63
SA4	KNLN-3	900	1	925	10	<63
SA7	KNLN-3	950	1	925	10	<63
SA3	KNLN-3	1000	1	925	10	<63
SA2'	KNLN-3	1050	1	925	10	<63

SA8	KNLN-3	1100	1	925	10	<63
-----	--------	------	---	-----	----	-----